ÉCOLE CENTRALE LYON

N°d'ordre 2016-03 Année 2016

Thèse de l'Université de Lyon

Advanced photonic crystal assisted thin film solar cells: from order to pseudo-disorder

Présentée devant
Ecole Centrale de Lyon

Spécialité: Photonique

Pour obtenir
Le grade de docteur

École doctorale : Electronique, Electrotechnique et Automatisme de Lyon

Par

He DING

Soutenue le 29 Janvier 2016

Jury

Rapporteur	Pr. Emmanuel Centeno	Université Blaise-Pascal, Institut Pascal
Rapporteur	Pr. Jean-Jacques Simon	Aix-Marseille Université, IM2NP
Examinateur	Pr. Nathalie Destouches	Université Jean-Monet, LabHC
Examinateur	Pr. Anne Kaminski	Grenoble INP, IMEP-LAHC
Directeur de thèse	Dr. Christian Seassal	Directeur de Recherche CNRS, INL
Co-directeur de thèse	Dr. Emmanuel Drouard	Ecole Centrale de Lyon, INL
Membre invité	Dr. Guillaume Gomard	Karlsrhue Institute of Technology

Laboratoire de recherche: Institut des Nanotechnologies de Lyon (INL) – CNRS UMR 5270

Acknowledgements

I express my sincere gratitude to my supervisor Dr. Christian Seassal, co-supervisor Dr. Emmanuel Drouard, and Dr. Loïc Lalouat, for giving me the opportunity to work with them for past more than three years. Christian, his immense knowledge, logical thinking, motivation, enthusiasm, especially his patience has helped me to overcome many difficulties and finish this dissertation. Emmanuel, his insightful comments and constructive criticisms at different stages of my researches were thought provoking and they helped me focus on my ideas. I am grateful to him for holding me to a high research standard and enforcing strict validations for each research result, and thus teaching me how to do research. Moreover, I am also thankful to both of them for encouraging the use of correct grammar and consistent notation in my writings and for carefully reading and commenting on countless revisions of this manuscript. Loïc has been always there to listen and give advices. I am deeply grateful to him for the long discussions that help me solve the detailed problems in my work.

I would like to thank the members in the collaborated nanophotonic and PV group: Abdelmounaim Harouri and Céline Chevalier, they are helpful in providing advices in the fabrication process. Regis Orobtchouk and Bastian Gonzalez-Acevedo, they have developed the numerical simulation software which is the main and important tool in my studies and researches. I also thank other professors in this group: Hai-son Nguyen, Fabien Mandorlo, Alain Fave and Erwann Fourmond; as well as the Ph.D students: Jia Liu and Romain Champory, for their helpful advices and suggestions.

I would like to acknowledge the platform 'Nanolyon', especially to the staffs Radoslaw Mazurczyk, Pierre Crémillieu and Jean-Louis Leclerq. They are very friendly, knowledgeable and they provide a great environment to complete the fabrication of my samples.

As well, Martin Foldyna, Pere Roca I Cabarrocas, from LPICM, and Olivier Deparis and Jérôme Muller, from UNamur, are acknowledged for fruitful discussions on the design of the nanophotonic structure. Many thanks for the colleges in IMEC Belgium for the sample preparing and characterizations.

I would like to thank the members who work in the Nanophotonic group. Cécile Jamois and Aurelien Griffart provide the optical setup to measure the micro-reflectivity of the sample. As well, I want to give many thanks to Aziz Benamrouche due to his

help on AFM measurements.

I would like to thank to Laurent Carrel, IT manager, for the respect of numerical simulations. My sincere thanks should be given to all the secretaries and other stuffs, Sylive Goncalves, Partricia Dufaut and Thérèse Martin for their help on the official papers and others.

I should give my warm thanks to my colleagues in the laboratory, Cédric Blanchard, Rémy Artinyan, Zhen Li, Alexandra Pavlova, Laurent Milord, Zhen Lin, David Allioux, Xin Guan, Hui Li and so on. Thanks for your helps and companying in these years and best wishes for your careers and future.

I appreciate that China Scholarship Council (CSC) offer the financial support for my Ph.D studies. I want to thank the French Research Agency (ANR) program 'NATHISOL' (Grant Agreement No ANR-12-PRGE-0004-01) and the European Union Seventh Framework Programme 'Photovoltaics' (Grant Agreement No. 309127). I would like to thank Ecole Centrale de Lyon (ECL) and Institute of Nanotechnology Laboratory (INL) offering the opportunity to study and research.

Finally, I will thank my parents: Mr. Suxiao Ding and Mrs. Su'e Ding for their sincerely care. Without their supports during these years, I could not complete this thesis very well.

Contents

1. Introduction

Energy is an essence of any human activity [1]. The traditional energy sources, such as coal, oil, and gas, play an important role and form today dominant sources of energy. Since these fossil fuels have a negative impact on the environment, renewable energy (hydropower, wind power, solar power) is expected to become significant in our daily life.

Photovoltaic (PV) solar cells are made up of semiconductor materials that absorb photons from sunlight and convert them into electricity [2, 3]. Over the last decade, thanks to novel technologies, economies of scale, the PV industry has been booming with growth rates well in excess of 30% per year and the cost is continuously reducing approximately 20 % for each time the cumulative production doubled [4, 5]. In spite of the high growth speed and the lower price, the PV area is still dependent on subsides in the major markets of the world, which is highly affected by government policies. In order to further develop the PV market, and to attract more industrial companies, costs should be further reduced, and solar cells efficiencies enhanced, in order to overcome grid parity [6, 7].

To succeed, many solutions based on different materials and different technologies are proposed, which are divided into three generations [6]. Among of these three generations, most solar cells presently on the market are based on first generation technology with silicon wafers, with this dominance likely to continue well into the future. Indeed, silicon is non-toxic and abundantly available in the earth crust, and crystalline silicon (c-Si) PV modules have shown their long-term stability over decades in practice [8]. However, they are rigid and the energy required to produce them is not negligible. Additionally, the cost of a c-Si PV module is clearly dominated by material costs, including especially that of the silicon wafer. In this context, thin film solar cells, also considered as second generation devices, offer substantial advantages since the material cost is reduced. These thin film solar cells could be made of a wide range of materials including silicon, but also other materials like, for example, copper indium gallium selenide (CIGS). Such materials lead to efficiencies over those of multi-crystalline silicon in laboratory [4]. In these second generation solar cells, the conversion efficiency remains limited by the absorption in layers as thin as a few hundreds of nanometers to a few micrometers. Therefore, it appears necessary to

overcome this limitation to reach acceptable efficiencies. Finally, the third generation solar cells aims at achieving devices with efficiencies typically above the Shockley Queisser limit for a single junction solar cell [9]. They require advanced concepts or tandem devices [10]. However, devices embedding novel concepts still need long term research and subsequent developments to become available for public applications. Our shorter-term reasonable goal is to obtain a higher conversion efficiency in thin film solar cells, by addressing their optical limitations.

In this thesis, we propose to optimize and implement advanced nanophotonic structures to perform efficient light trapping in thin film solar cells. From 2008 to 2012, the interest of photonic crystal (PC) nanopatterns was investigated at INL and in other institutes. This was the main topic of two PhD students at INL, Guillaume Gomard and Xianqin Meng. During my PhD, from 2012 to 2015, I have further developed advanced nanopatterns, including pseudo-disordered structures, to assist thin film crystalline silicon solar cells.

Among the various silicon materials in solar cell devices, we take into account the mono c-Si as the absorbing material mainly because of its good quality. The drawbacks in other silicon materials, e.g. high recombination of the a-Si and the thickness-limited performance of the poly-Si, restrict them to be potential. So considering the constraints of the PV domain, we will use heterojunction thin film solar cells made of “epifree” c-Si absorber passivated by an extremely thin a-Si:H layer.

I have contributed to the integration of periodic nanopatterns in functional c-Si solar cells, in collaboration with IMEC, LPICM and LPN. In this context, my role was to perform optical simulations to design and optimize thin film solar cells integrating realistic periodic patterns, and then to investigate and optimize the more complex pseudo-periodic patterns. I have also contributed to the fabrication of such patterns in absorbing c-Si layers, in order to investigate experimentally the light trapping effects.

In this manuscript, we first introduce photovoltaic solar cells, and then give a short review of the light trapping strategies in the chapter 2. Then, we describe the methodologies used to perform numerical simulations and experiments, in chapter 3. The targeted design is simulated by the finite difference time domain (FDTD) method or rigorous coupled wave analysis (RCWA). Demonstrators constituted of patterned absorbing layers or crystalline silicon solar cells stacks are fabricated by electronic beam lithography (EBL) and the reactive ion etching (RIE) technologies. Then in chapter 4, we focus on the net absorption of the absorbing layer in the complete thin

film solar cells, in which the top and active layers are patterned with two different types of the simple periodic photonic crystal structure, i.e. inverted pyramids and cylindrical holes. Optical simulations reveal that patterning the active layer (c-Si) as a 2D PC membrane enables to substantially increase its integrated absorption in a range of 300-1100nm compared to the unpatterned stack. Furthermore, the potential of a backside grating to further enhance the light trapping is evaluated in the same realistic configuration. In chapter 5, in order to further increase the absorption and meanwhile maintain the cost and the feasibility of the design, pseudo-disordered PC structures are proposed. The comparison of the total absorption of the solar cell between the pseudo-disordered structure and the optimized square lattice of holes structure will be investigated. After that, these patterned designs are fabricated on a model silicon-on-insulator-based (SOI) sample, and on more realistic c-Si layers bonded onto metal. Experiments are performed on such test samples to assess their optical performance. In the chapter 6, we discuss on the properties of pseudo-disordered patterns by using numerical simulation, in order to give key design rules and criteria to reach the highest net absorption increase in solar cells.

References and links

1. G. Boyle, *Renewable energy* (OXFORD university press, 2004).
2. M. A. Green, "Solar cells: operating principles, technology, and system applications," (1982).
3. A.-E. Becquerel, "Mémoire sur les effets électriques produits sous l'influence des rayons solaires," Comptes Rendus **9**, 1839 (1839).
4. M. A. Green, K. Emery, Y. Hishikawa, W. Warta, and E. D. Dunlop, "Solar cell efficiency tables (Version 45)," Progress in photovoltaics: research and applications **23**, 1-9 (2015).
5. A. El-Ghonemy, "Photovoltaic solar energy: review," International Journal of Scientific & Engineering Research **3**(2012).
6. B. Parida, S. Iniyan, and R. Goic, "A review of solar photovoltaic technologies," Renewable and sustainable energy reviews **15**, 1625-1636 (2011).
7. G. Singh, "Solar power generation by PV (photovoltaic) technology: a review," Energy **53**, 1-13 (2013).
8. S. Wenham and M. Green, "Silicon solar cells," Progress in Photovoltaics: Research and Applications **4**, 3-33 (1996).
9. W. Shockley and H. J. Queisser, "Detailed balance limit of efficiency of p-n junction solar cells," Journal of applied physics **32**, 510-519 (1961).
10. M. A. Green, "Third generation photovoltaics: Ultra-high conversion efficiency at low cost," Progress in Photovoltaics: Research and Applications **9**, 123-135 (2001).

2. Solar cells and light trapping

In this chapter, we will first introduce the main operating principle of solar cells. Then, we will present light trapping mechanisms to assist solar cells, with the particular attention to wavelength-scaled structures. The ultimate goal is to make the absorbing layer as thin as possible while still maintaining good absorption performance.

2.1 Principles of solar cell operation

Photovoltaic (PV) solar cells are devices that enable the direct conversion of sun light into electric power. Energy conversion consists of two essential steps [1, 2]. First, the absorbed photon generates an electron-hole pair. Second, the electron-hole pairs are separated by the structure of the device and are finally collected at the terminals separately.

2.1.1 Photogeneration

Incident photons from the sun can first be reflected, transmitted and the absorbed. Absorption and subsequent electron-hole pair generation occurs depending on the respective values of the photons energy ($h\upsilon$) and the bandgap (E_g) of the photovoltaic material (Fig. 2-1).

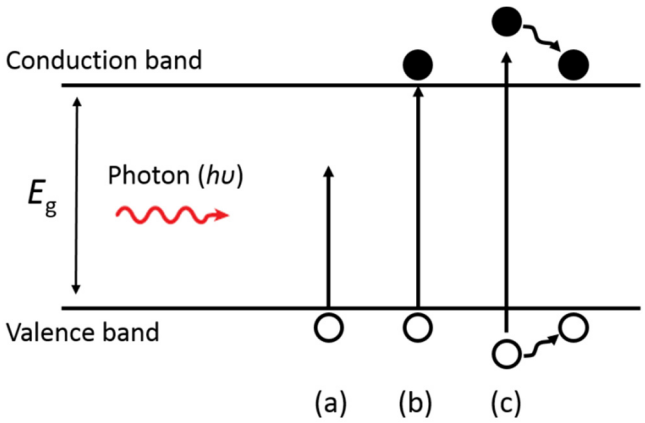

Figure 2-1. Schematic view of the generation process of electron-hole pairs excited by the light photons with different energy (hυ).[3]

(a) In the ideal case, if the energy of the photons is less than the bandgap energy of the solar cell material ($h\upsilon < E_g$), i.e. in the longer wavelengths range; incident light is not absorbed, and no electron-hole pair is generated. The absorbing material is actually transparent to these sub-band gap photons.

(b) Photons with energy equal to the bandgap ($h\upsilon = E_g$) generate electron-hole pairs without any loss.

(c) Photons with an energy higher than the band gap ($h\upsilon > E_g$) also excite electron-hole pairs. However, the excess energy above the band gap ($h\upsilon - E_g$) ends up as heat

instead of electrical power in the solar cell. Consequently, because of this thermalization process by the lattice vibration, these more energetic photons are not fully utilized.

Then we consider this optics-electronic link: the generation rate of the solar cells device [4]. The generation rate is equivalent to photon absorption rate the by assuming each absorbed photon excites an electron-hole pairs. The absorption per unit volume can be calculated from the divergence of the Poynting vector. To calculate the absorption as a function of space and frequency, we only need to know the electric field intensity (E) and the imaginary part of the permittivity (ε). The number of absorbed photons per unit volume can then be calculated by dividing this value by the energy per photon, so the generation rate (G) can be described by:

$$G = \frac{-0.5|E|^2 \, imag(\varepsilon)}{\hbar}$$

2.1.2 Charge separation

ın the second step of the PV process, the generated electron-hole pairs are separated and then collected at each terminal because of the internal electric field created by the diode structure in the solar cells.

In the dark condition, the solar cells can be considered as simple diodes, which current (I) is given by:

$$I = I_0\left(e^{\frac{qV}{n_{id}kT}} - 1\right)$$

When the diode is illuminated, the equation becomes:

$$I = I_0\left(e^{\frac{qV}{n_{id}kT}} - 1\right) - I_{ph}$$

Where the I_0 is the dark saturation current, q is the unit charge for an electron, V is the applied voltage across the diode, n_{id} is the ideality factor of the diode (1, for the ideal solar cell), k is the Boltzmann's constant, T is the absolute temperature and I_{ph} is the light generated current.

2.1.3 I-V curve and efficiency of a solar cell

In the following, we will introduce the current-voltage (*IV*) curve (Fig. 2-2) which typically represents the performance of a solar cell with its three characteristic parameters: short circuit-current (I_{sc}), open-circuit voltage (V_{oc}), and Filling factor (*FF*).

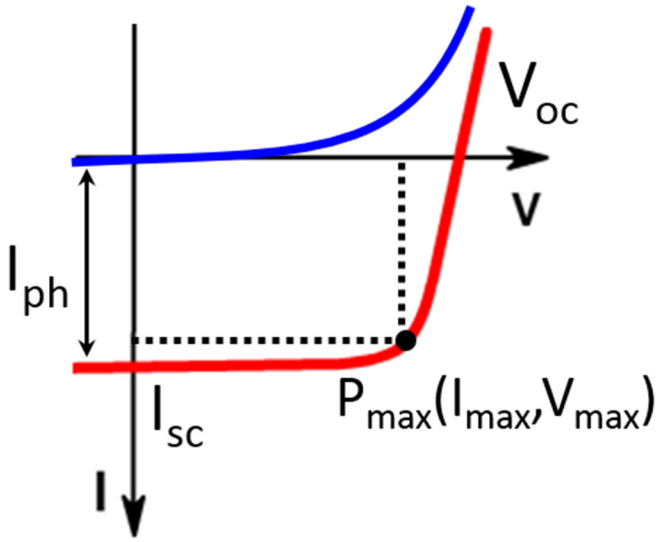

Figure 2-2. The current-voltage (IV) characteristics of a solar cell under dark (blue) or illumination (red) condition.

I_{sc} is the maximum current derived from the solar cell if no voltage is applied. Regardless of the resistive loss, I_{sc} in ideal solar cells is equal to the light generated current ($I_{sc}=I_{ph}$). In reality, the I_{sc} depends on a number of factors, including the area of the solar cell, the incident optical power, the spectrum of the incident light, the optical properties of the devices, and the efficiency of charge collection.

V_{oc} is the maximum voltage available from solar cells, and this occurs at zero current. In such open circuit conditions, the short circuit current compensates the dark current. V_{oc} can reach the limit E_g/q provided the carriers recombination are minimized.

While I_{sc} and V_{oc} are the maximum current and voltage respectively and set as the boundaries of the solar cell, a I_{sc} x V_{oc} electrical power cannot be generated in reality, since the *I(V)* curve does not exhibit a rectangular shape. So the maximum output power I_{max} x V_{max} is related to the "fill factor" ("*FF*"), which is defined as the ratio of the maximum power from the solar cell to the product of I_{sc} and V_{oc}, see Fig. 2-2b.

$$FF = \frac{I_{\max} V_{\max}}{I_{sc} V_{oc}}$$

Considering current densities (J) rather than currents (I), the solar cell is efficiency (η), which is defined as the ratio of the electrical output power to input energy from the sun, is given by:

$$\eta = \frac{V_{oc} J_{sc} FF}{P_{in}}$$

Hence, an increase of J_{sc} directly leads to an increase of the the solar cell efficiency. In this respect, we will use J_{sc} as our figure of merit when the parameters optimization processes are performed on the solar cell design architecture. At this point, is then useful to mention that the maximum J_{sc} that could be expected in a solar cell under a standard solar irradiance (AM1.5G solar spectrum, see below) is of 46 mA/cm² in a wavelength range less than 1200nm [5]. The usual expression of the short circuit-current density (J_{sc}), is

$$J_{sc} = qG\left(L_n + L_p\right)$$

Where G is the generation rate, and L_n and L_p are the electron and hole diffusion lengths respectively. Although this equation makes several assumptions, it indicates that the short-circuit current strongly depends on the generation rate and the diffusion length.

2.2 Sunlight absorption in a solar cell

2.2.1 Standard solar spectrum

The solar spectrum closely matches the radiation from a black body at a temperature of about 5,800 K. As it passes through the atmosphere, sunlight is attenuated by scattering and absorption. The air mass (AM) factor describes the path length of the light through the earth's atmosphere. The "AM1.5" solar spectrum is the standard solar irradiance is defined for terrestrial use [6]. It is the sun spectral irradiance after having passed through 1.5 times the thickness of the atmosphere. We will more specifically use the AM1.5G standard spectrum, where G stands for Global, and includes both direct and diffuse radiation (see Fig. 2-3). This spectrum is well suited to flat plate modules and it corresponds to an integrated power of 1000 W/m².

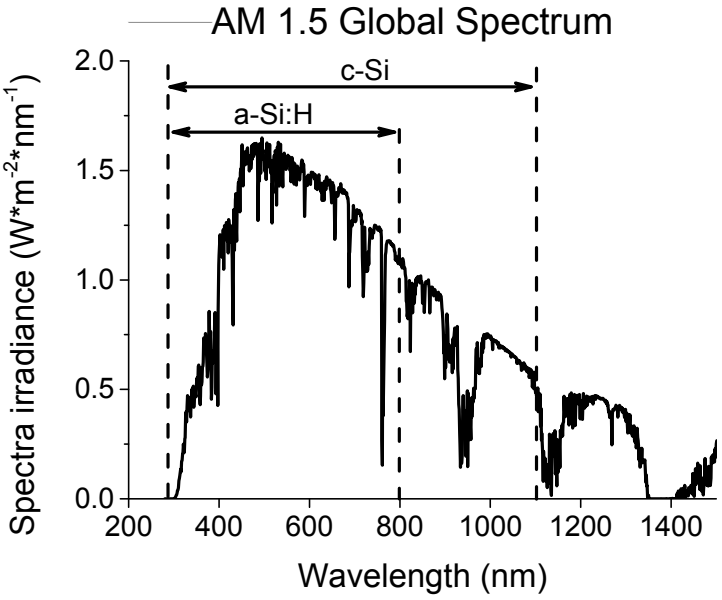

Figure 2-3. AM 1.5G solar spectrum intensity distribution, which includes both direct and diffuse radiation. The useful spectrum region for the a-Si:H and c-Si respectively.

2.2.2 Absorption in the PV material

Let us consider a semi-infinite thick layer as shown in Fig. 2-4, where no transmission or back reflection is taken into account. Reflection loss occurs at the front interface between the incident medium and the absorbing material; non-reflected light penetrates the layer and is gradually absorbed. Its intensity (I) is described by the formula of Beer-Lambert:

$$I(\lambda) = I_0 e^{-\alpha(\lambda)x}$$

Where x is the distance into the material at which the light intensity is being calculated, I_0 is the intensity at $x = 0$ and the absorption coefficient (α) is determined by the imaginary part of the refractive index κ,

$$\alpha = \frac{4\pi\kappa}{\lambda}$$

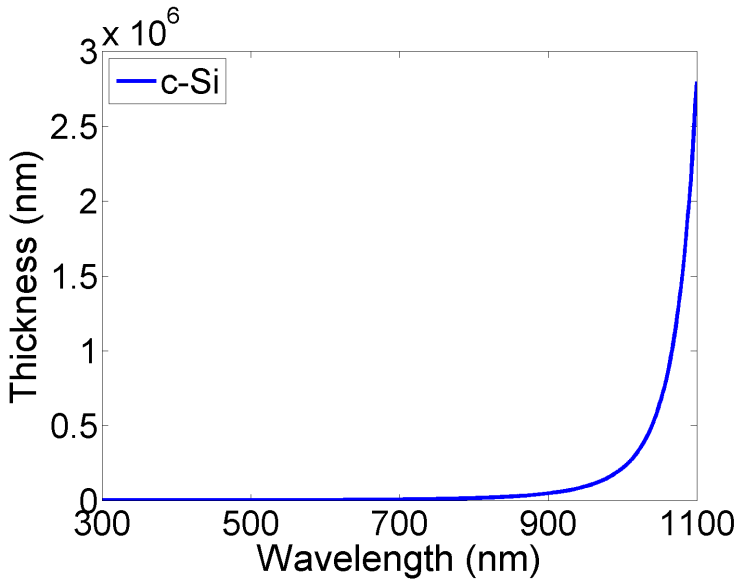

Figure 2-4. The absorption depth (nm) of the crystalline silicon (c-Si) mainly used in the thesis.

The absorption coefficient of the silicon in the long wavelength range is quite poor; a few micrometers are not enough to absorb efficiently the incident light. Photonic engineering is then even more important for thin c-Si solar cells.

2.3 Thin film silicon solar cells

Thin film solar cells [7, 8] are made by depositing one or several thin layers of photovoltaic material on a substrate, such as glass, plastic or metal. Thin film solar cells are commercially used in several technologies, including cadmium telluride (CdTe) [9, 10], copper indium gallium diselenide (CIGS) [11], amorphous (a-Si) [12] and other thin-film silicon (TF-Si). Film thickness varies from a few hundred nanometers (nm) to tens of micrometers (μm). This allows thin film cells to offer many advantages, such as their low cost, flexibility and the potentially improved voltage.

2.3.1 Main characteristics of thin film solar cells

- **Low cost**

Until now, most of these photovoltaic solar cells are based on the silicon material, especially the relatively thick and expensive crystalline wafers of silicon solar cells [13]. Using a reduce quantity of active material is expected to lead to a straightforward cost reduction.

- **Excellent portability**

When the thickness is small, it allows thin film cells to be flexible, of lower weight and somehow extensibility [14]. This excellent portability opens up many new applications for solar power that otherwise would not be feasible with wafer-based devices. For instance, the thin film solar cells could be used in building integrated photovoltaics and as semi-transparent, photovoltaic glazing material that can be laminated onto windows. In the future, it could be used for clothes, or integrated into the outside of an automobile or aircraft.

- **Efficiency**

In the PV industry, obtaining very thin solar cells while maintaining an overall higher efficiency is a key challenge. With thinner solar cells, the exited charge carriers will travel over shorter distances. Compared to bulk solar cells, thin film devices should therefore exhibit lower bulk recombination, leading to a higher V_{oc}. However, in the same time, the J_{sc} is expected to be reduced because of the lower amount of absorbing material. Since both V_{oc} and J_{sc} need to be maximized to increase the efficiency, the ideal solar cell is the one that is as thin as possible, and yet still absorbs the available light from the sun. Therefore, maximizing the absorption by using light trapping strategies is of fundamental importance; several possible strategies to reach this goal will be introduced in the following.

2.3.1 Silicon material for thin film solar cells

Among the different materials proposed in second-generation solar cells, silicon-based materials are attractive since they are abundant and non-toxic. From the point of view of processing and manufacturing, elemental materials are the simplest. However, there are no suitable elemental semiconductor materials available with direct bandgap close to 1.45eV, which would be the most appropriate to realize an optimum single junction device [7, 15, 16]. Silicon being an indirect bandgap material with a band gap of 1.1 eV is by no means an ideal material. However, silicon based solar cells dominate the PV market, and are available in their monocrystalline, polycrystalline, multi-crystalline or amorphous form [8, 17, 18].

Standard deposition techniques generally lead to amorphous silicon, polycrystalline or microcrystalline materials. Amorphous silicon (a-Si) has a high absorption coefficient [17, 19, 20] and a high bandgap energy (1.75eV). However, the

limitation of the stabilized efficiency, related to the Staebler-Wronski effect or light-induced degradation, restricts the performance of the a-Si solar cells. This material should be passivated by hydrogen, and its thickness should be limited to around 300nm. Their efficiency of a-Si:H cells remains limited to about 10% [21], which can be overcome by combining such junctions with c-Si in tandem cells [7, 12]. Polycrystalline/microcrystalline solar cells are common devices in the PV market thanks to theit relatively low-cost price and simple fabrication process. Generally, this leads the lower purity of silicon materials resulting in a limitation of the performance; the best conversion efficiency only could be achieved with few micrometers thick [22] and the highest efficiency is about 11% [23].

Crystalline silicon (c-Si) could still be obtained in a thin film form on foreign substrates like glass or metal. Specific and careful manufacturing processes are then required, leading to a relatively higher cost [17, 24, 25], however, thin c-Si layers, free of any grain boundaries are expected to lead to good performances. Several methods [1, 7, 17, 26] have been proposed to realize thin c-Si layers for PV applications. In this work, we will use an advanced 'epi-free' technology to fabricate the c-Si wafer, as developed at IMEC; it will be introduced in the chapter 3. We could also use approaches like epitaxial growth of c-Si layers (for example by plasma-enhanced chemical vapor deposition) and their subsequent transfer onto host wafers, as developed at LPICM [27].

The photon path in thin c-Si layers should be long enough to enable efficient sunlight absorption, in particular in the red and infrared ranges. Consequently, in order to obtain a high current, light trapping schemes should be considered.

2.4 Absorption enhancement based on light trapping strategies

The optimum thickness of the solar cell is related to many factors including economic aspects and properties of the materials. For effective solar absorption, silicon wafers need to be at least 50 μm thick unless optical enhancement techniques are used to improve their effective absorption. In this section, we will introduce a variety of concepts that have been proposed to control incident sunlight in-coupling and trapping in PV devices with strongly reduced thicknesses of active material. Indeed, in this case, the optical path length should be several times the actual device thickness. Consequently, optical losses should be greatly controlled and reduced.

2.4.1 Conventional schemes for the reduction of optical losses

Let us consider a silicon wafer with a flat surface and a thickness *d*, as shown in Fig. 2-5. Incident light can be either reflected, transmitted or absorbed. So the relation of the absorption (*A*), reflection (*R*) and transmission (*T*) is *A=1-R-T*. If we consider that *d>>l*, most of optical losses will be reflection losses, occurring on the top surface of the device. Additionally, long wavelength photons may not be absorbed, and can be lost by transmission, or be reflected back.

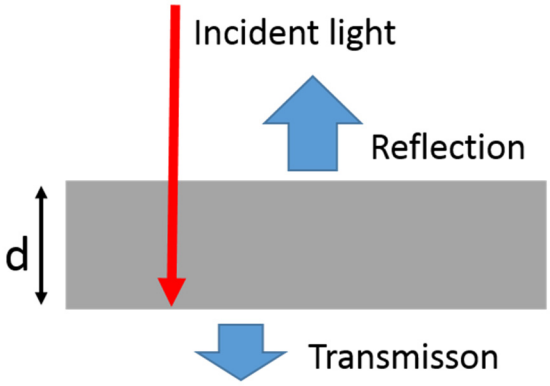

Figure 2-5. Schematic view of the incident light on the homogenous flat slab without applied light trapping.

Classical solutions to avoid such optical losses make use of anti-reflection (AR) coatings (Fig. 2-6a) and surface texturations (Fig. 2-6b). An AR coating consists of a thin layer deposited on top of solar cells to reduce their reflectance, which thickness is chosen so that the wavelength in the dielectric material is one quarter the wavelength of the incoming wave. To minimize the reflectance, the refractive index of this AR layer should be the geometric mean of that of the materials on both sides (glass or air and the absorbing layer). Continuously changing the refractive index of the AR layer or using multi-layer coatings can further decrease the top reflectance, using the same basic principle as with the single layer. However, benefits of multiple layers are too marginal considering their high cost, and potential mechanical and thermal instability. In some cases, and in first generation solar cells, the strategy may be to use the same material to realize the anti-reflection coatings and the surface passivation layers, e.g. SiN_X will decrease an average reflectance down to less than 2.5% [28].

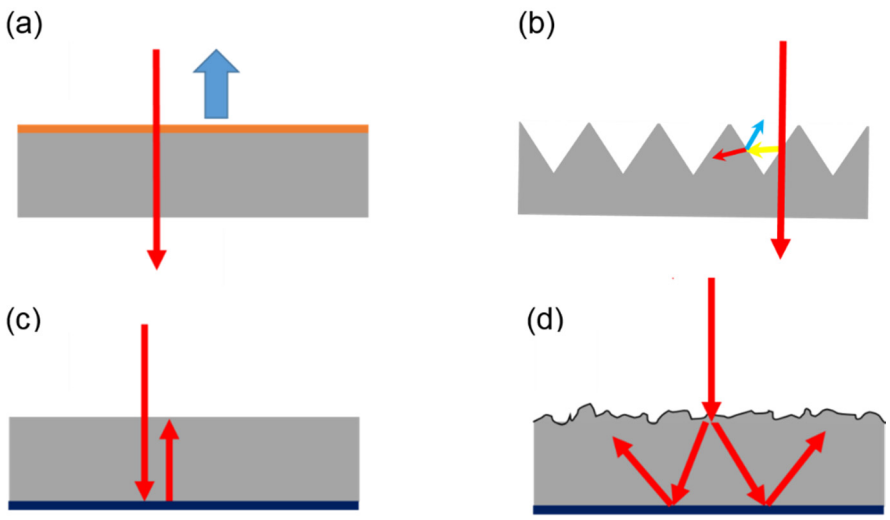

Figure 2-6. Conventional *schemes for reduction of optical losses with the anti-reflector (a), surface texturations (b), the back mirror (c) and ideal random scattering textures (d) applied to the simple flat slab.*

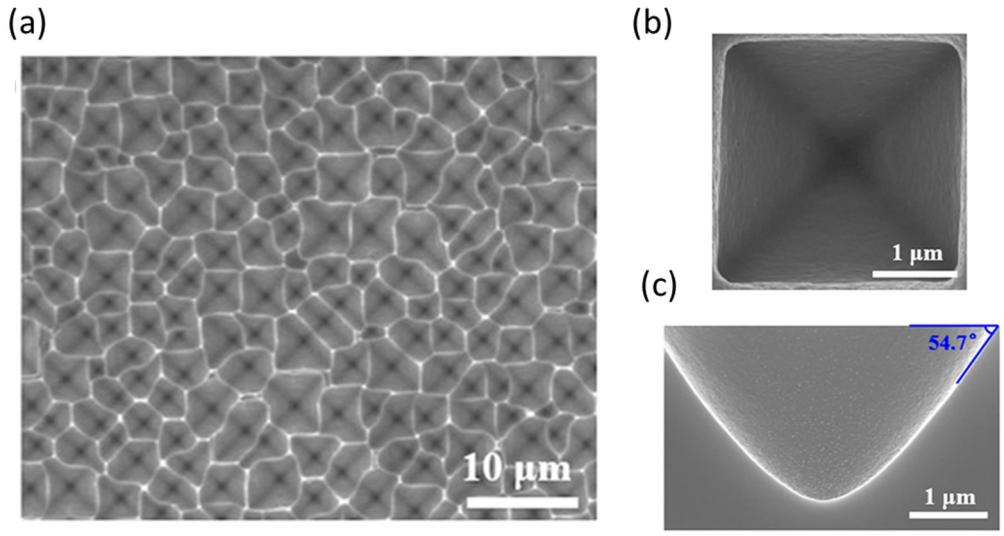

Figure 2-7. SEM images the random inverted pyramid texturations on silicon surface in the bulk solar cells. [29]

In order to minimize the reflection loss, surface texturations like random inverted pyramids (Fig. 2-7) [29] with feature size in the ten micrometers range are generally used in first generation solar cells (Fig. 2-6b). These are generally combined with an anti-reflection coating. Such structures make use of geometrical optics effects, bouncing the reflected beam back into the silicon. The reflected light has therefore more chance to be absorbed. Furthermore, reflected light entering the cell has a greater

chance of being absorbed because of its increased path length. Inverted pyramids in c-Si are generally obtained by anisotropic wet etching without the use of any mask.

In the case of solar cells based on thin absorbing layers, the thickness, i.e. the optical path length, is reduced, and turns out to be lower than the effective absorption length in the long wavelength range, leading to a limited absorption. In order to solve this problem, the effective optical path length should be increased. One could simply add a mirror at the rear of the absorber layer (Fig. 2-6c), which leads to a double optical path length. Indeed, a perfect reflector bonded on the solar cell is critical and helpful to increase the optical path length and then to achieve a higher efficiency. However, standard back reflectors like aluminum (Al) layers lead to parasitic absorption.

Though, even with a perfect back reflector, it can be noted that the absorption enhancement is still not enough. In commercialized thin film solar cells, in-coupling and trapping of light are achieved using light scattering, either at the front (Fig. 2-6d) or at the back of the solar cell, in order to increase the mean optical path length [30]. In 1982, Yablonovith [31] has proposed a fundamental limit for light trapping with an ideal scattering surface realized on a slab of semiconductor, which is called 'Lambertian surface'. An approximation of Lambertian surfaces is a roughened surface, which increases the chances of the reflected light to bounce back into the absorbing layer, with an angle leading to total internal reflection, rather than out of the device. Under important assumptions, including a high thickness of active layer ($d >> \lambda$) and a weak absorption ($\alpha d << 1$) in this material, a maximum absorption enhancement of $4n^2$ can be predicted, where n is the refractive index of the absorber material. This is referred to as the 'Yablonovith limit' or ergodic limit [32]. This randomization of the propagation direction of the incidence by a Lambertian surface is an effective method to trap the light. Let us recall that the critical angle that enables total internal reflection from the silicon is $\theta_c = sin^{-1} n_{air}/n_{si} \approx 16°$. Optical rays emerging with an angle lower than the critical angle escape from the cell, but rays with angles larger than this critical angle are totally internally reflected inside the cell. Integrating over the escape cone, one can deduce that only $1/n^2$ will escape through the front surface for each reflection. After a series expansion, it will eventually bring the path length enhancement close to $4n^2$, in silicon, this corresponds to a value close to 50 ($4 \times 3.5^2 \approx 50$).

However, as mentioned in the assumptions, this $4n^2$ limit is not relevant for thin film solar cells. It is possible to make use of wavelength or sub-wavelength scale

patterns to increase the photon path, sometimes leading to improvements above the Yablonovitch limit, but only over specific wavelength ranges [33, 34]. In this section, we have presented the main light trapping strategies suited to standard devices. We will then present designs that make use of nanophotonic structures and optical resonances in the following.

2.4.2 Nanophotonic structures for light trapping

During the past ten years, a wide range of nanopatterns was proposed, and their integration in thin film solar cells was extensively investigated. We will consider nano/micro patterns, with geometric size, such as the lattice parameter in the case of a periodic structure, of the order of the wavelength of the incident light. Geometrical optics is therefore inappropriate to describe the behavior of such structures. Conversely, they can take profit of the wave nature of the light, and their behavior may strongly depend on its wavelength and angle of incidence.

There is a vast variety of light trapping structures, including nano-wires [35, 36], dielectric gratings [37-40], plasmonic structures [41-43] and photonic crystal (PC) structures [24, 44-48]. Among these structures, PCs exhibit a wide range of optical modes and resonances, together with many adjustable parameters. Additionally, they do not lead to absorption losses in metallic nanostructures. For these reasons, we chose to make use of these structures, and to integrate them in thin film solar cells.

2.4.2.1 Periodic light trapping structure

PC structures are optical media where the refractive index exhibits a periodic modulation of a lattice constant of the order of the operation wavelength [49]. This property enables one to control the propagation of light in an unconventional way. While PC structure may be 1D, 2D or 3D, we will mainly consider 2D PCs fabricated in thin layers in this work.

A Bragg grating [33, 50, 51] is an example of a 1D PC structure; it corresponds to layers with a periodic distribution of the dielectric constant. Such stacks exhibit photonic bandgaps (corresponding to the wavelength range where reflectance is maximized) and band-edges, notably at the edges of the bandgaps, and leading to low group velocity modes. This concept may be used to realize a back reflector without metal, and which can exhibit low absorption losses. One may also consider 1D gratings,

or in other words, planar 1D PCs. Diffraction gratings are particular cases of 1D PCs, with a weak perturbation of the refractive index. 1D PCs can be patterned on the front side or the backside of the absorber of a solar cell [20, 24, 52]. Such structures act as dispersive elements that can split and diffract the light into different directions, depending on its wavelength. With front side gratings for instance, direct light coupling into waveguided modes can be achieved, which enables light trapping. For instance, a diffraction grating in a composite ZnO/ITO front stack can increase the absorption of a 100 nm thick a-Si:layer, thanks to an enhancement of the electromagnetic field in near field [53].

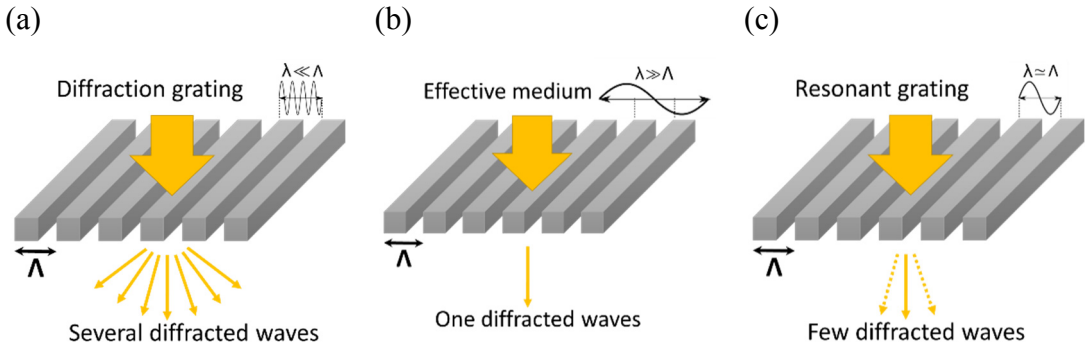

Figure 2-8. 1D grating structures designed for trapping of light. The different period of the grating (Λ) function with a normal incidence: diffraction grating (a), effective medium slab (b), and resonant (sub-wavelength) grating (c).

The properties of these structures primarily depends on the grating period [54], see Fig. 2-8. For short periods, the grating operates as an effective medium, which is relevant for light in-coupling, but not for light trapping, as it does not enable the coupling to waveguided modes. For too large periods, many diffracted orders will be available, each of them diffracting light over angles in a specific way; with such structures, controlling the generation of waveguided modes is therefore difficult. If the wavelength is of the order of the period ($\lambda \approx \Lambda$), as shown in Fig. 2-8c, the number of diffracted order is limited, leading to a better control of light trapping. In this case, a key parameter is the filling fraction (*ff*), defined as the ratio between the width of air slit and Λ, which will be discussed in the chapter 4.

2.4.2.2 Photonic crystal in thin film solar cells

An appropriate PC structures integrated on the top surface of the absorber layer of the solar cells can control the propagation and confinement of impinging light. This is expected to promote light in-coupling, and at the same time light trapping. The band structure of the PC displays the frequency as a function of the in-plane component of the wave-vector ($k_{//}$). The bands characteristics depend on the geometry of the structure, including the lattice parameter, the filling fraction and the refractive index contrast. The band structure shown in Fig. 2-9 corresponds to a 1D PC structure; it is displayed in the first Brillouin zone. No mode could exist with a frequency in the photonic band gaps (PBG). Coupling of permitted bands with radiative modes (i.e. with incident light from the free space) is only possible if the modes stand over the light line (blue dashed line), which is the case of the grey zone in Fig. 2-8. Additionally, such coupling is possible only if the modes symmetry is compatible with light coupling with an incident plane wave [33, 46]; this means that the overlap between the electromagnetic fields of propagating free space modes and that of resonant modes in the PC should not lead to zero after its integration over the space.

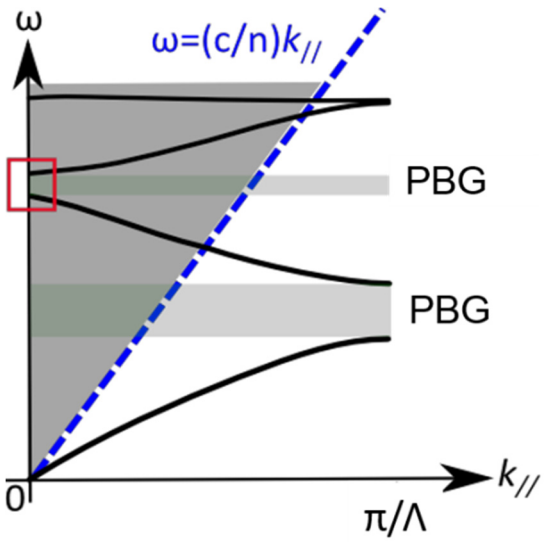

Figure 2-9. Dispersion schematic diagram of a photonic crystal presented in the first Brillouin zone (Λ is the period of the PC structure) and for the $k_{//} > 0$.

Let us analyze the dispersion characteristics along the wave vector, and in particular, the modes near the Γ-point in the red frame, which is corresponds to quasi-

normal incidence. The photonic bands being almost flat, the corresponding group velocity tends to 0 (at $k_{//}\approx 0$), which will increase the duration of light/material interaction in the absorbing structure. For such slow Bloch modes, provided symmetry enables coupling with propagating free-space modes, in-coupled photons will interact with the absorbing medium with an increased lifetime, leading to a maximized absorption.

2.4.2.3 Simply periodic 2D photonic crystals

Considering performance and feasibility, 2D PC structures exhibit key properties. First, such 2D patterns can be realized by using state-of-the-art semiconductor micro-fabrication technique, such as electron beam lithography, laser interference lithography and nanoimprint lithography. Moreover, as it will be shown below, their optical properties enable substantial absorption increase in the whole wavelength range of interest.

In 2D PC structures, various geometrical shapes[55], e.g. cylindrical holes, nanocones, squares and pyramids, have been proposed for the elementary pattern. Many research groups (see e.g. [19, 24, 34, 44, 56]) have investigated numerically the operation of solar cell devices including such periodic nanophotonic structures. Bermel et al.[57] was one of the very firsts to predict a large absorption enhancement (31.3% in their case) by adding an optimized 2D grating structure. Zhou et al. [58] has introduced a 2D back nanohole pattern combined with Bragg reflector in a 0.5μm thick a-Si:H stack, which increases the optical path length by a factor of hundred in the wavelength range of 600-775nm. Meng et al. [37] have proposed a dual pattern design consisting of the holes in the front layer and the grating on the bottom will provide a relative 65% increase compared to the flat case, with a J_{sc} of 30.3 mA/cm².

Since the early years, many efforts have been devoted to the fabrication of demonstrators. Cylindrical hole structures integrated on front surface of the a-Si:H or c-Si stacks were fabricated by Gomard et al. or Meng et al. respectively by using laser interference lithography and reactive ion etching technologies. Compared to the unpatterned references, the relative increase is about 27% [46] and 79% [59]. More recently, fully operational solar cells were realized. Chen et al. at MIT achieved a 15.7% efficiency with a 10μm thick c-Si solar cell including periodic inverted nanopyramids [60]. Jeong et al. [61] at Stanford obtain a 13.7% efficiency by integrating nano-cones

structures on top of a 10μm thick c-Si solar cell. Tanaka et al. [62] have fabricated a 0.5μm thick c-Si solar cells with PC structure, leading to a 1.3 times increase of a short circuit current density (from 15.0 mA/cm^2 to 19.6 mA/cm^2).

In this thesis, two kinds of nanopatterns shapes will be investigated: cylindrical nano-holes and inverted nanopyramids, will be integrated in thin film solar cells. According to the position of the patterns in the solar cells design, various properties are expected. If standing on the front, nanopatterns are expected to decrease the reflection losses (to optimize the in-coupling) and to improve light trapping in the active layers. Besides, the aim of the rear structure is to increase the diffraction of the long wavelength back into the structure and thus trap incident light into waveguided modes. Relative to the largest part of the papers published so far concerning nanopatterns integrated in a sole absorbing layer[34, 63, 64], we will consider the whole stack, including top and bottom electrodes, and doped layers as well as active layer. We will specifically consider the effect of periodic nano-holes or nanopyramids on the absorption in the sole intrinsic absorbing layer. This will lead to a fair evaluation of the gain expected from the photonic nanostructures (see chapter 4).

2.4.3 Disordered nanophotonic structures

Up to this point, we have considered solar cell architectures with simply periodic light trapping patterns, leading to an absorption increase compared to the unpatterned case. However, the achieved overall absorption enhancement is still far from the limits. Therefore, the thin film solar cells should be further developed by using more advanced patterns [65-68]. The two main objectives are (1) to make use of more modes per wavelength unit and (2) to make those modes absorb more light [69, 70].

Simply periodic nanostructures provide coherent scattering of light, and support extended Bloch modes that can be coupled with incident plane waves. However, to realize such periodic structures, it is in general necessary to use a dedicated technological process. On the other hand, disordered structure can be realized with simple processes, without any nanolithography. In addition, even in ordered photonic structures, fabrication induces a certain degree of disorder that affects the propagation, in-coupling and trapping of the incident light. The disorder due to the fluctuations in the fabrication processes affects the properties of structures like PCs [71]. That could

explain why measured absorption spectra are sometimes better than the simulation. This phenomenon suggests that introducing a disordered structure may be beneficial.

A substantial amount of work has been performed on disordered structure, both in the electronic and optical domains [65, 72-78]. These researches have focused on the revealing of the phenomena of the transport, localization and the wave scattering in the disordered structure, such as the Anderson light localization [79]. As introduced, the shortcoming of only focusing on periodic PCs is the limited spectral density of optical modes, in particular in the long wavelength range. A disordered structure can be obtained on the basis of a periodic PC by a random perturbation of either/both the size of the patterns or/and their position. This may lead to an enhancement of the spectral density of optical modes over a certain spectral range. It could lead to broader spectral and angular responses, which are clearly beneficial for photovoltaics applications.

Although perturbed structures provide a convenient path to field localization, it is difficult to engineer the design in order to achieve an optimization. Indeed, their optimization is highly time consuming and unpractical by considering the very large number of possible configurations. On the other hands, due to the random character of these structures, one could no longer make profit of the key properties of periodic structures, e.g. light coupling with carefully controlled Bloch modes.

Indeed, this is an open question in the nanophotonic community: is order better than disorder [80, 81]? Many simulations and experiments have been published recently in order to explore and answer this question [73, 81]. A way to go is to gradually introduce disorder in a periodic pattern [82] . In particular, partly disordered design, such as multi-periodic, periodically-ordered and pseudo-disordered structure, will fill the gap between perfectly ordered and fully disordered structures [69, 73, 74]. Using the supercell approach is a convenient way to investigate the transition. It could lead to a superior control over the photonic band dispersion and the density of optical states [83, 84].

In this thesis, we will notably (1) compare pseudo-disordered structures with optimized single periodic patterns, (2) consider the case of an absorbing layer covered by an antireflection layer and bonded on a back reflector layer, and (3) investigate the case of the different thicknesses of c-Si absorbing layers in the solar cells.

2.5 Conclusion and perspective

The main principles of solar cells operation, the properties of thin film silicon solar cells and key concepts used for light trapping, were introduced in this chapter. With PC structures, the absorption of thin film solar cells can be substantially increased with regards to non-patterned stacks. In order to increase the absorption in a large wavelength range, an approach consists in perturbing the PC structures to introduce a controlled degree of disorder in the design.

To design robust silicon thin film solar cells including PCs or partly disordered photonic structures, we will use the electromagnetic simulation to perform the optimization. Then with such optimized parameters, demonstrators will be fabricated and characterized.

References and links

1. S. Wenham and M. Green, "Silicon solar cells," Progress in Photovoltaics: Research and Applications **4**, 3-33 (1996).
2. G. Singh, "Solar power generation by PV (photovoltaic) technology: a review," Energy **53**, 1-13 (2013).
3. "Source: http://www.pveducation.org/pvcdrom/pn-junction/absorption-of-light."
4. Z. He, C. Zhong, X. Huang, W. Y. Wong, H. Wu, L. Chen, S. Su, and Y. Cao, "Simultaneous enhancement of open-circuit voltage, short-circuit current density, and fill factor in polymer solar cells," Advanced Materials **23**, 4636-4643 (2011).
5. R. Bube, *Fundamentals of solar cells: photovoltaic solar energy conversion* (Elsevier, 2012).
6. Source of data ASTM/NREL: http://rredc.nrel.gov/solar/spectra/am1.5/.
7. A. Shah, P. Torres, R. Tscharner, N. Wyrsch, and H. Keppner, "Photovoltaic technology: the case for thin-film solar cells," Science **285**, 692-698 (1999).
8. M. A. Green, "Thin-film solar cells: review of materials, technologies and commercial status," Journal of Materials Science: Materials in Electronics **18**, 15-19 (2007).
9. D. Bonnet and P. Meyers, "Cadmium-telluride—Material for thin film solar cells," Journal of Materials Research **13**, 2740-2753 (1998).
10. G. Fulop, M. Doty, P. Meyers, J. Betz, and C. Liu, "High-efficiency electrodeposited cadmium telluride solar cells," Applied Physics Letters **40**, 327-328 (1982).
11. R. Mickelsen and W. S. Chen, "High photocurrent polycrystalline thin-film CdS/CuInSe2 solar cella," Applied Physics Letters **36**, 371-373 (1980).
12. D. E. Carlson and C. Wronski, "Amorphous silicon solar cell," Applied Physics Letters **28**, 671-673 (1976).
13. T. Saga, "Advances in crystalline silicon solar cell technology for industrial mass production," npg asia materials **2**, 96-102 (2010).
14. M. B. Schubert and J. H. Werner, "Flexible solar cells for clothing," Materials today **9**, 42-50 (2006).

15. L. Dou, J. You, J. Yang, C.-C. Chen, Y. He, S. Murase, T. Moriarty, K. Emery, G. Li, and Y. Yang, "Tandem polymer solar cells featuring a spectrally matched low-bandgap polymer," Nature Photonics **6**, 180-185 (2012).
16. V. S. Gevaerts, A. Furlan, M. M. Wienk, M. Turbiez, and R. A. Janssen, "Solution processed polymer tandem solar cell using efficient small and wide bandgap polymer: fullerene blends," Advanced Materials **24**, 2130-2134 (2012).
17. A. Shah, H. Schade, M. Vanecek, J. Meier, E. Vallat-Sauvain, N. Wyrsch, U. Kroll, C. Droz, and J. Bailat, "Thin-film silicon solar cell technology," Progress in photovoltaics: Research and applications **12**, 113-142 (2004).
18. B. Parida, S. Iniyan, and R. Goic, "A review of solar photovoltaic technologies," Renewable and sustainable energy reviews **15**, 1625-1636 (2011).
19. O. El Daif, E. Drouard, G. Gomard, A. Kaminski, A. Fave, M. Lemiti, S. Ahn, S. Kim, P. Roca i Cabarrocas, and H. Jeon, "Absorbing one-dimensional planar photonic crystal for amorphous silicon solar cell," Optics express **18**, A293-A299 (2010).
20. G. Gomard, X. Meng, E. Drouard, K. El Hajjam, E. Gerelli, R. Peretti, A. Fave, R. Orobtchouk, M. Lemiti, and C. Seassal, "Light harvesting by planar photonic crystals in solar cells: the case of amorphous silicon," Journal of Optics **14**, 024011 (2012).
21. M. A. Green, K. Emery, Y. Hishikawa, W. Warta, and E. D. Dunlop, "Solar cell efficiency tables (Version 45)," Progress in photovoltaics: research and applications **23**, 1-9 (2015).
22. S. Hänni, G. Bugnon, G. Parascandolo, M. Boccard, J. Escarré, M. Despeisse, F. Meillaud, and C. Ballif, "High-efficiency microcrystalline silicon single-junction solar cells," Progress in Photovoltaics: Research and Applications **21**, 821-826 (2013).
23. H. Sai, T. Matsui, K. Matsubara, M. Kondo, and I. Yoshida, "11.0%-Efficient Thin-Film Microcrystalline Silicon Solar Cells With Honeycomb Textured Substrates," Photovoltaics, IEEE Journal of **4**, 1349-1353 (2014).
24. X. Meng, G. Gomard, O. El Daif, E. Drouard, R. Orobtchouk, A. Kaminski, A. Fave, M. Lemiti, A. Abramov, and P. R. i Cabarrocas, "Absorbing photonic crystals for silicon thin-film solar cells: Design, fabrication and experimental investigation," Solar Energy Materials and Solar Cells **95**, S32-S38 (2011).

25. M. A. Green, "Crystalline and thin-film silicon solar cells: state of the art and future potential," Solar Energy **74**, 181-192 (2003).
26. H. Keppner, J. Meier, P. Torres, D. Fischer, and A. Shah, "Microcrystalline silicon and micromorph tandem solar cells," Applied physics A **69**, 169-177 (1999).
27. R. Cariou, M. Labrune, and P. R. i Cabarrocas, "Thin crystalline silicon solar cells based on epitaxial films grown at 165 C by RF-PECVD," Solar Energy Materials and Solar Cells **95**, 2260-2263 (2011).
28. S. Duttagupta, F. Ma, B. Hoex, T. Mueller, and A. G. Aberle, "Optimised antireflection coatings using silicon nitride on textured silicon surfaces based on measurements and multidimensional modelling," Energy Procedia **15**, 78-83 (2012).
29. Y. Wang, L. Yang, Y. Liu, Z. Mei, W. Chen, J. Li, H. Liang, A. Kuznetsov, and D. Xiaolong, "Maskless inverted pyramid texturization of silicon," Scientific reports **5**(2015).
30. A. Goetzberger, "Optical confinement in thin Si-solar cells by diffuse back reflectors," in *15th Photovoltaic Specialists Conference*, 1981), 867-870.
31. E. Yablonovitch, "Statistical ray optics," JOSA **72**, 899-907 (1982).
32. T. Tiedje, E. Yablonovitch, G. D. Cody, and B. G. Brooks, "Limiting efficiency of silicon solar cells," Electron Devices, IEEE Transactions on **31**, 711-716 (1984).
33. Z. Yu, A. Raman, and S. Fan, "Fundamental limit of light trapping in grating structures," Optics express **18**, A366-A380 (2010).
34. A. Bozzola, M. Liscidini, and L. C. Andreani, "Photonic light-trapping versus Lambertian limits in thin film silicon solar cells with 1D and 2D periodic patterns," Optics Express **20**, A224-A244 (2012).
35. E. Garnett and P. Yang, "Light Trapping in Silicon Nanowire Solar Cells," Nano Letters **10**, 1082-1087 (2010).
36. J. Michallon, D. Bucci, A. Morand, M. Zanuccoli, V. Consonni, and A. Kaminski-Cachopo, "Light trapping in ZnO nanowire arrays covered with an absorbing shell for solar cells," Optics express **22**, A1174-A1189 (2014).
37. X. Meng, E. Drouard, G. Gomard, R. Peretti, A. Fave, and C. Seassal, "Combined front and back diffraction gratings for broad band light trapping in thin film solar cell," Optics Express **20**, A560-A571 (2012).
38. C. S. Schuster, P. Kowalczewski, E. R. Martins, M. Patrini, M. G. Scullion, M. Liscidini, L. Lewis, C. Reardon, L. C. Andreani, and T. F. Krauss, "Dual gratings

for enhanced light trapping in thin-film solar cells by a layer-transfer technique," Optics express **21**, A433-A439 (2013).

39. Y. Shi, X. Wang, W. Liu, T. Yang, and F. Yang, "Light-absorption enhancement in thin-film silicon solar cells with front grating and rear-located nanoparticle grating," physica status solidi (a) **212**, 312-316 (2015).
40. Z. Xia, Y. Wu, H. Jiao, H. Cao, Z. Liang, J. Zhou, and X. Qin, "Thin film silicon solar cells with non-simple integral period ratio between front and back gratings," Journal of Optics **16**, 105011 (2014).
41. S. Vedraine, P. Torchio, D. Duché, F. Flory, J.-J. Simon, J. Le Rouzo, and L. Escoubas, "Intrinsic absorption of plasmonic structures for organic solar cells," Solar energy materials and solar cells **95**, S57-S64 (2011).
42. K. R. Catchpole and A. Polman, "Plasmonic solar cells," Optics Express **16**, 21793-21800 (2008).
43. H. A. Atwater and A. Polman, "Plasmonics for improved photovoltaic devices," Nat Mater **9**, 205-213 (2010).
44. M. Burresi, F. Pratesi, F. Riboli, and D. S. Wiersma, "Complex Photonic Structures for Light Harvesting," Advanced Optical Materials (2015).
45. X. Sheng, L. Z. Broderick, and L. C. Kimerling, "Photonic crystal structures for light trapping in thin-film Si solar cells: Modeling, process and optimizations," Optics Communications **314**, 41-47 (2014).
46. G. Gomard, R. Peretti, E. Drouard, X. Meng, and C. Seassal, "Photonic crystals and optical mode engineering for thin film photovoltaics," Optics Express **21**, A515-A527 (2013).
47. D. Duché, C. Masclaux, J. Le Rouzo, and C. Gourgon, "Photonic crystals for improving light absorption in organic solar cells," Journal of Applied Physics **117**, 053108 (2015).
48. O. VanbéSien and E. Centeno, "Two-Dimensional Dielectric Photonic Crystals," Dispersion Engineering for Integrated Nanophotonics, 1-35 (2014).
49. J. D. Joannopoulos, S. G. Johnson, J. N. Winn, and R. D. Meade, *Photonic crystals: molding the flow of light* (Princeton university press, 2011).
50. L. Zeng, P. Bermel, Y. Yi, B. Alamariu, K. Broderick, J. Liu, C. Hong, X. Duan, J. Joannopoulos, and L. Kimerling, "Demonstration of enhanced absorption in thin film Si solar cells with textured photonic crystal back reflector," Applied Physics Letters **93**, 221105 (2008).

51. L. Zeng, Y. Yi, C. Hong, J. Liu, N. Feng, X. Duan, L. Kimerling, and B. Alamariu, "Efficiency enhancement in Si solar cells by textured photonic crystal back reflector," Applied Physics Letters **89**, 111111 (2006).
52. N. Destouches, D. Blanc, J. Franc, S. Tonchev, N. Hendrickx, P. Van Daele, and O. Parriaux, "Efficient and tolerant resonant grating coupler for multimode optical interconnections," Optics express **15**, 16870-16879 (2007).
53. A. Moreau, R. Smaali, E. Centeno, and C. Seassal, "Optically optimal wavelength-scale patterned ITO/ZnO composite coatings for thin film solar cells," Journal of Applied Physics **111**, 083102 (2012).
54. S. Collin, "Nanostructure arrays in free-space: optical properties and applications," Reports on Progress in Physics **77**, 126402 (2014).
55. J. Gjessing, A. S. Sudbø, and E. S. Marstein, "Comparison of periodic light-trapping structures in thin crystalline silicon solar cells," Journal of Applied Physics **110**, 033104 (2011).
56. J. G. Mutitu, S. Shi, C. Chen, T. Creazzo, A. Barnett, C. Honsberg, and D. W. Prather, "Thin film solar cell design based on photonic crystal and diffractive grating structures," Optics Express **16**, 15238-15248 (2008).
57. P. Bermel, C. Luo, L. Zeng, L. C. Kimerling, and J. D. Joannopoulos, "Improving thin-film crystalline silicon solar cell efficiencies with photonic crystals," Optics express **15**, 16986-17000 (2007).
58. D. Zhou and R. Biswas, "Photonic crystal enhanced light-trapping in thin film solar cells," Journal of Applied Physics **103**, 093102 (2008).
59. X. Meng, V. Depauw, G. Gomard, O. El Daif, C. Trompoukis, E. Drouard, C. Jamois, A. Fave, F. Dross, I. Gordon, and C. Seassal, "Design, fabrication and optical characterization of photonic crystal assisted thin film monocrystalline-silicon solar cells," Optics Express **20**, A465-A475 (2012).
60. M. S. Branham, W. C. Hsu, S. Yerci, J. Loomis, S. V. Boriskina, B. R. Hoard, S. E. Han, and G. Chen, "15.7% Efficient 10-μm-Thick Crystalline Silicon Solar Cells Using Periodic Nanostructures," Advanced Materials **27**, 2182-2188 (2015).
61. S. Jeong, M. D. McGehee, and Y. Cui, "All-back-contact ultra-thin silicon nanocone solar cells with 13.7% power conversion efficiency," Nature communications **4**(2013).

62. Y. Tanaka, K. Ishizaki, M. De Zoysa, T. Umeda, Y. Kawamoto, S. Fujita, and S. Noda, "Photonic crystal microcrystalline silicon solar cells," Progress in Photovoltaics: Research and Applications (2015).
63. S. B. Mallick, M. Agrawal, and P. Peumans, "Optimal light trapping in ultra-thin photonic crystal crystalline silicon solar cells," Optics express **18**, 5691-5706 (2010).
64. Q. G. Du, C. H. Kam, H. V. Demir, H. Y. Yu, and X. W. Sun, "Enhanced optical absorption in nanopatterned silicon thin films with a nano-cone-hole structure for photovoltaic applications," Optics letters **36**, 1713-1715 (2011).
65. F. Pratesi, M. Burresi, F. Riboli, K. Vynck, and D. S. Wiersma, "Disordered photonic structures for light harvesting in solar cells," Optics Express **21**, A460-A468 (2013).
66. R. A. Pala, J. S. Liu, E. S. Barnard, D. Askarov, E. C. Garnett, S. Fan, and M. L. Brongersma, "Optimization of non-periodic plasmonic light-trapping layers for thin-film solar cells," Nature communications **4**(2013).
67. J. Xavier, J. Probst, F. Back, P. Wyss, D. Eisenhauer, B. Löchel, E. Rudigier-Voigt, and C. Becker, "Quasicrystalline-structured light harvesting nanophotonic silicon films on nanoimprinted glass for ultra-thin photovoltaics," Optical Materials Express **4**, 2290-2299 (2014).
68. D. S. Wiersma, "Disordered photonics," Nature Photonics **7**, 188-196 (2013).
69. R. Peretti, G. Gomard, L. Lalouat, C. Seassal, and E. Drouard, "Absorption control in pseudodisordered photonic-crystal thin films," Physical Review A **88**, 053835 (2013).
70. A. Oskooi, M. De Zoysa, K. Ishizaki, and S. Noda, "Experimental Demonstration of Quasi-resonant Absorption in Silicon Thin Films for Enhanced Solar Light Trapping," ACS Photonics **1**, 304-309 (2014).
71. Z. Zhang and Y. Fan, "Propagation properties of a wave in a disordered multilayered system containing hyperbolic metamaterials," JOSA B **29**, 2995-2999 (2012).
72. M. Liscidini, A. Bozzola, P. Kowalczewski, and L. C. Andreani, "Light-trapping: From Order to Disorder in Thin-film Silicon Solar Cells," in *CLEO: Science and Innovations*, (Optical Society of America, 2013), CTh1M. 5.

73. A. Bozzola, M. Liscidini, and L. C. Andreani, "Broadband light trapping with disordered photonic structures in thin-film silicon solar cells," Progress in Photovoltaics: Research and Applications **22**, 1237-1245 (2014).
74. A. Oskooi, P. A. Favuzzi, Y. Tanaka, H. Shigeta, Y. Kawakami, and S. Noda, "Partially disordered photonic-crystal thin films for enhanced and robust photovoltaics," Applied Physics Letters **100**, 181110 (2012).
75. K. Vynck, M. Burresi, F. Riboli, and D. S. Wiersma, "Photon management in two-dimensional disordered media," Nat Mater **11**, 1017-1022 (2012).
76. X. Fang, M. Lou, H. Bao, and C. Y. Zhao, "Thin films with disordered nanohole patterns for solar radiation absorbers," Journal of Quantitative Spectroscopy and Radiative Transfer (2015).
77. M. Burresi, F. Pratesi, K. Vynck, M. Prasciolu, M. Tormen, and D. S. Wiersma, "Two-dimensional disorder for broadband, omnidirectional and polarization-insensitive absorption," Optics Express **21**, A268-A275 (2013).
78. U. W. Paetzold, M. Smeets, M. Meier, K. Bittkau, T. Merdzhanova, V. Smirnov, D. Michaelis, C. Waechter, R. Carius, and U. Rau, "Disorder improves nanophotonic light trapping in thin-film solar cells," Applied Physics Letters **104**, 131102 (2014).
79. M. Segev, Y. Silberberg, and D. N. Christodoulides, "Anderson localization of light," Nature Photonics **7**, 197-204 (2013).
80. C. Battaglia, C.-M. Hsu, K. Söderström, J. Escarre, F.-J. Haug, M. Charrière, M. Boccard, M. Despeisse, D. T. Alexander, and M. Cantoni, "Light trapping in solar cells: can periodic beat random?," ACS nano **6**, 2790-2797 (2012).
81. S. Mokkapati and K. Catchpole, "Nanophotonic light trapping in solar cells," Journal of applied physics **112**, 101101 (2012).
82. D. M. Callahan, K. A. Horowitz, and H. A. Atwater, "Light trapping in ultrathin silicon photonic crystal superlattices with randomly-textured dielectric incouplers," Optics express **21**, 30315-30326 (2013).
83. T. Utikal, T. Zentgraf, S. G. Tikhodeev, M. Lippitz, and H. Giessen, "Tailoring the photonic band splitting in metallodielectric photonic crystal superlattices," Physical Review B **84**, 075101 (2011).
84. V. Rinnerbauer, Y. Shen, J. D. Joannopoulos, M. Soljačić, F. Schäffler, and I. Celanovic, "Superlattice photonic crystal as broadband solar absorber for high temperature operation," Optics express **22**, A1895-A1906 (2014).

3. Simulation, fabrication and characterization methods for photonic crystal assisted thin film solar cells

In this chapter, we will present the methodologies of numerical simulation and the fabrication processes dedicated to photonic crystal designs assisted thin film solar cells. Characterization methods used to assess the properties of the fabricated structures will also be presented.

3.1 Numerical simulation methodology

Numerical simulations based on the solving of the Maxwell's equation are efficient methods to design and optimize the solar cell geometry and thus in order to maximize the efficiency, and firstly the short circuit current. Among many methods, the Finite difference time-domain method (FDTD) [1, 2] and rigorous coupled wave analysis method (RCWA) [3, 4], which could solve the Maxwell's equation either in the time-domain or the frequency domain, are used in this thesis, depending on the available functionalities.

3.1.1 Finite Difference Time Domain (FDTD) method

The finite difference time domain method (FDTD) is one of the most popular technique for the solution of electromagnetic problems [5]. It is a numerical analysis technique to solve time-dependant Maxwell's equation in any geometry by using finite-difference approximation of partial derivatives. In FDTD, space is meshed into box-shaped 'Yee' cells, where the electric field (E) and magnetic field (H) are computed at the edge or face centers of the cube respectively. Bloch boundary conditions with a given phase matching between the edges of the computation window allow the study of periodic structures. Symmetry can be taken into account for faster computation.

All spectra can be obtained in a single calculation, thanks to the simulation of the propagation of short pulses in the structures followed by a Fourier transform. The spectral resolution is the inverse of the simulated propagation time. FDTD method directly provides the electromagnetic field (E) everywhere in the structure, and thus enables a straightforward calculation of the absorption.

In this paper, a commercial software 'Lumerical' based on the FDTD method was used to perform the FDTD simulations [6]. Available but not detailed dispersion models allows to fit the chromatic dispersion properties of the materials with a good accuracy (few percent), but at the cost of a serious increase of the computation time and required resources due to the in time convolution process.

3.1.2 Rigorous Coupled Wave Analysis (RCWA) method

The rigorous coupled wave analysis (RCWA) method is typically used to solve diffraction of a field by a given periodic grating structure at any given wavelength. Two

dimensional in plane dielectric function and thus fields are written as a sum of spatial harmonics. A device is divided into a number of z-invariant layers, all having the same in-plane periodicity. The propagating and evanescent diffracted orders in each layer are calculated and analytically propagated through the layers using scattering matrices. RCWA thus directly provides the reflectance and transmittance of a given stack, in each diffracted order. The accuracy is directly related to the truncation of Fourier series, i.e. the number of calculated orders. Finally, the direct implementation of the analytical Fourier transform of basic patterns (squares, circles) enables a faster calculation and convergence.

3.1.3 Choice between the methods

The RCWA seems to be well suited for the following studies, since it is dedicated to periodic devices. However, it can be noticed that if the stack requires a fine vertical mesh, the computation time of RCWA drastically increases and is thus comparable, even possibly longer than using FDTD. Moreover, it appears difficult to compute the absorption in a given material of the stack. As using FDTD, such a computation derives from the electric field all over the grid. Using RCWA, these fields are post calculated from the Fourier space, thus possible Gibbs oscillations can affect the accuracy.

In our work, since the calculation of the 3D electromagnetic field was not yet available in our in-house developed RCWA, FDTD has been used for an accurate description of multilayer stacks.

3.1.4 Absorption efficiency and generation map calculations

In the numerical simulations based on FDTD or RCWA methods, we use the unpolarized sunlight as a light source. In the case of square lattice, due to the symmetry of the design, the unpolarized absorption could be obtained using one linearly polarized light, either TE orTM. On the contrary, for the pseudo-disordered structures, the unpolarized absorption is the averaged result of the simulation sunder TE and TM polarizations.

The absorption efficiency (*eff*) is considered:

$$eff = \frac{\int_{\lambda_{min}}^{\lambda_{max}} I(\lambda) A(\lambda) \lambda d\lambda}{\int_{\lambda_{min}}^{\lambda_{max}} I(\lambda) \lambda d\lambda} \qquad \text{Equation: 3-1}$$

in which λ is the wavelength, $I(\lambda)$ is the ASTM Air Mass 1.5G solar irradiance spectrum, and $A(\lambda)$ is the absorption spectrum of solar cell. It represents the ratio between the number of absorbed photons and the total number of incident photons in the incident solar spectrum.

In addition, assuming an efficiency of the carrier collection of 100%, the short circuit current density (J_{sc}) can be given by:

$$J_{sc} = \frac{e}{hc}\int_{\lambda_1}^{\lambda_2} \lambda A(\lambda)\frac{dI}{d\lambda}d\lambda \qquad \text{Equation: 3-2}$$

where e is the unit charge of the electron, h is the Planck's constant, c is speed of the light in the vacuum, λ is the wavelength, $A(\lambda)$ is the absorption, and $dI/d\lambda$ is the incident solar radiation intensity per wavelength corresponding to the AM1.5G solar spectrum.

3.2 Fabrication techniques

Structures optimized by optical simulations are patterned into samples including c-Si layers. In this work, patterning of the targeted complex structures is achieved by electron-beam lithography, which is quite flexible, and reactive ion etching.

3.2.1 Preparation of the thin film solar cell

In this work, we chose to pattern silicon layer with a high quality. Most of layer stacks are based on c-Si. More particularly, we used c-Si layers fabricated by the IMEC PV group, using the so called ‘epi-free processes’ [7, 8].

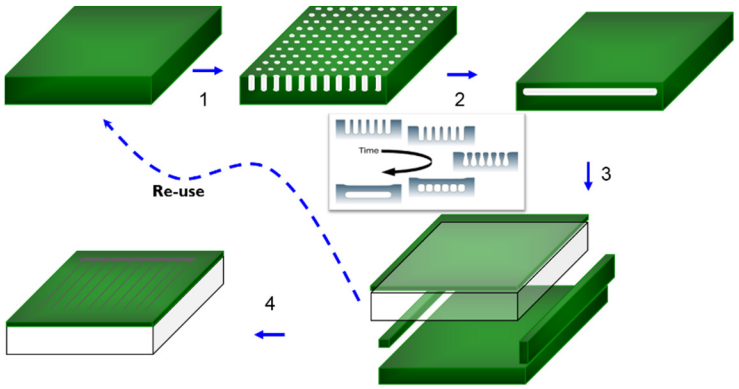

Figure 3-1. Epifree solar-cell process to generate the mono c-Si wafer, which is consisting of five steps of (1) pore formation, (2) annealing, (3) processing of the first cell side and bonding to a low-cost substrate, and (4) processing of the second side of the cell with re-use of the parent.

In this process (Fig. 3-1), the origin substrate (p-type Si, 100) is patterned by deep-UV lithography and reactive ion etching in order to generate pores in Si. The patterned Si wafer is then annealed above 1100°C in order to merge the upper part of Si pillars, so as to generate a c-Si layer on top of a porous layer. The obtained silicon film can then be detached from the initial Si wafer.

3.2.2 Lithography

In order to realize the micro- or nano-scale patterns in a tightly controlled way, nanolithography should be used. Available techniques include electron beam lithography (EBL), laser interference lithography (LIL) and nano-imprint lithography (NIL). While NIL and LIL are high throughput techniques, they are not suited to flexible fabrication of complex nanopatterns. Indeed, NIL needs the pre-patterning of a master stamp. For this reason, we chose to use EBL in this thesis, although patterning is then highly time consuming.

3.2.2.1 Electron-beam lithography

Electron-beam lithography (EBL) [9] is a nanofabrication technique which allows the direct writing of structures down to sub-10 nm resolution. It involves the exposure by a highly focused electron beam to dramatically modify the properties of an electro-

sensitive resist, enabling selective removal of either the exposed or non-exposed regions of the resist during the development step.

We have used an Inspect F FEI scanning electron microscope (SEM), including a laser alignment stage, connected to an Elphy Plus external module operated by the Raith lithography software. This equipment is available in the Nanolyon technological platform.

This system is operated with an electron beam at 30kV, with a current of around 10pA. This enables to realize a photonic crystal over 100×100µm in 20 min in a single exposure step to obtain a photonic crystal of hole with a 675nm period and a 220nm radius. In order to cover a millimeter square area, which is necessary to realize small prototypes of solar cells, exposed fields need to be stitched. This can be achieved using the available laser stage, but at the expense of the exposure time. Indeed, generating a 1mm² area takes 30 hours.

While this process was used to realize structures that can be characterized by micro-reflectometry (see below), larger structures are necessary to realize solar cells. To achieve this, we have attempted to reduce the exposure time by changing several parameters, like the diaphragm and spot size (related to the electron beam current), and the field size. Unfortunately, the effective lithography time does not depend so much on the beam current. Additionally, modifying the field size from 25µm² to 100µm² led to a duration decrease of only 18%, while leading to high mismatch at the field boundaries (Fig. 3-2a). This limited control illustrates that the lithography time is mainly related to the calculations performed to control the beam, rather than the resist exposure itself. Therefore, we started to develop a routine enabling to control directly the beam position, point by point, and reducing the number of points needed to realize a single hole.

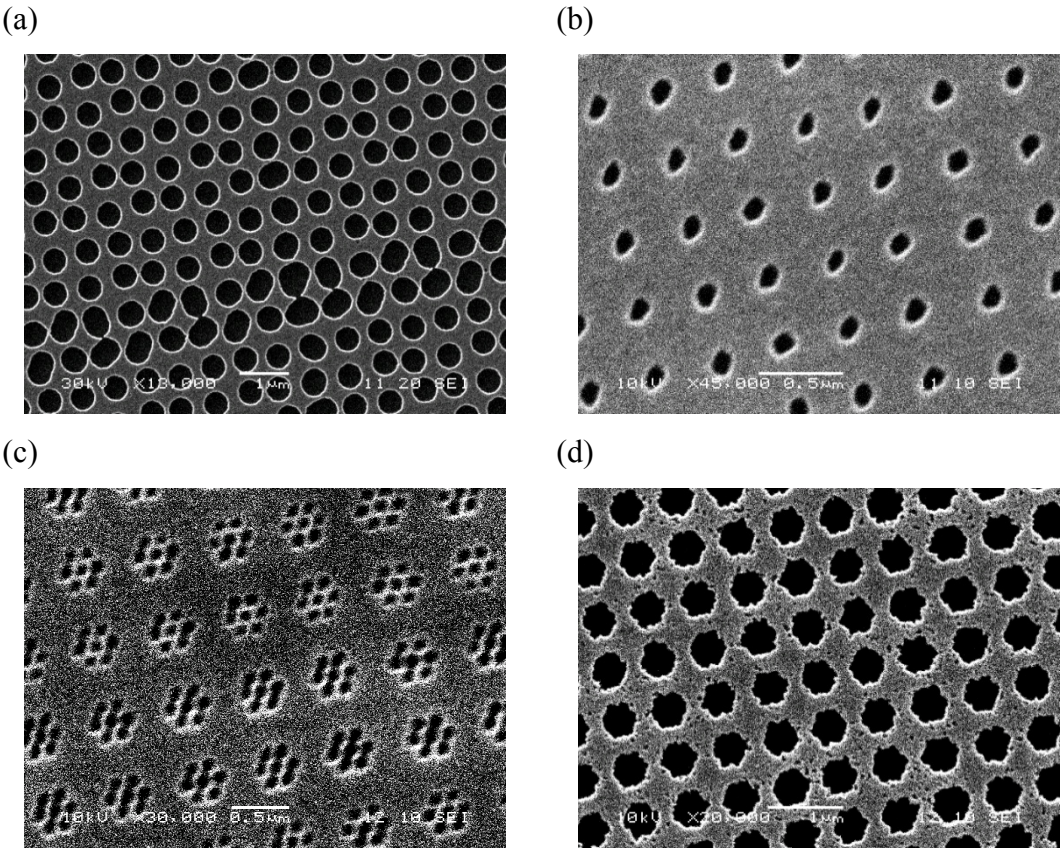

Figure 3-2. SEM images of the cylindrical hole patterns in c-Si stack. (a) the mismatch boundaries with a large writeflied size. Using the point element to establish the small radius of hole (b) and a large radius of holes with 7 points design with a low (c) and high dose value.

Firstly, holes with small radii can directly be obtained with a single point exposure, with a high dose (in micro Coulomb). (Fig. 3-2b). Secondly, for bigger radii, several points should be exposed to realize a single hole. The hole size can be adjusted by controlling the dose on each point, as shown in Fig. 3-2c and 3-2d. While this process enables a substantial gain in terms of lithography time, which leads a 20% gain in time compared to the directly elemental-based method, it is necessary to further control the parameters to realize holes with well-controlled shape and size. This optimization was beyond the scope of this PhD.

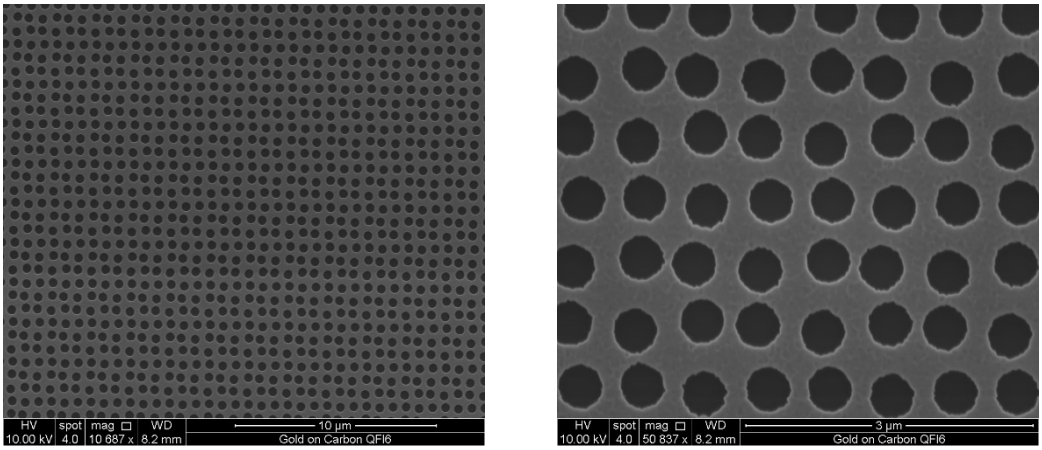

Figure 3-4. SEM images of the cylindrical hole patterns in a large surface area.

Considering the difficulty to realize millimeter square areas using our EBL system, we have considered using an industrial EBL machine (JEOL6300FS), available in the Renatech PTA platform in Grenoble. It was then possible to realize photonic crystals on 1mm² in 10 hours. From the SEM images shown in Fig. 3-4, we can realize the obtained holes are quite homogenous and circular. We chose to use this equipment to realize complex photonic patterns over wide areas. These last lithographies were done by Céline Chevalier.

3.3.3.2 Other lithography technologies

Laser interference lithography (LIL), which is also called 'laser holographic lithography (LHL), is a pattern definition technique capable of defining micrometre and sub-micrometre large area periodic patterns [2, 3, 10, 11]. The basic principle is the interference between two optical beams, split from a coherent laser source. When recombined, these beams form a standing wave at the surface of the sample covered by a photosensitive resist.

Nanoimprint lithography (NIL) is a nonconventional lithographic technique for high-throughput patterning of polymer nanostructures at great precision and at low costs [12, 13]. Compared to the traditional lithographic technologies, e.g. EBL, LIL, which the patterned structure is achieved through the use of electrons or photons by the modification of the properties of the photoresist, NIL relies on direct mechanical deformation of the resist material. Therefore, it can achieve resolutions beyond the limitations set by light diffraction or beam scattering that are encountered in conventional techniques.

3.2.3 Reactive-ion etching

Reactive-ion etching [14, 15] (RIE) is a widely used plasma etching method, well suited to micro- and nano- structure fabrication. This dry etching method, involves a high-speed stream of glow discharge (plasma) of an appropriate gas mixture, to transfer the patterns from the photoresist to the underlying layers. Different or mixed gases are flowed in the chamber under a RF powered electromagnetic field, creating a plasma, which ionizes the gas molecules. The positive ions tend to drift toward the wafer platter, where they collide with the samples to be etched. At the surface of the samples, ions transfer their kinetic energy, and/or chemically react with the layer.

(a) (b)

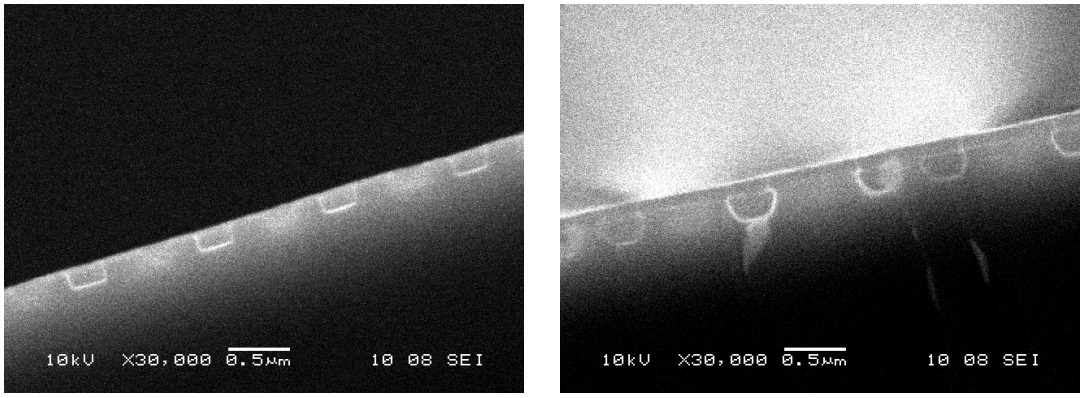

Figure 3-5. Profile view of the patterns in the c-Si stack: (a) vertical or (b) rounded sidewall.

Key parameters need to be adjusted to realize the targeted patterns. They include the chamber pressure, the composition of the gas mixture, and their corresponding flow rate, the plasma power and the etching time. For example, a vertical sidewall pattern in c-Si stack shown in Fig. 3-5a is obtained with mixture of SF_6 and Ar with low pressure (15mTorr). Conversely, if we need a rounded sidewall shape, the recipe should be more chemical, with a high pressure (100mTorr), and a gas mixture of $SF_6/CHF_3/O_2$. As the patterns with the vertical sidewall will be presented in the thesis, we will adopt the recipe as shown in Table. 3-1 to perform the RIE process.

Table. 3-1 Selectivity of masking material to silicon in the RIE processes.

Etching Material	Gas	Flow (sccm)	Pressure (mTorr)	P_{RF} (W)	Etching Rate (nm/s)
SiO_2	CHF_3	45.5	15	100	0.17
c-Si	SF_6	5	15	50	2.86
	Ar	5			

3.3 Characterization techniques

We first observe the topography of the fabricated sample to check out its quality, and to enable the comparison between numerically optimized parameters, and the geometry really achieved. This is achieved by scanning electron microscopy (SEM) and atomic force microscopy (AFM) measurements. The subsequent step is to optically assess the quality of the fabricated sample.

3.3.1 Optical assessment

If the photonic structures are realized by EBL, their area will be limited to a few 100x100μm². Therefore, the absorption of the thin film solar cells cannot be measured using an integrating sphere. Thus, we will resort to a micro-reflectivity set-up that was built at INL.

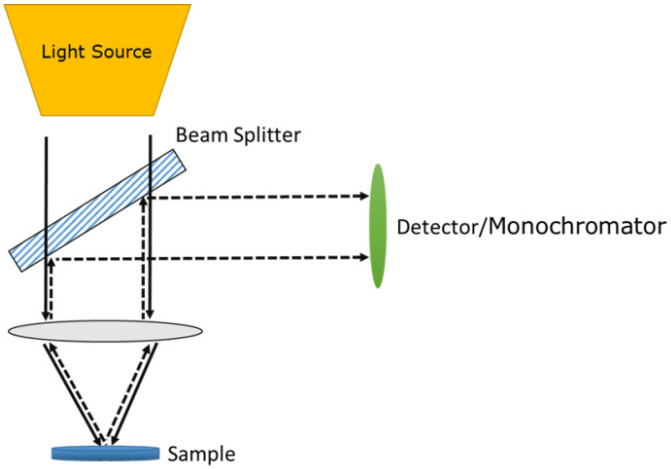

Figure 3.6. Micro-reflectivity set-up. A white light is focused on the nanostructure thanks to a long working distance objective. The back-reflection of the structure is analyzed through a spectrometer.

The schematic view of the set-up is shown on Fig. 3.6. On the top, a nearly collimated white light is focused onto the nanopatterned structures through a long-focal microscope objective. The back reflection of the structure is collected through the same objective lens and then analysed using a spectrometer. This setup enables to measure pattern areas smaller than 100x100µm². However, in order to reduce the numerical aperture, and therefore the collection of angles of incidence, one should use patterned areas as large as possible. Lastly, one should note that this measurement may be used to evaluate the absorption only if the transmission is zero, which is the case if the patterned layer stands on a metallic back reflector. Moreover, this measurement method does not guarantee that all non-absorbed photons are collected.

To overcome these limitations, or to assess the appropriateness of micro-reflectivity measurements for such structures, absorption measurements should be made using an integrating sphere on a limited set of nanopatterns realized over millimetre or centimetre wide areas.

References and links

1. J. R. Nagel and M. A. Scarpulla, "Enhanced absorption in optically thin solar cells by scattering from embedded dielectric nanoparticles," Optics express **18**, A139-A146 (2010).
2. X. Meng, G. Gomard, O. El Daif, E. Drouard, R. Orobtchouk, A. Kaminski, A. Fave, M. Lemiti, A. Abramov, and P. R. i Cabarrocas, "Absorbing photonic crystals for silicon thin-film solar cells: Design, fabrication and experimental investigation," Solar Energy Materials and Solar Cells **95**, S32-S38 (2011).
3. G. Gomard, X. Meng, E. Drouard, K. El Hajjam, E. Gerelli, R. Peretti, A. Fave, R. Orobtchouk, M. Lemiti, and C. Seassal, "Light harvesting by planar photonic crystals in solar cells: the case of amorphous silicon," Journal of Optics **14**, 024011 (2012).
4. M. Moharam and T. Gaylord, "Rigorous coupled-wave analysis of planar-grating diffraction," JOSA **71**, 811-818 (1981).
5. A. Taflove and S. C. Hagness, "Computational electrodynamics: the finite-difference time-domain method," Norwood, 2nd Edition, MA: Artech House, l995 (1995).
6. F. Lumerical, "Solutions 8.0."
7. V. Depauw, X. Meng, O. El Daif, G. Gomard, L. Lalouat, E. Drouard, C. Trompoukis, A. Fave, C. Seassal, and I. Gordon, "Micrometer-thin crystalline-silicon solar cells integrating numerically optimized 2-D photonic crystals," Photovoltaics, IEEE Journal of **4**, 215-223 (2014).
8. V. Depauw, Y. Qiu, K. Van Nieuwenhuysen, I. Gordon, and J. Poortmans, "Epitaxy-free monocrystalline silicon thin film: first steps beyond proof-of-concept solar cells," Progress in Photovoltaics: Research and Applications **19**, 844-850 (2011).
9. C. Vieu, F. Carcenac, A. Pepin, Y. Chen, M. Mejias, A. Lebib, L. Manin-Ferlazzo, L. Couraud, and H. Launois, "Electron beam lithography: resolution limits and applications," Applied Surface Science **164**, 111-117 (2000).
10. X. Meng, V. Depauw, G. Gomard, O. El Daif, C. Trompoukis, E. Drouard, C. Jamois, A. Fave, F. Dross, I. Gordon, and C. Seassal, "Design, fabrication and optical characterization of photonic crystal assisted thin film monocrystalline-silicon solar cells," Optics Express **20**, A465-A475 (2012).

11. C. Lu and R. Lipson, "Interference lithography: a powerful tool for fabricating periodic structures," Laser & Photonics Reviews **4**, 568-580 (2010).
12. L. J. Guo, "Nanoimprint lithography: methods and material requirements," ADVANCED MATERIALS-DEERFIELD BEACH THEN WEINHEIM- **19**, 495 (2007).
13. C. Trompoukis, O. El Daif, V. Depauw, I. Gordon, and J. Poortmans, "Photonic assisted light trapping integrated in ultrathin crystalline silicon solar cells by nanoimprint lithography," Applied Physics Letters **101**, 103901 (2012).
14. H. Jansen, H. Gardeniers, M. de Boer, M. Elwenspoek, and J. Fluitman, "A survey on the reactive ion etching of silicon in microtechnology," Journal of micromechanics and microengineering **6**, 14 (1996).
15. S. Grigoropoulos, E. Gogolides, A. Tserepi, and A. Nassiopoulos, "Highly anisotropic silicon reactive ion etching for nanofabrication using mixtures of SF6/CHF3 gases," Journal of Vacuum Science & Technology B **15**, 640-645 (1997).

4. Numerical optimization of the photonic crystal structure assisted thin film solar cell

In this chapter, we will investigate numerically the influence of different kinds of PC patterns in thin c-Si (less than 2μm thick) solar cells, as well as the corresponding optimization of the absorption. We focus on arrays of cylindrical holes and inverted nano-pyramids structure. The comparisons of absorption spectra between the different structures will be analyzed. The corresponding generation rates of the solar cells are calculated in order to perform the electrical simulations. The PC patterned thin film solar cells stack was considered firstly on the silicon substrate and then on the metal back reflector. At last, a dual patterned cylindrical holes design is proposed in order to further increase the absorption of the solar cells, especially in the long wavelength range.

4.1 Thin film solar cells stack composition

As introduced previously, the single homojunction made of c-Si cannot take full advantage of the solar energy. Therefore, the simplified heterojunction concept by the deposition of a doped a-Si:H layer on the crystalline wafer [1, 2] is considered, so as to target a higher conversion efficiency.

The considered thin film heterojunction silicon solar cells typically consist of, from the top to the bottom, an ITO front electrode, an amorphous hydrogenated silicon (a-Si:H) layer, then a lowly doped c-Si layer acting as the main active region lying on a highly doped c-Si substrate, as described in Fig 4-1a. The PC patterns are introduced on the top layers of the solar cells as shown in Fig. 4-1b and 4-1c, including the active c-Si layer. In order to enable an easier surface passivation, the a-Si:H layer is supposed to be deposited after the etching and is thus considered continuous. In preliminary investigations, unboned thin films are considered, without rear metallic contact and reflector.

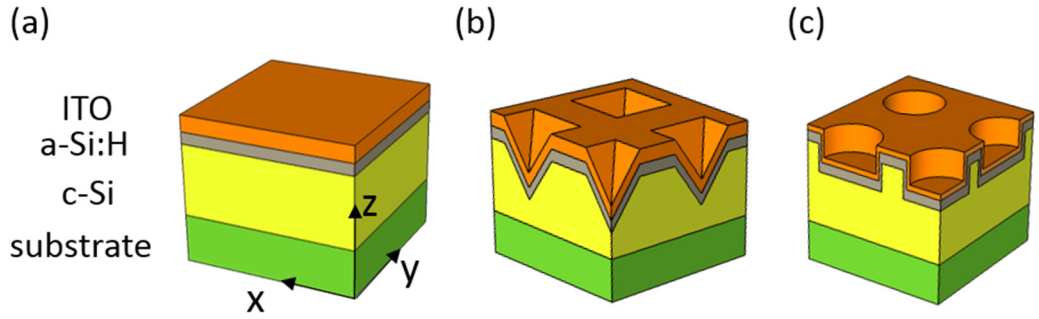

Figure. 4-1 Schematic view of the solar cells stack (a) and the inverted nano-pyramids (b) or cylindrical holes (c) structure applied to the top layers, including the active layer.

In order to characterize the net absorption, the absorption in the active layer including the nanopatterns needs to be measured. For the better understanding of the influence of the geometrical parameters of the PC structure assisted the thin film solar cells and meanwhile to obtain the maximum enhancement, the optimization on the geometrical parameters of PC structure will be carried out.

4.2 Simulation detailed methodology

In this chapter, we simulated the structures with the commercial software 'Lumerical' based on the finite difference time domain numerical method (FDTD) described in the previous chapter. In the settings of the software, the mesh setting (mesh=3 over 8, non-uniform mesh) and the simulation time (1000fs, depending on the thickness of the stack) ensure a good accuracy within reasonable computational time and memory. For the boundaries condition, the perfectly matched layers (PML) were used in the z direction on both the top and bottom. Due to the square symmetry of the periodic PC structure, only one single x-axis polarized light source was used in the simulations. Besides, symmetric (along y-axis) and anti-symmetric (along x-axis) boundary conditions enable to reduce the simulation requirements under normal incidence.

As discussed in the previous sections, the net absorption of the thin film solar cell should be calculated then optimized in the numerical process. As we use the continuous a-Si:H and ITO layers to cover the c-Si layer in the design, it is necessary to detect the absorption of the c-Si layer, named the 'local absorption', by distinguishing the other materials. However, in the FDTD simulations, the structure geometry is described on an orthogonal mesh, as well as the monitors. Therefore, for the inverted nano-pyramids and cylindrical holes, monitors have been set as close as possible to the profile, following a staircase approximation that is also used for the index profile of the material. If there are two absorbing materials, a series of staircase monitors are required in each material. The absorption in the corresponding layer is thus calculated by making the difference of the summation of all detected incident light and the emergent light in each staircase monitor, and possibly by the average between the two surrounding staircase monitors.

4.3 Optimization of PC structure in thin film solar cells on silicon substrate

The transverse schematic view of the thin film solar cells stack is shown in Fig. 4. The two considered possible PC patterns, i.e. the inverted nano-pyramids and cylindrical holes structures, were designed in the top layers including the active layer shown in Fig. 4-2a and 4-2b respectively. In the case of the inverted nano-pyramids,

the ITO layer is supposed to have a thickness of 50 nm in both the top and oblique sidewalls, while it is 5 nm on vertical sidewall, in the case of the cylindrical holes. Such structures can correspond e.g. to epitaxially grown thin films of Si on silicon substrates. Even if the efficiency might appear limited, such devices are still of great interest to study the patterning of the front surface and to address passivation issues. The optical indices considered are shown in annex 1, in which the index of the grown c-Si in slightly different from the one of the substrate.

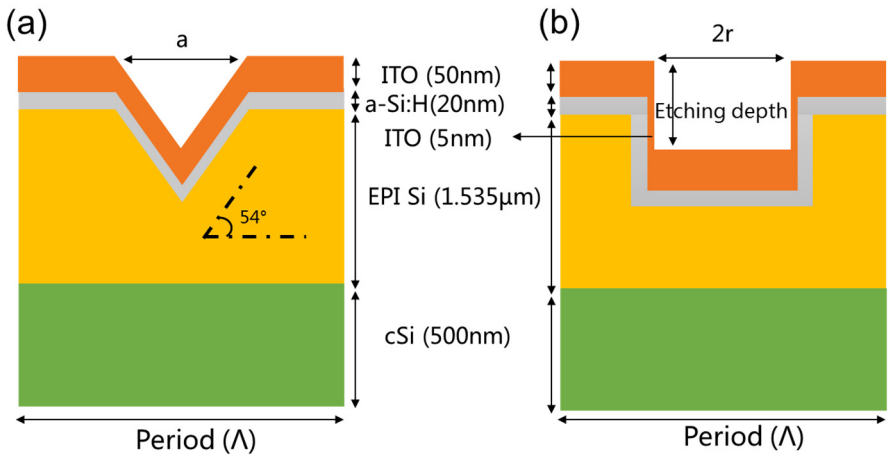

Figure 4-2. Schematic view of the inverted nano-pyramids (a) and the cylindrical holes (b) structures in the silicon-substrate stack.

In the nano-pyramid patterns, the angle (54.7°) is dependent on the silicon property and the relevant anisotropic wet etching process [3]. Potassium hydroxide (KOH) is the typical anisotropic wet etchant for the silicon, which the silicon crystal planes (100) are etched 200 times faster than the planes (111). Finally, the etching is terminated when only the slow etching planes (111) are presented. The etching depth is determined by the mask opening (Λ and *ff*) and the angle between the (111) and (100) planes, 54.7°[4].

In the numerical simulation, we will consider the parameters of the PC structure (Fig. 4-2), period (Λ), the air surface of the filling fraction (*ff*, by a^2/Λ^2 for the nano-pyramids or $\pi r^2/L^2$ for the cylindrical holes, $a(r)$ being the length (radius) of the air hole) and the etching depth (only in the case of cylindrical holes structure, since for the nano-pyramids structure this parameter is set by the angle 54.7° from the wet etching of the c-Si). For sake of simplicity, we restrict to three different periods (300nm, 450nm and 600nm) to perform the optimization for both inverted nano-pyramids and cylindrical

holes patterns. Then we tuned the other parameters, i.e. *ff* and the etching depth, to find the highest efficiency with the two types of the patterned structure in each period.

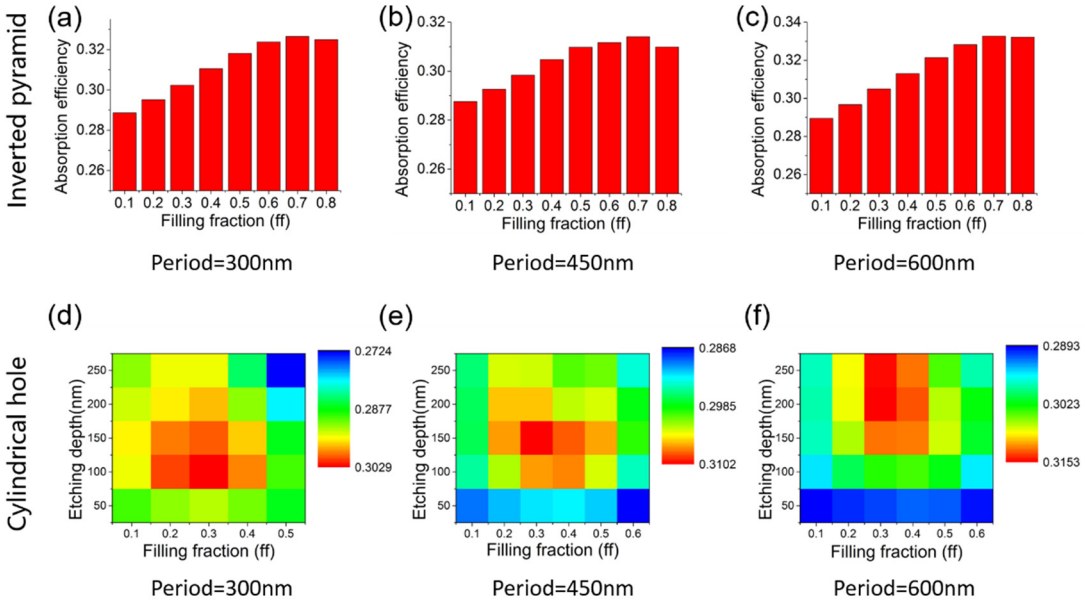

Figure 4-3. The absorption efficiency of active layer (EPI silicon) with two types of PC patterned structures: inverted nano-pyramids (top, a, b, c) and cylindrical holes (bottom, d, e, f) and with the different periods: 300nm (a, d), 450nm (b, e) and 600nm (d, f).

The absorption results about the inverted nano-pyramids structures are shown in Fig. 4-3a, b and c. The larger absorption is obtained for large (0.7), but not the largest (0.8) *ff* for each period. Considering the three different periods with the corresponding optimized *ff*, the largest period and so the deepest etching leads to the largest absorption. That is mainly because the large volume of the patterns will provide the more possibilities of the light coupled into the increased modes [5, 6].

Concerning the results of cylindrical holes are shown in Fig. 4-3d, e and f, it is noticeable that over the considered range and for the given steps, only one maximum is observed. The hot spot range with the parameter of the *ff* is relatively stable in the 0.2-0.4 range. The optimal etching depth increases with the period. Similarly, in the case of the inverted nano-pyramids, the optimized design with a large period of 600 nm exhibits the best absorption efficiency.

(a) (b)

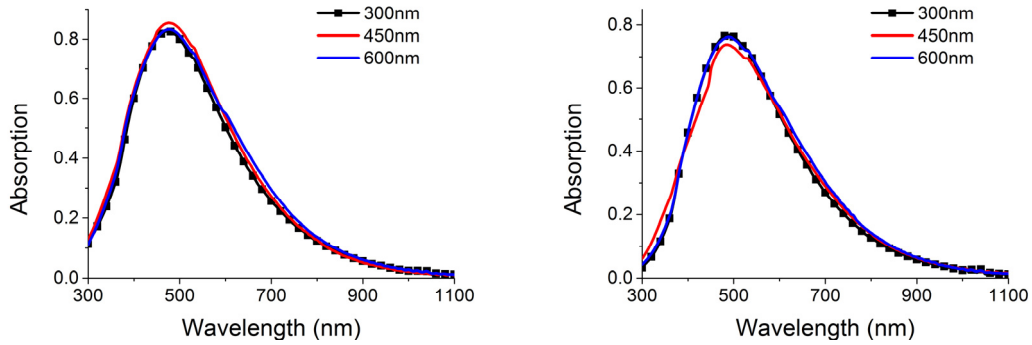

Figure 4-5. Absorption spectra of c-Si with the inverted nano-pyramids (a) and cylindrical holes (b) designs in a period of 300, 450 and 600nm with filling fraction (ff) of 0.3 and etching depth of 200nm

Fig. 4-5 show absorption spectra of the inverted nano-pyramids (Fig. 4-5a) and cylindrical holes (Fig. 4-5b) designs with the optimized parameters in different periods. In the designs with inverted nano-pyramids structure, the structures with the three periods exhibit almost same performance in the wavelength range of 300-400nm. In the wavelength range of 400-600nm, the period 450 has a best absorption, conversely, the large period of 600nm has a better performance in the wavelength range of 600-1100nm. In designs with cylindrical holes structure, the period of 450nm has a relative high absorption in the wavelength range of 300-400nm, while it is lower than the period 600nm in the rest of wavelength range. In the consequence, the absorption spectra are not clear to tell the best design, so that J_{sc} will be used in the following. It also could be noted that the period is a critical parameter in the PC structure, which needs to be optimized.

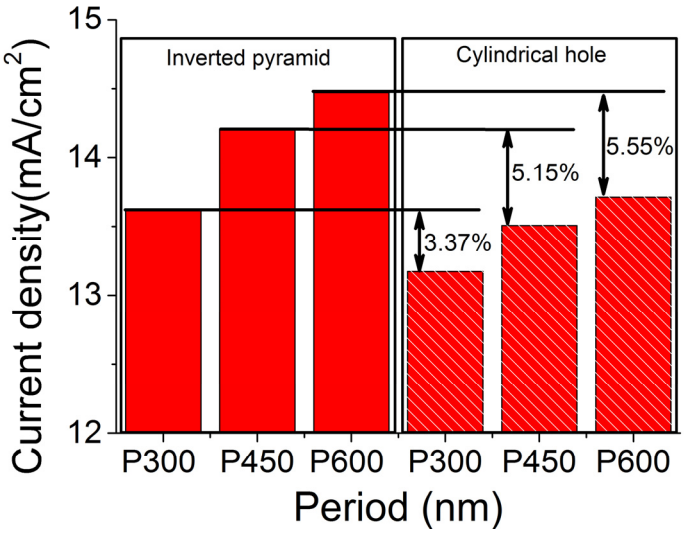

Figure 4-6. The comparison of the best current density (J_{sc}, mA/cm²) for each period (300, 450 and 600nm) with the nanopatterned structure: inverted nano-pyramids structure and the cylindrical holes structure, in preliminary step.

The maximal achievable short-circuit current (J_{sc}) could directly indicate the performance of the thin film solar cells, so the J_{sc} of the optimized designs with different periods for both the nano-pyramidal and cylindrical patterns are summarized in Fig. 4-6. Firstly, for both designs, the optimized design with largest period leads to the best J_{sc}. Secondly, it can be seen that the J_{sc} of the inverted nano-pyramids is higher than the one of the corresponding cylindrical holes structure. Then, in order to compare the light trapping scheme of these two structures, we will analyze the absorption spectra corresponding to the highest J_{sc} design with the different patterned designs.

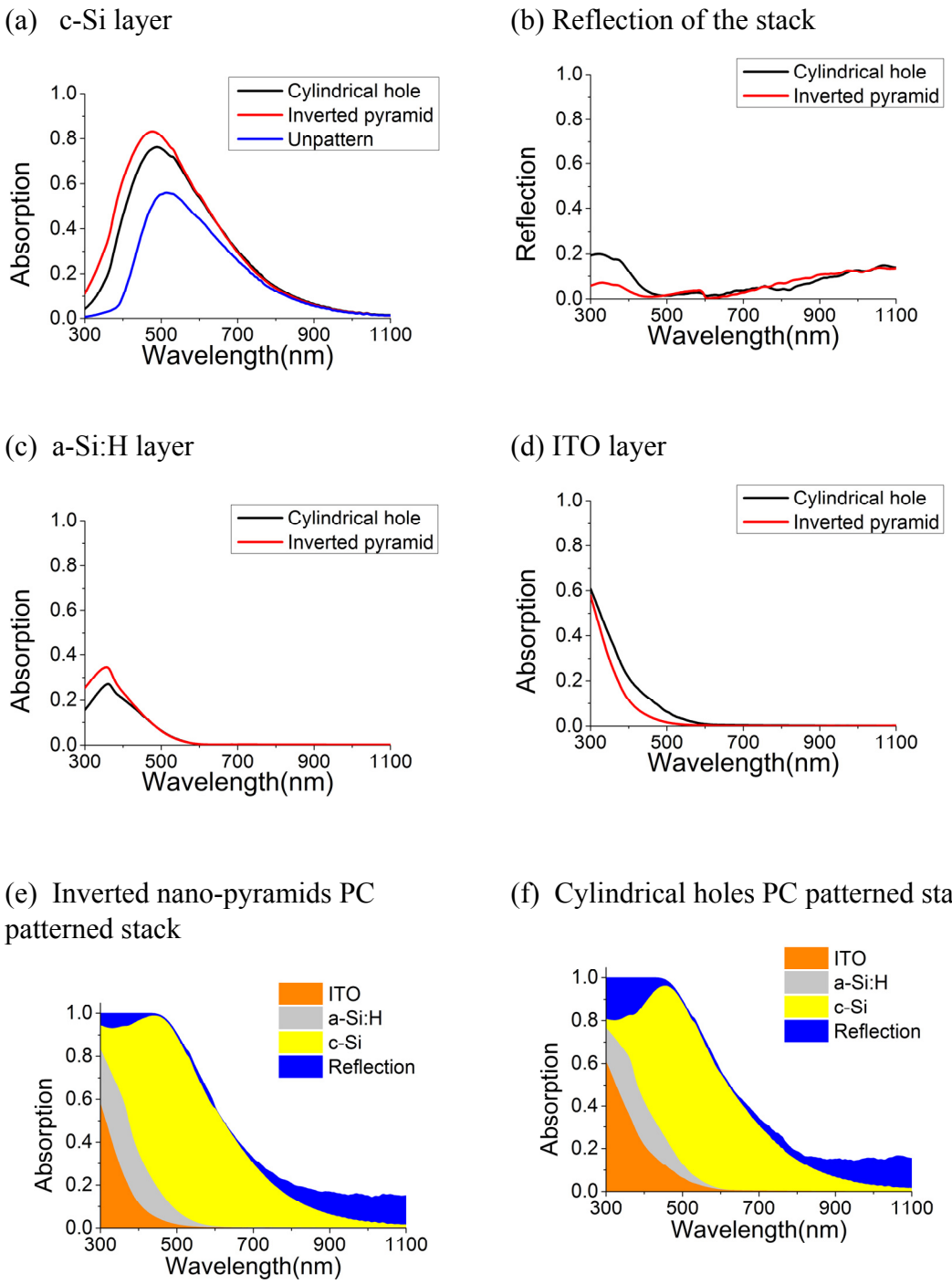

Figure 4-7. Absorption spectra comparison between the inverted nano-pyramids structure and the cylindrical holes structure in each layers of the c-Si (a) (including a reference unpatterned flat stack), a-Si:H (b) and ITO (c), as well as the reflection spectra (d) by the aid of the local monitors. The light distribution in the stacks with the inverted nano-pyramids structure (e) or the cylindrical holes structure (f).

Absorption spectra of each layer in the silicon-based substrate of the thin film solar with the two best different patterns for the period 600 nm are shown in Fig. 4-7. Firstly,

for the c-Si layer in Fig. 4-7a, compared with the unpatterned design, both the PC patterned designs exhibit a higher absorption in the 300-1000nm wavelength range. More precisely, the stack with the inverted nano-pyramids has a higher absorption than the cylindrical holes below 500nm. This corresponds first to a lower reflection of the inverted nano-pyramids patterned stack (Fig. 4-7b). This is derived from a gradual change of the index by the inclinations of the nano-pyramidal shape at the wavelength-scale.

Secondly, we will consider the absorption of the other layers, i.e. a-Si:H and ITO, with these two different PC structures. In the absorption spectra of the a-Si:H layer shown in the Fig. 4-7c, the absorption is also higher with inverted nano-pyramids than with the cylindrical holes structure in the wavelength below 450nm, . This confirms a better anti-reflectivity with the inverted nano-pyramids design. The parasitic absorption of the ITO layer (Fig. 4-7d), is lower using inverted nano-pyramids than using the cylindrical holes structure.

It is noticeable that for both structures the parasitic absorption is larger at short wavelengths, whereas, in the long wavelength range, the light can reach the c-Si, but the absorption is quite low. Therefore, it is necessary to add a back reflector to simply increase the optical path length in order to further enhance the absorption in the c-Si layer.

4.4 PC structure applied to thin film solar cells on a metal-substrate stack

In this section, we will use the complete thin film solar cells stack with the back metal instead of the silicon substrate. Meanwhile, we add an optical spacer [7-9] between the back surface field (BSF) layer and a back metallic contact as depicted in Fig. 4-8, in order to reduce the parasitic absorption in the metal. The patterns are inverted nano-pyramids (Fig. 4-8a and c) and cylindrical holes (Fig. 4-8b and d).

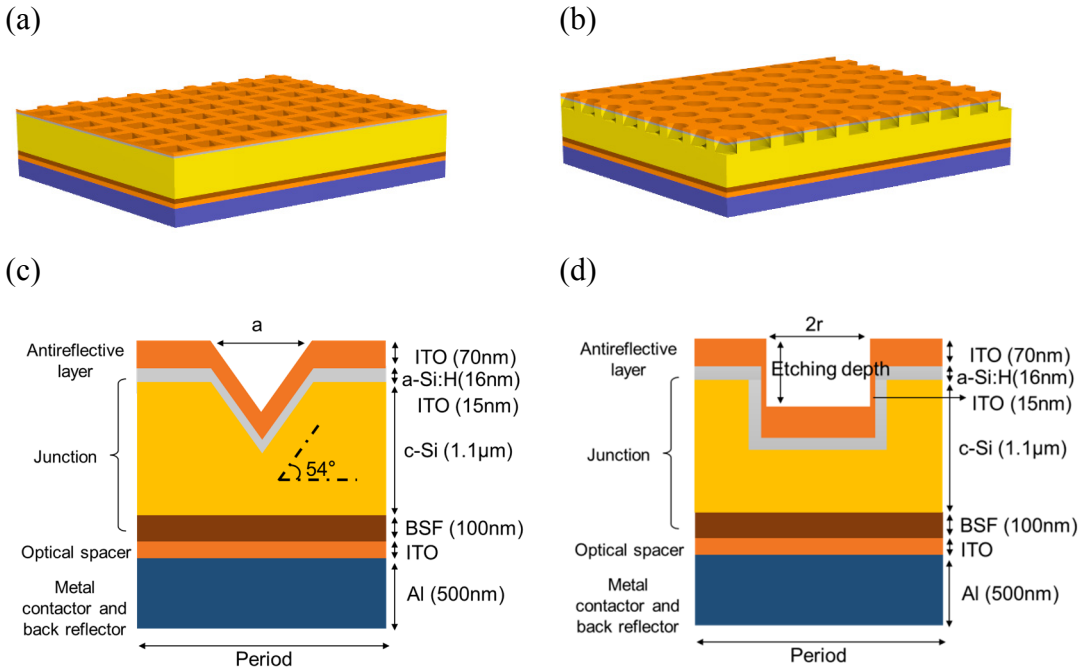

Figure 4-8. Schematic view of the inverted nano-pyramids (a, vertical cross section c) and the cylindrical holes (b, vertical cross section d) structures.

If this back interface is expected to increase the efficiency, by increasing the optical path length in the active c-Si layer and thus the absorption, it requires also a complex fabrication process including a bonding step. In our numerical calculations, a 1.1µm thick weakly doped c-Si layer was chosen as the active layer, meaning that the absorption in the BSF (modeled with the same index as the c-Si for sake of simplicity) is not taken into account, due to the high doping concentration if this layer. This could correspond to a film obtained by the epi-free technique (see previous chapter), which the corresponding optical indices are given in annex 1.

4.4.1 Absorption optimization

The optimization process on this complete thin film solar cells stack is almost similar as before, but with additional parameters. From the analysis in the previous section, the period is an important parameter so that it has been tuned during this optimization process. As the thickness of the optical spacer could change the absorption of the thin film solar cells, we will consider it as another parameter that needs to be optimized. Since we introduced two additional parameters compared to the previous

case, the protocol has been set to avoid a time consuming full sweep of all the parameters.

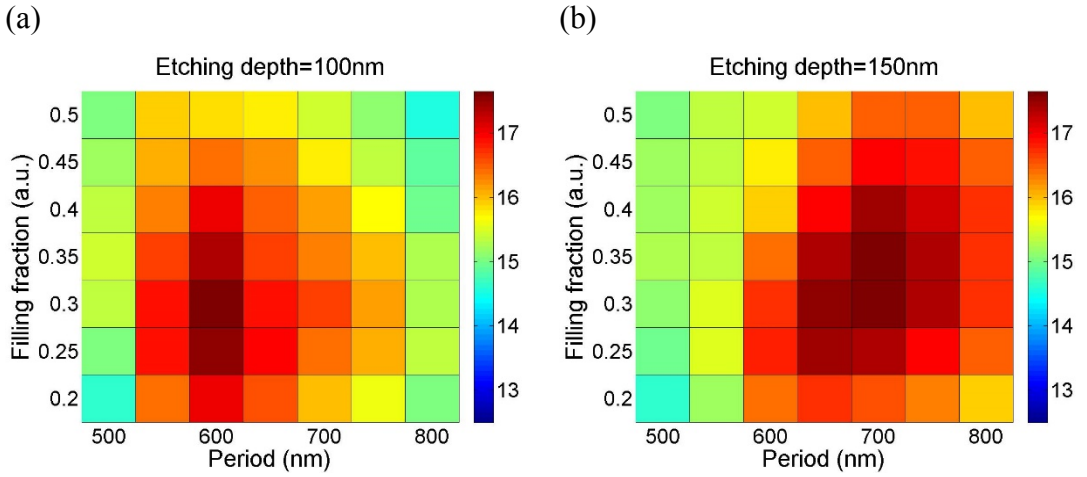

Figure 4-9 Map of the current density (J_{sc}, mA/cm²) according of the cylindrical holes structure: the period and the filling fraction (ff) for two etching depths, which are corresponding to the first (a) and the second (b) hot spot ranges in the first optimization step with a given thickness of the optical spacer layer.

For the cylindrical holes, at the beginning of the optimization of all the parameters, the thickness of the optical spacer was set to 110 nm. It will be tuned after the preliminary optimization of the rest of parameters. Other parameters are tuned, i.e. period in the range [500;800] nm, filling fraction [0.2;0.5] and etching depth [50;200] nm, with steps of 50 nm for the period, 0.05 for the filling fraction (*ff*) and 50 nm for the etching depth, to find the hot spot range, in which the parameters are closer to the optimal values. Due to the large step used in the first optimization, we take the top two hot spot ranges (Fig. 4-9) in the following optimization process, corresponding to the highest J_{sc} (17.65mA/cm², period 600nm, *ff* 0.3 and etching depth 100nm) shown in Fig. 4-9a and the second highest J_{sc} (17.63mA/cm², period 700nm, *ff* 0.3 and etching depth 150nm), shown in Fig. 4-9b. Thirdly, the parameters of the two highest J_{sc} (see in 1st step of Table. 4-1) in the previous step were used and then we just changed the thickness of the optical spacer layer parallel to find the best in a precise step. Systematically, the similar refinements were performed by using the parameters of the highest J_{sc} in the previous and then only one variable was tuned, such as the period or the *ff*, with smaller steps each time. After several circular simulations (see Table 4-1), the optimized parameters of the thin film solar cells could be determined.

Table 4-1. The optimization process of the cylindrical holes structure.

Step	J_{sc}(mA/cm²)	Period (nm)	Filling fraction (*ff*)	Etching depth(nm)	Optical spacer(nm)
Initial	/	/	/	/	110
1st	17.65	600±50	0.3±0.05	100±50	110
1st	17.63	700±50	0.3±0.05	150±50	110
2nd	17.71	600	0.3	100	100±5
3rd	17.96	600	0.3	110±5	100
4th	17.99	580±10	0.3	110	100
5th	18.02	580	0.29±0.01	110	100
6th	18.02	580±10	0.29	110	100

It can be noticed that the optimized *ff* = 0.29 is far from extreme values (*ff* ~ 0 or *ff* ~ 1), since *ff* ~ 0 would lead to a too weak coupling on the incident light, and *ff* ~ 1 would lead to multiple scattering. If *ff* is in between, the situation corresponds to that of PC with bandgaps and band-edge modes, so slow Bloch modes, which will enhance the absorption [10].

The same optimization process is performed on the inverted nano-pyramids PC structure, where the etching depth is related to period *ff*. Such a "manual" method has been preferred to a more "blind" optimization algorithm such as genetic algorithm or particle swarm optimization. The optimized J_{sc} with the cylindrical holes PC structure is 18.02mA/cm², with a period of 580nm, a *ff* of 0.29, an etching depth of 110 nm and a 100 nm optical spacer. The optimized inverted nano-pyramids PC structure will lead to a J_{sc} value of 23.59mA/cm², with a period of 800 nm, a *ff* of 0.85 and a 110nm thick optical spacer. Compared to the unpatterned design (11.52mA/cm²), which corresponds to the highest J_{sc} with a 110 nm thick optical spacer, based on the parameter of the optimized inverted nano-pyramids structure, both of the nanopatterned structures will lead to a larger J_{sc}, with a 56.4% gain with the cylindrical holes PC structure (18.02mA/cm²), and a 104.8% relative increase with the inverted nano-pyramids PC structure (23.59mA/cm²) (Fig. 4-10a).

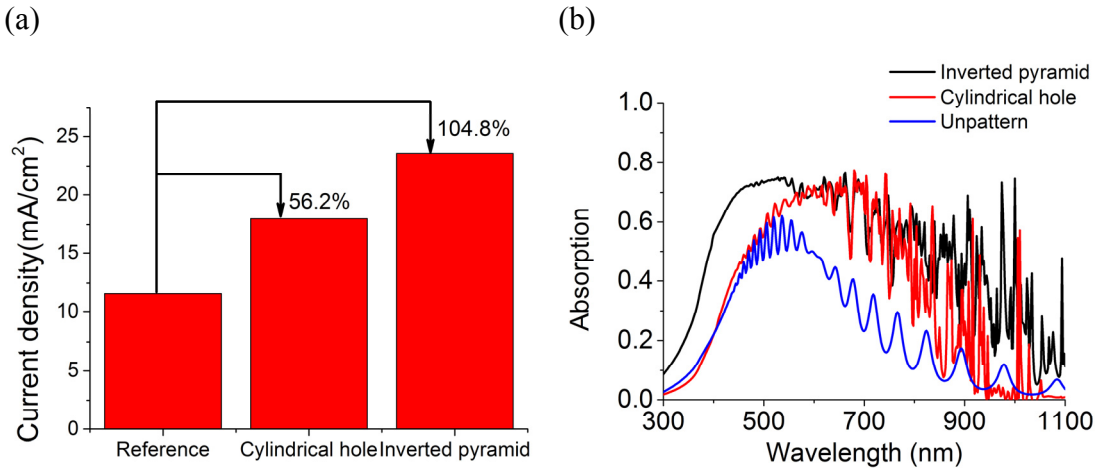

Figure 4-10. (a) The comparison of the current density (J_{sc}) of the optimized inverted nano-pyramids, cylindrical holes and the unpatterned structure (b) The comparison of the absorption spectra between the inverted nano-pyramids, cylindrical holes and the unpatterned structure in the complelte thin film solar cells.

In order to deeply analyze the increase of the J_{sc} by aid of the PC structure, we will focus on the local absorption spectra of the c-Si layer in the optimized designs for the two different PC structures and the reference of the unpatterned design. From the absorption spectra of the two PC structures and the reference unpatterned structure shown in Fig. 4-10b, the absorption of the patterned structures are clearly above the unpatterned structure, especially for the inverted nano-pyramids structure. More precisely, in the short wavelength range of 300-500nm, the anti-reflective effect works better on both PC structures, resulting in a high absorption. Among them, the solar cell with inverted nano-pyramids structure has the highest absorption, as previously observed and justified. Meanwhile, it could be noted that no sharp absorption peak appears in the short wavelength range, where the penetration length of the photons in the c-Si is shorter than the absorbing layer thickness. For the wavelength range from 500 to 700nm, several absorption resonances corresponding to the Fabry-Perot modes come out by the reflection occurring on the c-Si/ITO/Al interfaces. Compared to the unpatterned flat structure configuration, in the wavelength range of 700-1100nm, the cylindrical holes and inverted nano-pyramids exhibit dense and irregular absorption resonances. These resonances correspond to Bloch modes in the strongly dispersive material and the multimode waveguide. Thanks to the patterns, the incoming light can

be coupled into these modes and then feel an increased absorption by light trapping mechanism.

Furthermore, it should be noted that the configuration of the stack for unpatterned case is based on the parameters of the optimized inverted nano-pyramids design, in which the J_{sc} is higher than the one based on the cylindrical case. Despite an overestimated absorption due to the fitted index above 700nm in the numerical simulations, the absorption in the design with the inverted nano-pyramids structure is much better than the one with cylindrical holes. This tendency is similar to previous results in the literature for thicker films [11].

However, focusing on the large wavelength range of the two nanopatterned PC structures, both of them exhibit sharp and densely packed peaks. The inverted nano-pyramids PC structure exhibits better performance, which all the sharp dense peaks are above the reference structure. Conversely, the cylindrical holes PC structure exhibits relatively weaker performance, especially in the wavelength range between 900 and 1100nm, in which the valleys of the peaks in the absorption spectrum are lower than in the reference structure. So it means the light trapping abilities of these PC structure should be developed, especially for the cylindrical holes case in the large wavelength range of the spectrum. These researches of the development on the advanced design will be introduce in the following chapters.

4.4.2 Generation rate

As the absorption of the active layer with two kinds of PC structures has been already studied, we are now considering possible opto-electronic simulations. As described in chapter 2, the required generation rate parameter (G) is given by the equation.

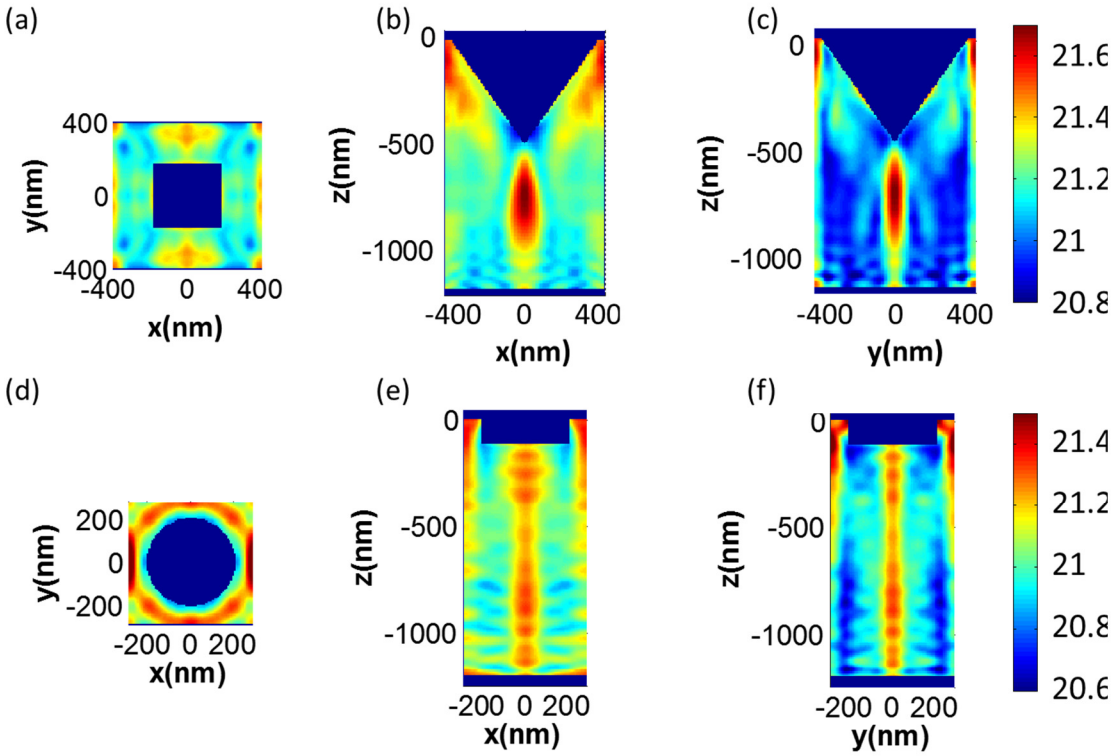

Figure 4-11. Generation rate ($cm^{-3}s^{-1}$) of electron-hole pairs of solar cells device with the inverted nano-pyramids (a, b and c) and cylindrical holes (d, e and f) with top view (a, d) or cross views (b, c, e and f) in logarithmic scale. The dark blue areas corresponding to 0.

Then we chose generation rate on several cross sections on the top and the profile of the c-Si layer, which is the middle depth of the pattern (≈55nm) and the half of the period (the central cross-section) in the x/y direction. Based on these images (Fig. 4-11), we can clearly see the distribution of generated electrons. The higher generation rate is in both sides of the structure. In the contrary, at the vertex point of the etching, the generation rate value is very low, leading possibly to low surface recombination.

4.5 Combined front and rear PC cylindrical holes structure

The previous absorption enhancement might appeared limited in the long wavelength range, especially for the cylindrical holes structure. Therefore, a longer photon lifetime is necessary to take full profit of the optical resonances of the structure. One of the solutions is to introduce the PC structure also at the back interface to increase the absorption of the solar cells [12-15]. It diffracts the non-absorbed propagated light

into the active layer, which is equivalent to increase the light path length. This concept in 1D grating structure has been developed in former studies [16] and proved numerically an enhancement of J_{sc}. In this section, such a pattern with dual 2D cylindrical holes structures is proposed to further increase the absorption at large wavelengths.

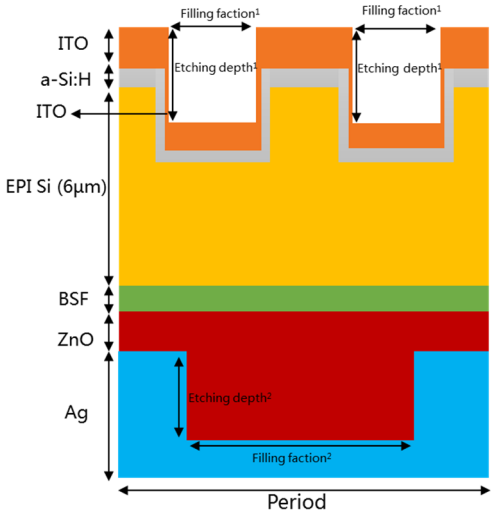

Figure 4-12. Schematic image of the dual patterns (cylindrical holes PC structure) designs in the profile view.

As shown in the schematic view of the design in Fig. 4-12, the whole solar cell stack is composed, from bottom to top, of a silver layer as the back contactor and reflector, the zinc oxide (ZnO) layer (as an optical spacer, 100 nm), the 6 μm thick c-Si active layer lying on a highly doped c-Si acting as a BSF layer (100 nm), passivated by the conformal a-Si:H layer (20 nm) and then covered by the continuous ITO layer (50nm on horizontal surfaces, and 7 nm for the sidewalls). The ZnO was used instead of ITO since it can be less absorbing. The periodic cylindrical holes structure were introduced on the top (ITO, a-Si:H and c-Si) layers and the bottom silver layer is filled with ZnO, with 4 cylindrical holes in a 2x2 supercells on the top and one single cylindrical holes on the bottom in one period. It can be noticed that as the pattern must be periodically repeated for the simulation, the period has to include integer numbers of patterns both on the top and the bottom gratings. The optimization method by tuning the geometry of the PC patterns was performed in this structure for the specific c-Si thickness of 6μm. Furthermore, we also simulated the designs with only top patterns in order to put into evidence the absorption enhancement of the dual patterned design.

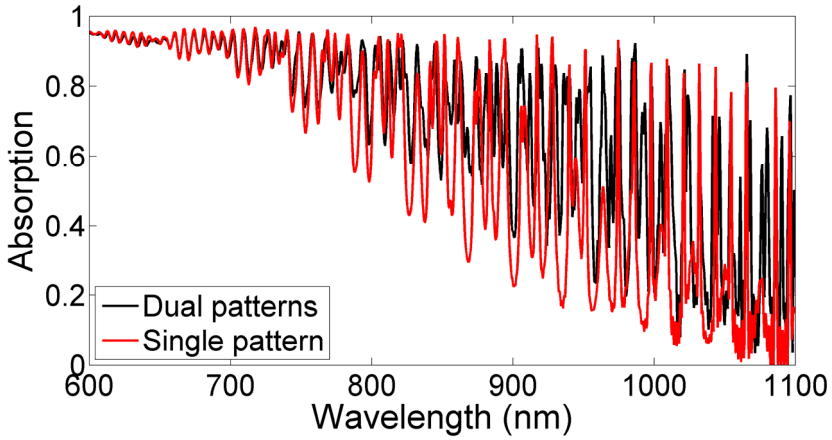

Figure 4-13. Comparison of the absorption spectra between the dual patterns and the flat design (a) or the single pattern of the front layers (b) in the wavelength range of the 600-1100nm with the 6μm thick c-Si layer stack.

For an optimized dual cylindrical holes design, the period is 680 nm, the filling fraction (*ff*) on top for each holes is 0.1 and on bottom is 0.5, and etching depth for the hole on top is 150 nm and on bottom is 200 nm respectively. The corresponding J_{sc} is 32.96mA/cm², which is 2.39mA/cm² higher than the simple single front cylindrical holes structure. Since we have already realized the patterned structure could reduce the reflection compared to the flat design in the short wavelength range, we will focus on the large wavelength in a range, i.e. 600-1100nm. Then with this supplement pattern on the rear layers, the absorption will have denser peaks and meanwhile increase the amplitude of certain peaks, as shown in Fig. 4-13.

Indeed, the absorption of the thin film solar cell might be further enhanced because of the introduced second PC patterns at the interface between the optical spacer and the back mirror, so without patterning the silicon at the back side and thus preventing from any additional surface recombination. However, this introduced pattern needs more steps during fabrication process, resulting in an additional cost. Under this situation, we need to propose a simple design applying to the thin film solar cells in order to obtain high absorption, and meanwhile keep the design more realistic.

4.6 Conclusion and perspective

In this chapter, we have proposed the two kinds of photonic crystal structures: the inverted nano-pyramids and the cylindrical holes, applied to the complete thin film solar cells on the top of the layers, including the absorbing c-Si layer, which is much closer to a realistic solar cell. By performing the numerical simulations based on FDTD method, the optimized designs were realized and then it clearly evidenced the PC structures will help the thin film solar cells to have a higher current densities (J_{sc}) with a relative increase respectively of 56.4% and 104.8% compared to the unpatterned stack. Meanwhile, from the analysis of the absorption in each layer, the inverted nano-pyramids structure has a better performance than the cylindrical holes structure, which is mainly due to a more robust anti-reflectivity property and a higher coupling light efficiency in the longer wavelength range. Additionally, we calculated the generation rate map for the electronic simulations. At last, a second cylindrical holes structure introduced on the bottom of the thin film solar cell in order to compose a dual cylindrical holes design to increase the absorption in the long wavelength range, with a current density 2.39mA/cm² higher than the front patterned cell.

All in all, the absorption of thin film solar cells with one single periodic PC structure is better than the unpatterned flat design, while it is still low in the large wavelength range. Indeed, adding a second pattern will increase the absorption but it also increases the cost at same time. So in the next chapter, we will focus on an advanced designs to further increase the absorption and maintain the cost.

References and links

1. L. Korte, E. Conrad, H. Angermann, R. Stangl, and M. Schmidt, "Advances in a-Si: H/c-Si heterojunction solar cell fabrication and characterization," Solar Energy Materials and Solar Cells **93**, 905-910 (2009).
2. K. Masuko, M. Shigematsu, T. Hashiguchi, D. Fujishima, M. Kai, N. Yoshimura, T. Yamaguchi, Y. Ichihashi, T. Mishima, and N. Matsubara, "Achievement of more than 25% conversion efficiency with crystalline silicon heterojunction solar cell," Photovoltaics, IEEE Journal of **4**, 1433-1435 (2014).
3. S. Franssila, *Introduction to microfabrication* (John Wiley & Sons, 2010).
4. E. D. Palik, *Handbook of optical constants of solids* (Academic press, 1998), Vol. 3.
5. L. Peres, V. Vigneras, and S. Fasquel, "Light trapping efficiency of organic solar cells with large period photonic crystals," Optics express **22**, A1229-A1236 (2014).
6. A. Bozzola, M. Liscidini, and L. C. Andreani, "Photonic light-trapping versus Lambertian limits in thin film silicon solar cells with 1D and 2D periodic patterns," Optics Express **20**, A224-A244 (2012).
7. J. Y. Kim, S. H. Kim, H. H. Lee, K. Lee, W. Ma, X. Gong, and A. J. Heeger, "New Architecture for High-Efficiency Polymer Photovoltaic Cells Using Solution-Based Titanium Oxide as an Optical Spacer," Advanced Materials **18**, 572-576 (2006).
8. A. K. K. Kyaw, D. H. Wang, D. Wynands, J. Zhang, T.-Q. Nguyen, G. C. Bazan, and A. J. Heeger, "Improved Light Harvesting and Improved Efficiency by Insertion of an Optical Spacer (ZnO) in Solution-Processed Small-Molecule Solar Cells," Nano Letters **13**, 3796-3801 (2013).
9. G. Gomard, E. Drouard, X. Letartre, X. Meng, A. Kaminski, A. Fave, M. Lemiti, E. Garcia-Caurel, and C. Seassal, "Two-dimensional photonic crystal for absorption enhancement in hydrogenated amorphous silicon thin film solar cells," Journal of Applied Physics **108**, 123102 (2010).
10. S. Collin, "Nanostructure arrays in free-space: optical properties and applications," Reports on Progress in Physics **77**, 126402 (2014).
11. A. Mavrokefalos, S. E. Han, S. Yerci, M. S. Branham, and G. Chen, "Efficient light trapping in inverted nanopyramid thin crystalline silicon membranes for solar cell applications," Nano letters **12**, 2792-2796 (2012).

12. L. Zeng, P. Bermel, Y. Yi, B. Alamariu, K. Broderick, J. Liu, C. Hong, X. Duan, J. Joannopoulos, and L. Kimerling, "Demonstration of enhanced absorption in thin film Si solar cells with textured photonic crystal back reflector," Applied Physics Letters **93**, 221105 (2008).
13. J. G. Mutitu, S. Shi, C. Chen, T. Creazzo, A. Barnett, C. Honsberg, and D. W. Prather, "Thin film solar cell design based on photonic crystal and diffractive grating structures," Optics Express **16**, 15238-15248 (2008).
14. Y. Shi, X. Wang, W. Liu, T. Yang, and F. Yang, "Hybrid light trapping structures in thin-film silicon solar cells," Journal of Optics **16**, 075706 (2014).
15. K. X. Wang, Z. Yu, V. Liu, Y. Cui, and S. Fan, "Absorption enhancement in ultrathin crystalline silicon solar cells with antireflection and light-trapping nanocone gratings," Nano letters **12**, 1616-1619 (2012).
16. X. Meng, E. Drouard, G. Gomard, R. Peretti, A. Fave, and C. Seassal, "Combined front and back diffraction gratings for broad band light trapping in thin film solar cell," Optics Express **20**, A560-A571 (2012).

5. Simulation and fabrication of pseudo-disordered PC structures assisted thin film solar cell

We have designed square lattice PC structures that will increase the absorption of the thin film solar cells. However, the absorption in the long wavelength range is still low. This is due to the limited spectral density of modes of the PC. Thus, we choose to use pseudo-disordered structures made of a supercell periodically repeated in a square lattice. The supercell is then a random set of cylindrical holes. Such patterns can still be simulated with the RCWA or FDTD methods as previously. For the fabrication, direct writing method such as electron beam lithography (EBL) will typically be required for a first sample or for a mask that can be replicated by a nanoimprint lithography.

A previous work in the group [1] has numerically demonstrated the interest in a 200 nm thick a-Si:H layer on glass. If this structure was easy to analyse thanks to a reduced number of guided modes, the interest for PV is very limited.

The first objective of this chapter is to check the potential of this approach in a more realistic solar cell configuration, based on bonded c-Si with a metallic layer. Then, some samples can be realized and characterized. In the next chapter, we will go deeper in the analysis and optimization of the pseudo-disordered patterns.

5.1 State of the art

As stated in the previous chapters, the light trapping strategy based on the PC structure applied to the thin film solar cells will increase the absorption compared to the unpatterned reference. [2, 3]. However, the absorption in the long wavelength range still lower than the expectation, especially for the cylindrical holes structure. This is because only a few diffraction orders could be exploited to the light trapping in the ordered structures. This approach is highly efficient only for specific wavelengths and angles as traduced by the high quality factor peaks obtained on a typical absorption spectrum, in the large wavelength range, where the absorption of the c-Si is very low.

So the advanced design should be introduced in order to enhance the absorption in the long wavelength range. As an example, the proposed complex design that combines a front and a rear PC structure [4-7] can overcomes this value by adding new optical modes and tailoring the reflection at the bottom interface of the solar cell. Still, this approach is technologically quite complex.

The mechanism of light coupling and trapping into thin film solar cells can be improved by using additional resonant modes in the long wavelength range. To achieve this, introducing a certain degree of disorder in a periodic structure has been considered during the past years. However, in most of these investigations, the performance of disordered structures [8-11], partly disordered structures [1, 12-19] or quasicrystal structures [20, 21] are compared to non-optimized ordered structure [8, 9, 11, 13, 17]. Furthermore, most of these theoretical investigations consider the sole absorbing layer [1, 8, 13, 18, 19], i.e. without a back metal layer, or nanopatterns which fabrication appears highly challenging [14, 22]

In our approach, we first considered a fully optimized and robust simply periodic PC structure, as a reference. Then, by using the parameters of the optimized PC structure, a supercell was made of randomly positioned holes periodically repeated in a square lattice in order to define a pseudo-disordered photonic crystal [1]. Such an approach allows to quantify the magnitude of disorder introduced in an optimized design and to engineer the optical resonances related to the periodic nanopattern. Meanwhile, our approach was conducted on a technologically realistic thin photovoltaic stack [23], where the thickness of the absorbing layer was chosen in order to eventually achieve a high absorption. Lastly, the nanopatterned design with carefully

positioned holes was chosen, so that the design could be implemented with a conventional lithography technique with a reduced effort compared to complex and very small patterns that have been proposed elsewhere. Finally, in order to avoid additional surface passivation issues in future development, we kept a lattice of cylindrical holes to prevent any extra sidewall or nanopatterned shape differences, and enabled to use the same conformal depositions conditions for the subsequent passivation of the nanopattern.

5.2 Thin film solar cells design and simulation methodology

In order to clearly reveal the influence of the presented pseudo-disordered structure, we focused the quite simply stack which is an absorber (c-Si) on a back contact in this chapter. More precisely, the stack under consideration is a 1μm thin c-Si film (see annex 1) bonded onto a 1μm thick aluminum (Al) layer on a glass substrate as depicted in Fig. 5-1a. The Al layer acted as a back mirror, especially at the wavelengths above 0.5μm where the single pass absorption in c-Si is low; and it could also act as a back contact in a solar cell. A PC structure was then partially etched in the c-Si film, with an etching depth in a range of 100-200 nm.

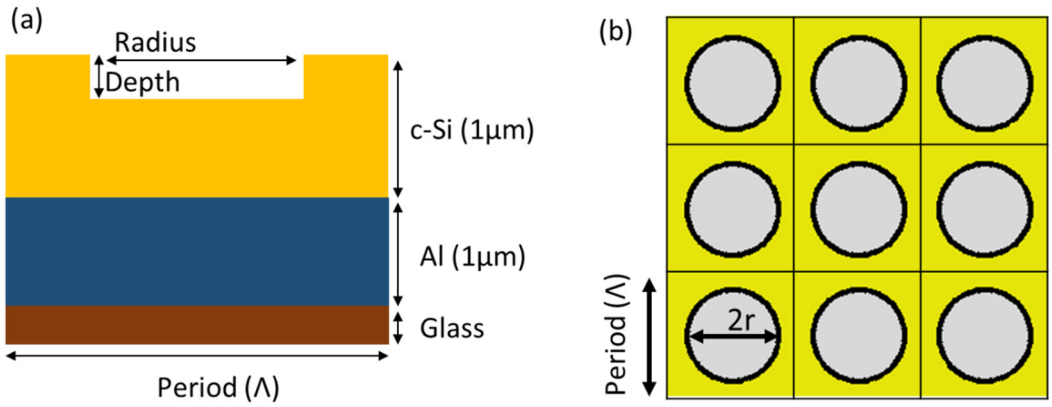

Figure 5-1. (a) A patterned thin c-Si film lies on a metallic layer bonded on a glass substrate. (b) A square lattice (period, Λ) of partially etched (etching depth, h) hole (radius, r) is used to increase the absorption of the stack.

In the photovoltaic solar cells, the increase of the absorption should be the net enhancement in the active layers, but it is not easy to be detected in the experimental characterization process. Under this condition, a trade-off by using the result of the

reflection or total absorption of the thin film solar cells will be taken into account. We used the rigorous coupled wave analysis (RCWA) method to implement the numerical simulations, the material optical indices used are presented in appendix. Unpolarized AM1.5 light at normal incidence was used to mimic the solar illumination in the 300-1100nm range.

5.3 Optimization of the square lattice of holes PC structure

Before we introduced the pseudo-disordered structure in the thin film solar cells, we firstly performed the optimization on the simply periodic structure with the square lattice of holes as the reference. The 2D square lattice of air hole depicted in Fig. 5-1a and 5-1b is fully determined by three different parameters: the period (Λ), the air-surface filling fraction (*ff*) (ratio between the area of the air hole and the total area, given by $ff=\pi r^2/\Lambda^2$, r being the radius of the cylindrical hole) and the etching depth (h).

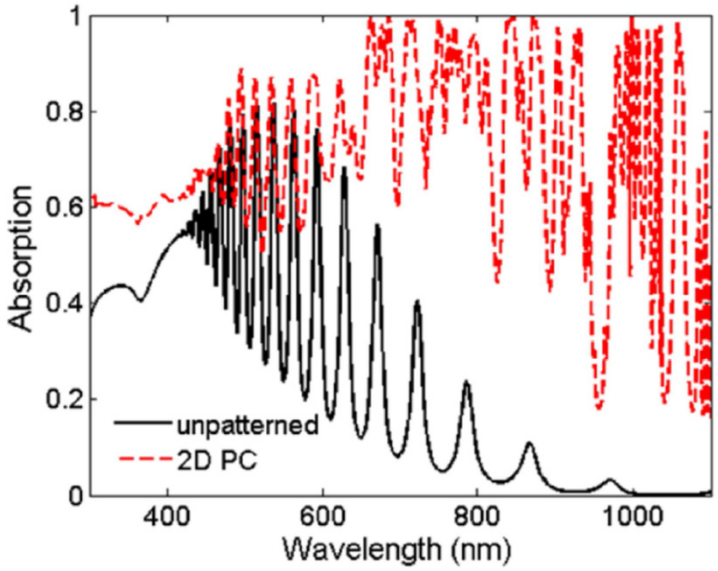

Figure 5-2. Comparison of the total absorption between the unpatterned thin film (black curve) and the absorption of the optimized square lattice of holes PC structure (red dashed line) with the 1μm thick c-Si layers.

By tuning the parameters, i.e. period, *ff* and the etching depth, with the same optimization methodology as in the previous chapter, the optimized parameter was with period of 657nm, a *ff* of 0.42 and an etching depth of 213.5nm. These values are in good agreement with results obtained on a quite similar stack [14], but slightly different from

our optimal values in the previous chapter due to the lack of top layers. The optimized absorption spectrum is then plotted in Fig. 5-2 and compared to the absorption spectrum for the unpatterned case. The square lattice of holes PC structure is highly efficient for specific wavelengths and angles due to the periodicity; this corresponds to the shark peaks displayed in Fig. 5-2 compared to the unpatterned case. Thanks to the PC structure, the integrated absorption is enhanced from 37.7% (the unpatterned case) to 70.7% (optimized square lattice of holes PC structure), which the corresponding relative enhancement in a value of 87.8%.

5.4 Advanced design: pseudo-disordered lattices of cylindrical holes, assist the thin film solar cells

In order to further overcome these limitations and then increase the absorption of thin-film solar cells, we propose to change the pure periodic structure into the pseudo-disordered case, relying on a careful shift of the holes position. Based on the parameters of the optimized square lattice of holes structure, we moved the hole shown in Fig. 5-3a by a distance of shift (*dp*) under an angle of α. The value of *dp* is determined by a Gaussian distribution, while the angle is determined by a uniform distribution. Then this perturbation process was applied to 9 holes (Fig. 5-3b) composing a 3x3 supercell further replicated in a square lattice. To avoid numerical issues and to keep a realistic design, only the cases in which holes do not merge were considered. For each selected value of mean shift (mean *dp*), we simulated 10 different structures. As we selected 5 different values for the mean shift from 25nm to 75nm, we computed the integrated absorption for 50 different structures, which correspond to different realizations of the disorder.

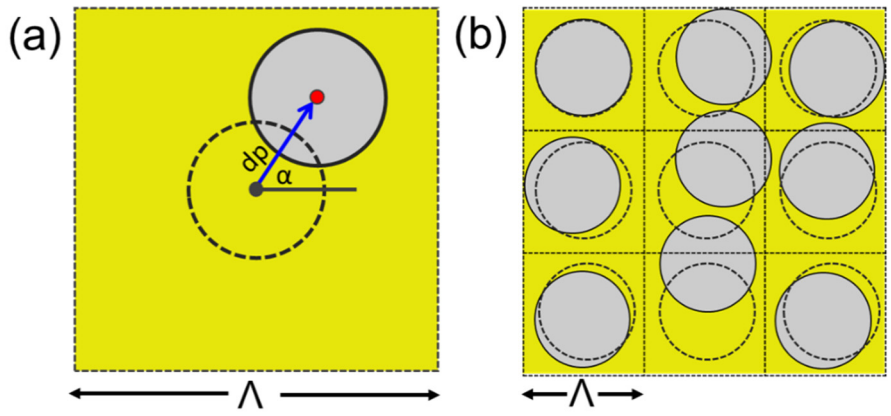

Figure 5.3. Schematic view of the perturbation (a) for a single hole and (b) for 9 holes in a 3x3 supercell structure.

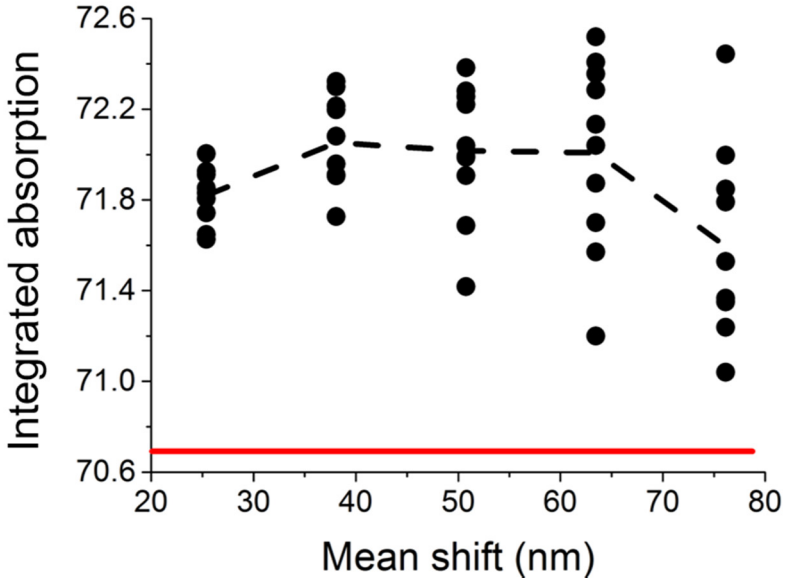

*Figure 5-4. Evolution of the theoretical integrated absorption for 10*5 pseudo-disordered structures (dark dot). The mean value of integrated absorption (black dashed line) remains higher than the optimized square lattice of holes structure as the reference value (red horizontal line).*

As shown in Fig. 5-4, the integrated absorption of the pseudo-disordered structures are above the optimized square lattice of holes, indicating the pseudo-disordered structure absorbs more light. Then let us firstly focus on the evolution of the averaged integrated absorption (black dashed line in Fig. 5-4). When the value of mean shift increases from 25 to 38 nm, the averaged integrated absorption increases from 71.8%

to 72.0%. Then, this figure-of-merit remains quite constant for mean shift values from 38 to 63 nm. If the mean shift value is larger than 63 nm, the mean integrated absorption decreases down to 71.5%. This evolution of the mean integrated absorption is related to the range of integrated absorption that can be obtained as depicted by the black dots. When the value of d increases from 25 to 75 nm, the range of available integrated absorption extends from 71.0% to 72.5%. As the reference structure in this study is an optimized square lattice of holes, the amount of disorder introduced in the lattice should be carefully chosen. Designs including highly perturbed patterns could lead to a decrease of the integrated absorption compared to a slightly pseudo-disordered structure. Indeed, the gain at large wavelengths can be lost by a poor absorption at low wavelengths, due to a far lower diffraction efficiency than using the square lattice of holes.

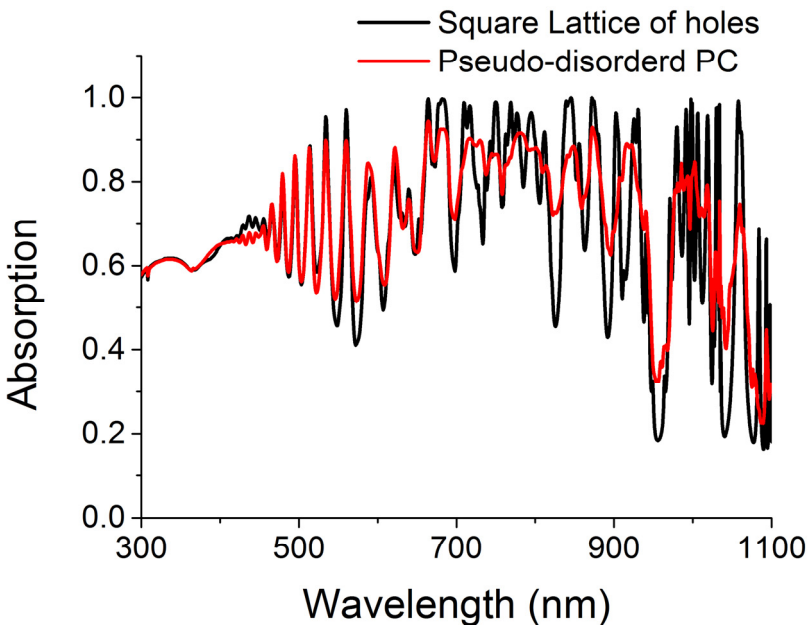

Figure 5-5. Comparison between the theoretical absorption of optimized square lattice of holes structure (black curve) and the theoretical absorption of the best pseudo-disordered structure (red dashed line).

Among these obtained results in pseudo-disordered structure, the best of them that is corresponding to an optimized design will be compared to the optimized simply periodic structure, and discussed. The absorption spectra corresponding to these two structures are plotted in Fig. 5-5. For this selected structure, the expected integrated absorption is as high as 72.5%, which corresponds to an absolute increase of 1.8% (and

a relative enhancement of 2.6%) compared to the previously optimized square lattice of holes. Then we divide the spectrum in two parts, with a 700nm boundary. Below 700nm, the absorption spectra in the optimized square lattice of holes and the best pseudo-disordered structure exhibit almost similar performance, they have the same number of the peaks and only smaller offset exist in the corresponding peaks, but the integrated absorption is kept same (only 0.7% relative higher in the pseudo-disordered case). Above 700nm, even if the pseudo-disordered structure appears to have less absorption peaks than the optimized square lattice of hole, this structure exhibits more modes thanks to the introduced perturbation, as expected since the period of the supercell is larger than the one of the square lattice of holes. As the amplitude of these peaks is small, the result is a broadening of the peaks and then the number of visible peaks decreases. However, as it has been shown in a previous work [1], such a broadening can be benefic for the integrated absorption. Finally, the integrated absorption in the pseudo-disordered structure is 4.7% larger than the one of square lattice of holes, and the effect of the disorder is mainly focused in the long wavelength range.

5.5 Fabrication process and measurements methodologies

In this section, we focus on the realization and characterization of square lattice of holes structure and the pseudo-disordered structure. As all these patterned structures are defined at the nano-metric scale (in size as well as in position of the holes), the lithography technique requires a high resolution and a large flexibility. So we resort to Electron Beam Lithography (EBL) [24, 25] and Reactive ion etching (RIE) to realize our optimized square lattice of holes PC structure and the best pseudo-disordered PC structure design in the 1μm thick c-Si layer stack [1, 10, 12, 17]. After the structures are patterned on the stack, the characterization will be performed on their topography and the optical property.

5.5.1 Si stack and nanolithography

The 1μm thick mono-crystalline silicon layer stack fabricated by epi-free was chosen for the thin film solar cells. The c-Si was bonded with a 1μm thick aluminum layer on glass and 200nm thick SiO_2 as the hard mask layer.

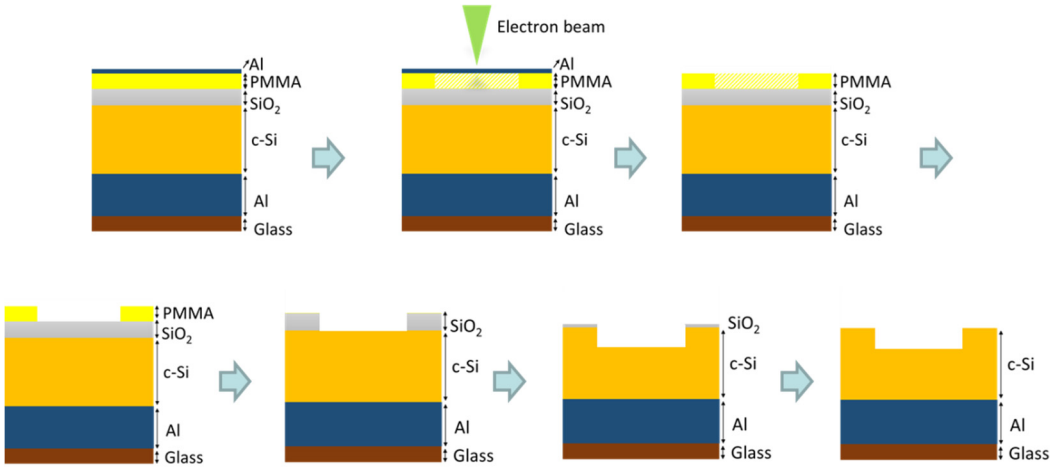

Figure 5-6. Simplified process flow for the patterning of a c-Si stack by the electron beam lithography (EBL), the development and Reactive ion etching (RIE).

In the EBL process (Fig. 5-6), the shape and size of pattern depend on the several key parameters: electron beam size, electron dose, dwell time, the accelerate voltage and the properties of the sample, including the type of the photoresist. Based on the result of the adjustment, we tune the electron dose to get different holes radii but keep the other setting in an appropriate value. An accelerating voltage of 30kV and working distance of 6mm was always used. The beam current (~10pA) was measured with a Faraday cup to maintain a constant dose during the beam write. A magnification of 1100×, corresponding to a calibrated field of view of 100μm on a side, was predominantly used. A proper selection of the electron beam resist is very crucial to obtain the resolution inherent to the e-beam lithography system. A 100nm thick PMMA A4 electron sensitive resist was deposited on the sample by spin coating and then baked at 180°C during 1min 30s on a hot plate. Then, in order to have better adjustment during the EBL operation, a 10nm thick Al is deposited on the top of the sample to reduce charging effects.

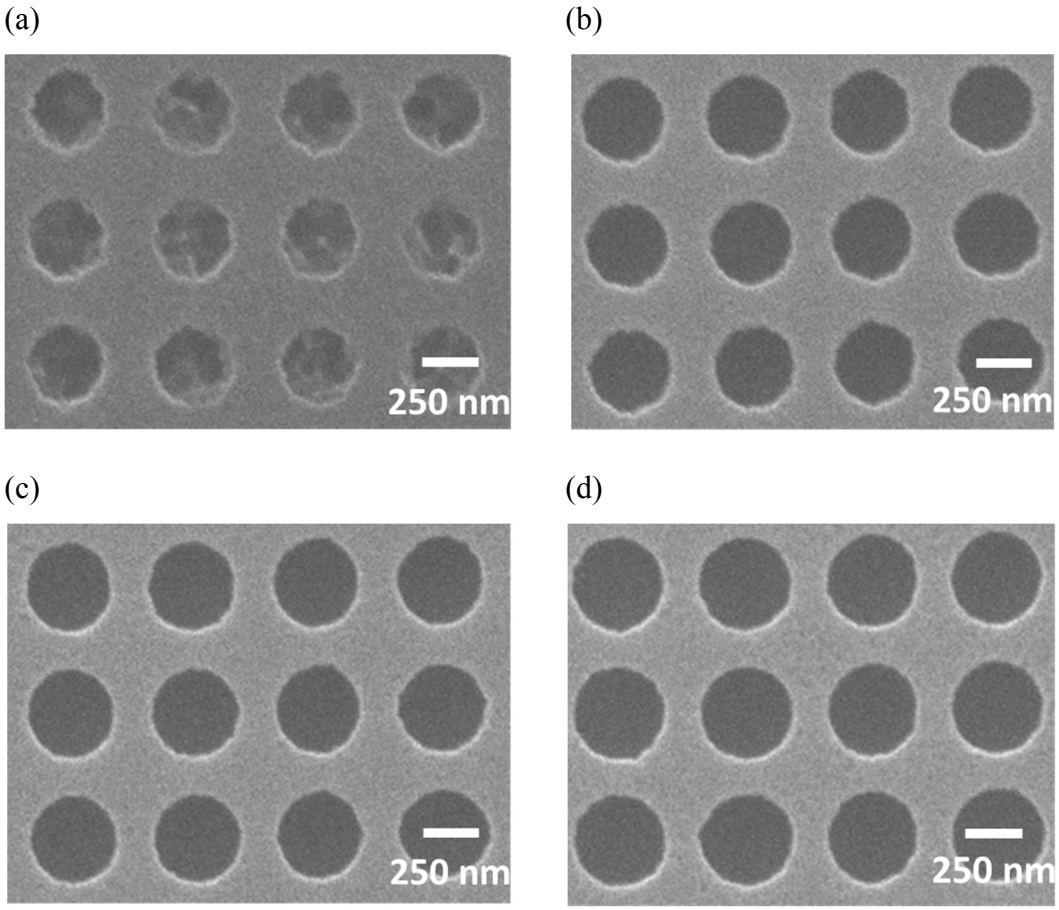

Figure 5-7. Influence of the exposure dose on the radius of the holes, which the expose dose factor is 0.9 (a), 1.1 (b), 1.3 (c), and 1.6 (d) respectively.

As shown in Fig. 5-7, the different holes radii could be obtained by tuning the dose factor. With the low dose factor (Fig. 5-7a), it means that the dose of the electron exposure is not enough to make expected holes. So with a standard recipe of the plasma etching process, due to the smaller size, the holes not well etched and the boundaries is quite rough. When the dose factor increases (Fig. 5-7b, c and d), the size of the holes are larger and the boundaries are smoother. Based on a series of test on the changing dose factor, we chose the value of 1.35 to obtain the expected size of the hole, leading to a 135μC/cm² dose.

In order to reduce the error between the experimental result and numerical result, the size of the patterned area was limited in order to make sure all the structures fabricated in a single run process. The sample was then developed in the solution of Aluminum Etchant Type D during 2min 30s, to remove the Al layer. Then the exposed area could be removed by the developer MIBK/IPA 1:1, during 45s at a room

temperature, and the sample is then rinsed in isopropyl alcohol ($(CH_3)_2CHOH$). Lastly, the sample is dried and baked at 100°C on a hot plate for 1 min.

5.5.2 Reactive ion etching (RIE) process

Next step is transferring PMMA patterns into the underlying c-Si layer. We use reactive ion etching (RIE) [26] and more specifically the recipe shown in Table. 3-1, in Chapter 3. The patterns are first transferred into a 100nm thick, SiO_2 hard mask, and then to the c-Si layer. The Si patterns obtained are shown in Fig. 5-8.

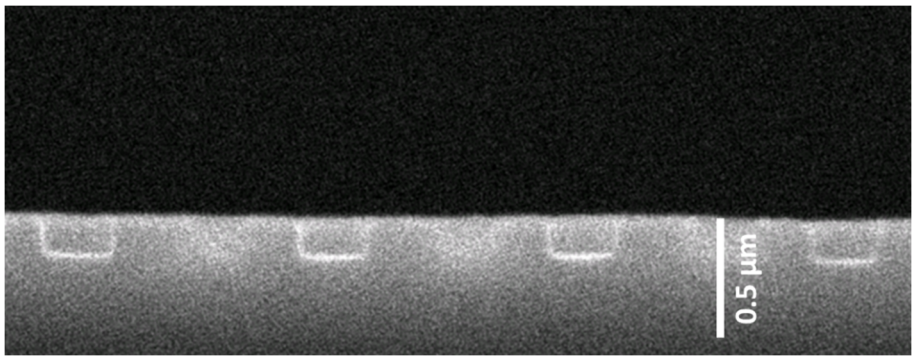

Figure 5-8. SEM cross section view of the patterned c-Si layer with a 1D structure.

5.5.3 Characterization of the patterned structures

Optical measurements should be performed both on patterned and non-patterned area. Due to the limitation in the area of the patterned structures, only micro-reflectivity could be performed. Because an Al layer underlies the c-Si layer, so the absorption of the solar cells could be approximate to 1-Reflection.

5.6 Silicon-on-Insulator-based nanopatterned absorber

Before we perform the fabrication on the stack of the c-Si layer on aluminum, we consider the patterns on a Silicon-on-Insulator (SOI) wafer. The geometrical parameters of the stack are shown in Fig. 5-9, which is a 0.7µm thick c-Si layer on a 1µm thick SiO_2 layer, on top of the c-Si substrate. With this stack, we will focus on the

patterned absorbing c-Si layer without the parasitic absorption in the back metal. Meanwhile, such a SOI wafer exhibits a better surface with a roughness lower than 1nm in rms. This outstanding topography allows the realization of patterns that are very close to the designed PC structure.

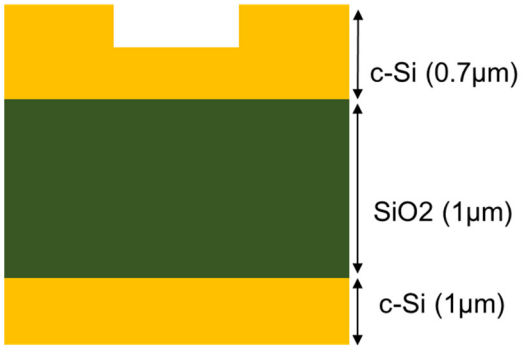

Figure 5-9. Schematic view of the pattened structure on the Silicon-on-Insulator (SOI) wafer.

As we will use this kind of structures as model structures, we chose to perform the realization of two optimized structures based on the previous optimization on the metal-based stack: the pseudo-disordered structure that exhibits the highest absorption and the square lattice of holes that will be used as a reference (Fig. 5-9). Lastly, we choose to limit the size of the patterned area to 300x300µm², which is a trade-off between the time needed to realize the structure and the mismatch between optical simulation and characterization.

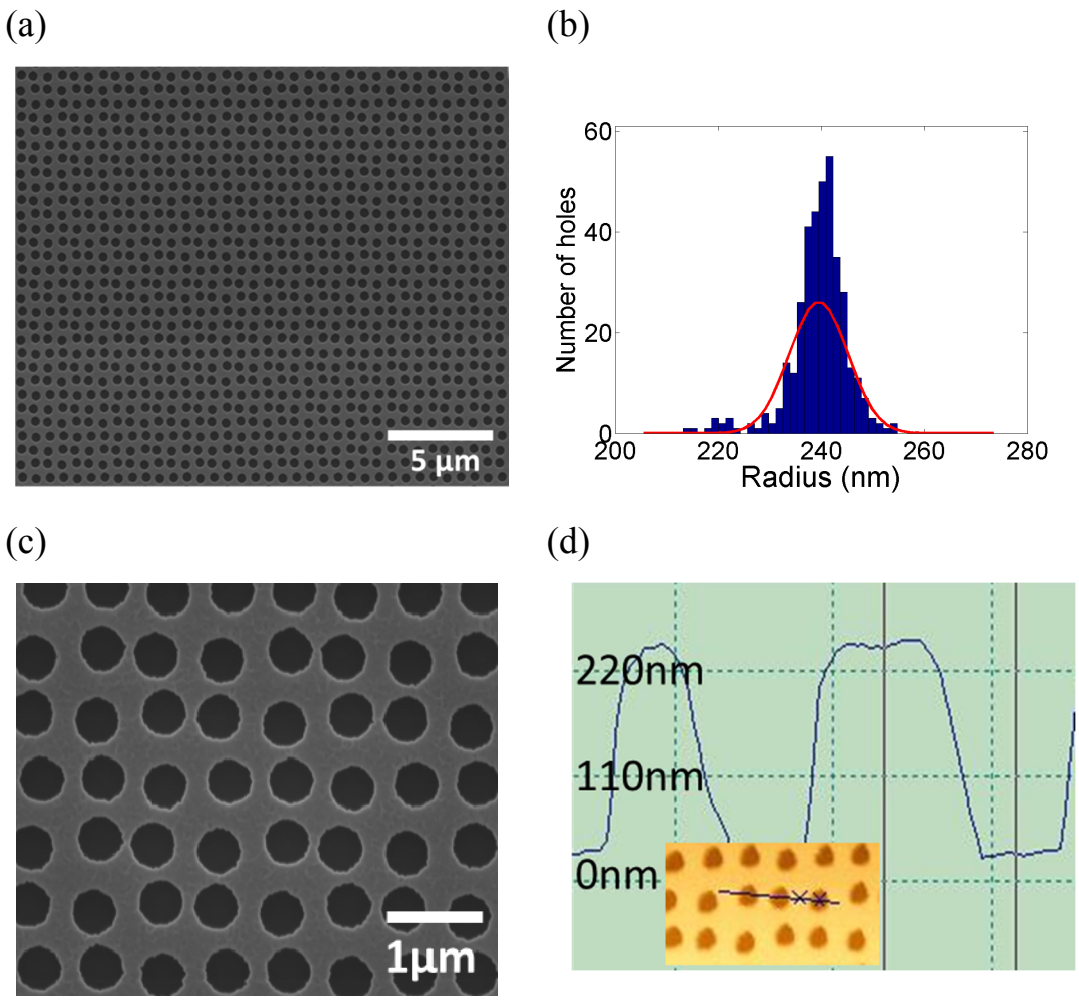

Figure 5-10. SEM image (a, c) of the pseudo-disordered structure in SOI sample and the corresponding distribution of the radius (b) of holes. The depth of hole measured by the AFM characterization (d).

From the SEM images (Fig. 5-10a&c), we could evaluate the distribution of the holes radii (Fig. 5-10b) in the fabricated structures, with a mean radius of about 239 nm and a deviation of 5 nm. It means the averaged *ff* is 0.42 in the fabricated structures in the SOI sample. Meanwhile, according to the result of the AFM measurement (Fig. 5-10d), the depth of the holes is about 210nm which is in a good agreement with the simulated case. Also due to the changing of the stack for the metal-based to the SOI, we launched the new simulation based on the parameters of the SOI wafer.

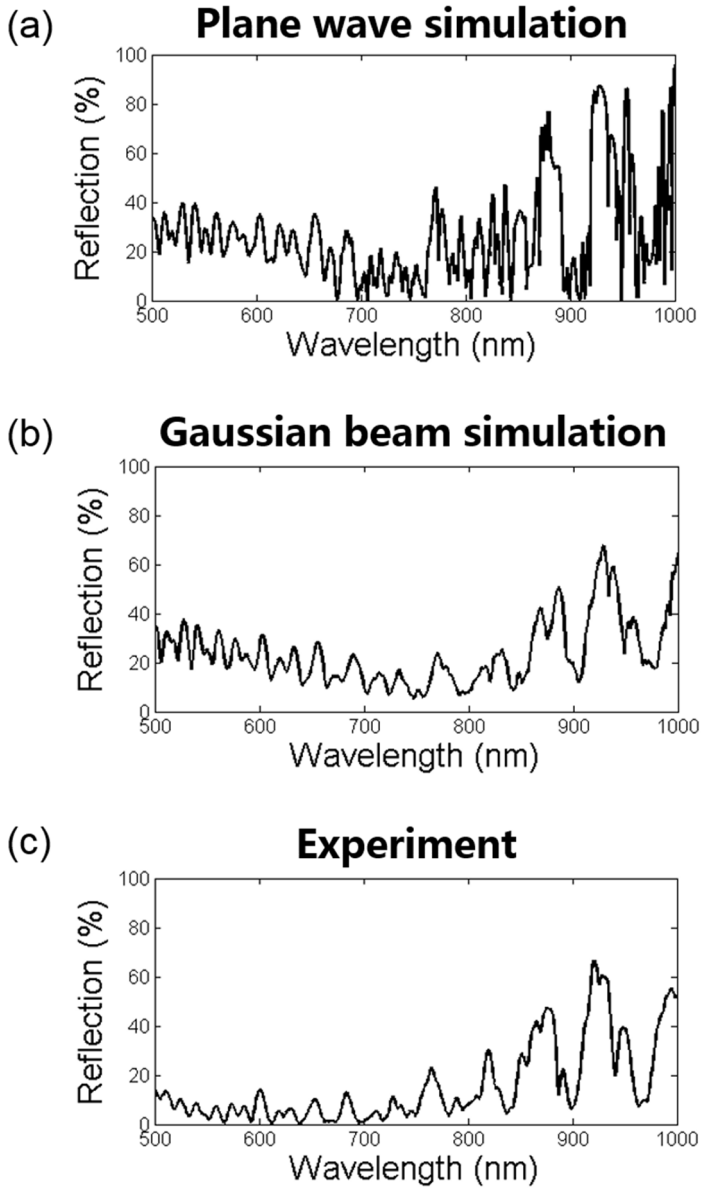

Figure 5.11. In the square lattice of holes structure with the SOI stack, the theoretical reflection spectrum under normal incidence with plane wave (a), with Gaussian beam (b) and the experimental reflection spectrum (c).

Under a plane wave normal incidence, the theoretical and the corresponding experimental reflection spectrum of the square lattice of holes structure are shown in Fig. 5-11a and Fig. 5-11c respectively. In the wavelength range of 800-1000nm, 1000nm corresponding to the longest achievable wavelength in our set-up, sharp and dense peaks appear in the result of the numerical simulation, while they are absent in the experimental spectrum. Conversely, the broad absorption peaks are shown in the measured spectrum. In the range of 500-800nm, the reflection in the experiment is

lower than the theoretical case. In order to achieve a better correspondence between the theoretical and experimental results, we should take into account the profile of the incident light. Indeed, in experimental process, the structures are not illuminated by a plane wave, but by a Gaussian beam profile. Thanks to the 300x300μm² size of the structure, small magnification objectives (x5) can be used with a corresponding reduced numerical aperture of 0.14. In order to achieve a good agreement between experiment and simulation with the square lattice of holes structure, the usual theoretical reflection spectrum (obtained for a plane wave under incidence) is replaced by the reflection spectrum obtained for a Gaussian beam under normal incidence mimics the experimental incident light, which the Gaussian beam is a summation of plane waves under different angles and has a waist of 60 μm. Such a substitution increases the computational time by a factor directly proportional to the number of plane waves used in the summation. Thus, such simulations can be performed within a reasonable time only for the square lattice of holes.

Let us now compare the theoretical spectrum obtained with the Gaussian beam simulation (Fig. 5-11b) with the experimental spectrum (Fig. 5-11c). In the range of 800-1000nm, the number of peaks, the quality factor and their contrast are in much better agreement. However, in the range below 800nm, while the peak positions match well, their maxima somehow disagree. This difference is probably mainly due to the small roughness (<<1nm in rms) of the remaining SiO_2 layer. With the micro-reflectivity set-up, the roughness will increase the amount of leaky reflected light in the measurement, resulting in an unexpected low measured reflection. Moreover, due to the limitation of this micro-reflectivity set-up, the large orders of the reflected light could not be captured by the detector, which is diffracted into the air. That could cause a low reflection in the experimental measurement compared to the result of numerical simulations.

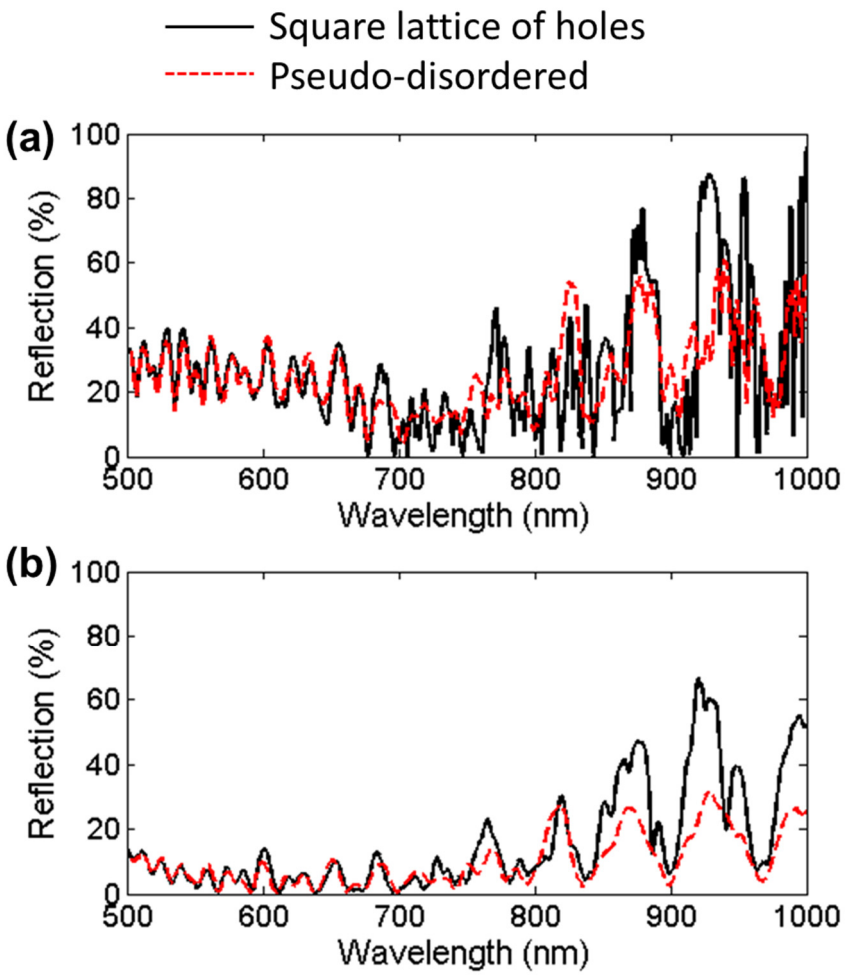

Figure 5-12 Comparison between theoretical reflection (a) and experimental reflection (b) spectra obtained for the square lattice of holes (dark line) and for the pseudo-disordered structure (red dash line).

In order to study the effect of the pseudo-disordered structure, we limit the simulation to the case of a plane wave at normal incidence to compute the absorption of our thin layer with or without disorder, as depicted in Fig. 5-3b. In this theoretical result (Fig. 5-12a), the pseudo-disordered structure behaves almost same way as the square lattice of holes structure in the wavelength range below 700nm, the same remark can be made for experiment result (Fig. 5-12b). According to this agreement in both the square lattice of holes and the pseudo-disordered structure, we can conclude that the designed pseudo-disorder has no effect on the absorption for these wavelengths. As analyzed in the previous paragraph, the experimental results have a lower reflection compared to the simulation cases; we can conclude that the designed pseudo-disorder has less influence than the remaining slight roughness in the SiO_2 layer and

imperfection in the holes circularity. While the latter leads to a better impedance matching with the air, the former tends to induce an additional disorder that broadens the peaks on the reflection spectrum.

In the 700-1000nm wavelength range, the sharp peaks of the square lattice of holes are broadened in the pseudo-disordered structure on the theoretical spectrum (Fig. 5-12a). The expected sharp peaks in the pseudo-disordered case are related to the limited diffraction efficiency of the incident plane wave into the added orders, even if their intensity can be small. However, as the experimental incident light is a Gaussian beam, the coherence of this light is lower than the coherence of the theoretical plane wave. Thus, these sharp peaks are not visible on the experimental spectra shown in Fig. 5-12b. For the wavelengths between 700-1000nm, the experimental reflection (Fig. 5-12b) of the pseudo-disordered structure is almost always lower than for the square lattice of holes. Finally, a broadening of the absorption peak is visible near 875nm and 925nm on the experimental absorption spectrum, in the case of the pseudo-disordered structure. Thus the pseudo-disordered structure exhibits a significantly higher absorption than the square lattice of holes as expected theoretically.

From these results related to the two different designs both in experiments and the simulation, the introduced pseudo-disordered structures do not change the reflection in the short wavelengths. The lower reflection in the experimental spectrum in the short wavelength is mainly due to experimental fluctuations on the surface roughness and the circularity of holes. In the long wavelength range, the discrepancies between the illumination condition in the numerical and experimental cases (mainly Gaussian beam vs plane wave), and also considering the remaining roughness and non-uniformities of the pattern in the fabricated structures, the reflection spectra exhibit broad peaks which could artificially increase the measured integrated absorption. Still, introducing a pseudo-disorder in a simply periodic PC does lead to a reflection decrease in the long wavelength range.

Taking into account all these remarks, we will now consider the impact of the pseudo-disorder on a thin c-Si layer bonded onto a metal layer standing on a glass substrate.

5.7 Crystalline-Si-Aluminum-based nanopatterned absorber

In this section, we will consider the 1µm thick c-Si layer bonded on the Aluminum metal layer stack as depicted in Fig. 5-1a. Using the same experimental process as performed the previous on the SOI stack, we could to obtain the patterned stack as designed in the numerical simulations. Due to large group of the structures that are fabricated by the EBL, the size of the structure is reduced to 100x100µm², also in order to complete all the structures in a single run of EBL to limit the discrepancies and experimental fluctuations.

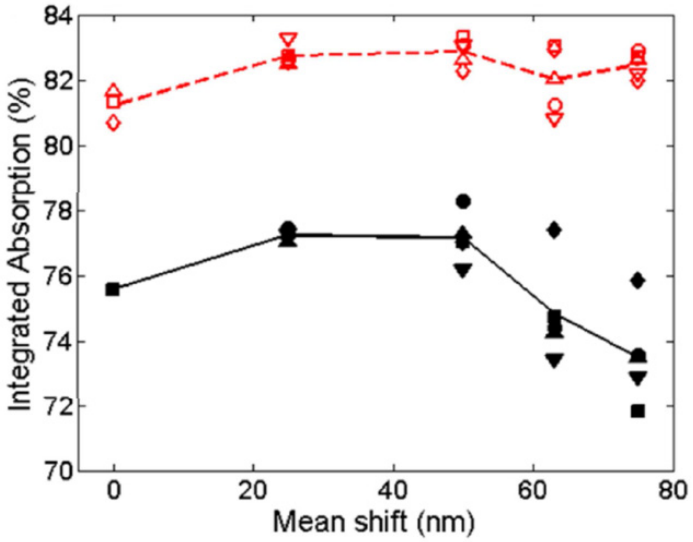

Figure 5-13. Evolution of the mean integrated absorption experimentally (red dash line) and theoretically (black line). The filled symbols (unfilled symbols) correspond to measurement (simulation) of integrated absorption for different pseudo-disordered structure. The reference value for the square lattice of holes corresponds to a mean shift value of 0nm.

Then we take into account the solar spectrum to mimic the real situation and focus on the integrated absorption in wavelength range of 700-1000nm.The results of the theoretical integrated absorption and experimental integrated absorption are plotted in the Fig. 5-13.

At the beginning, we focus on the reference structure: square lattice of holes, the experimental integrated absorption (81.2%) is higher than the theoretical result (75.6%). It can be notice that 3 different experimental results are presented for the square lattice

of holes structure, and this spread of the values is related to geometrical imperfections; while all of them are below the value which can be achieved for pseudo-disordered cases.

Next step, we will switch to the pseudo-disordered structures. Due to the fluctuations on the surface of the sample and the imperfect uniformity of the holes, we chose the relative good surface morphology of 5 pseudo-disordered structures among 10 designs in each mean shift value in the experimental case. Then the integrated absorption of the experimental and the corresponding theoretical pseudo-disordered structures are marked with different symbols and colors, as plotted in Fig. 5-13. All the experimental results overpass the theoretical results. We then compute the mean value of integrated absorption for the theoretical and experimental pseudo-disordered structures; the two curves exhibit almost the same behavior. First, both the experimental and theoretical absorption increase with the small increase of the mean shift value. Then if the mean shift value is further increased, the mean absorption does not increase anymore. The main difference between the 2 curves appears in the case of the highest mean shift value, which clearly decreases only in the theoretical case. Meanwhile, as the mean shift value increases, the available range for the integrated absorption increases experimentally as well as theoretically for the highest experimental mean shift. Even if the average value of the measured optical absorption is 5.7% higher than the simulated one, the maximal enhancements of the averaged value due to the pseudo-disorder are quite comparable in the experiments and simulation (around 1.7% in absolute value). For the best pseudo-disordered structure, the experimental integrated absorption increases by 2.1% compared to the square lattice of holes which a little bit less than the theoretical increases of 2.7%.

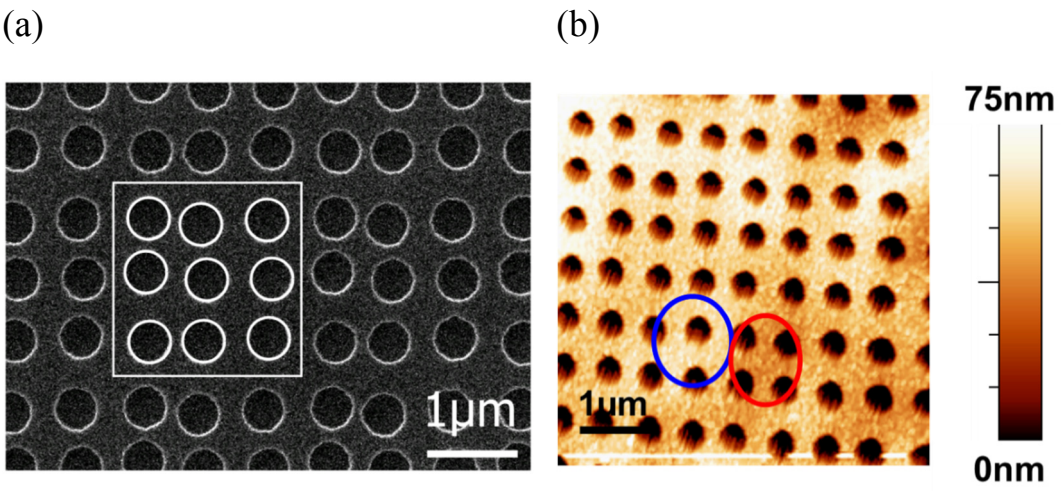

Figure 5-14. The SEM (a) and AFM (b) view of the patterned structure on the c-Si layer on metal-based wafer. The peak-to-valley highlighted by circle spots (blue and red circle) exhibit a topographical difference that is more than 10nm.

Considering the difference between the theoretical and experimental results, the offset of the integrated absorption (+5.7%) can be explained by the quality and the area of the patterns. Firstly, it can be noticed that a small roughness is exhibited on the circular shape of holes in the SEM view (Fig. 5-14a). Meanwhile, with the Atomic Force Microscope (AFM) measurement (Fig. 5-14b), we can clearly see that the roughness of the thin c-Si film on metal is significantly higher than on previous SOI wafer. For instance, the peak-to-valley highlighted by circle spots exhibit a topographical difference that is more than 10nm. Moreover, as the size of the patterned area decreases from 300x300µm² to 100x100µm², we used a higher magnification microscope objective to detect the reflection. It could lead to an increased discrepancy between the experimental and the theoretical illumination conditions.

5.8 Conclusion and perspective

Using RCWA simulation, we introduced a solar cell design based on a 1µm thick c-Si layer standing on an Al layer, patterned as an optimized photonic crystal including a controlled disorder. This, as expected, led to an almost two-fold increase of the optical absorption, over a broad and relevant wavelength range. The integrated absorption enhancement overpasses that expected using a fully optimized square lattice photonic crystal pattern, while its fabrication can be achieved using exactly the same process. In

order to further demonstrate the interest of these complex nanophotonic patterns, experiments were performed on simply periodic and pseudo-disordered nanopatterns. Model structures were first patterned in a Silicon-On-Insulator wafer, in order to highlight the influence of experimental fluctuations related to the process imperfections, and the impact of the illumination conditions on the expected absorption spectra. Technological imperfections mainly increase the optical absorption in the active c-Si layer at the shortest wavelengths of the solar spectrum. Then selected pseudo-disordered patterns have been patterned in a thin c-Si film bonded on top of the metal layer. The experimental integrated absorption measured in this solar cell stack almost exhibits the same behavior as the theoretical one, despite a constant offset. Compared to a simply periodic photonic crystal, the best pseudo-disordered structure enhanced the optical absorption up to 2.1%, which is in good agreement with the 2.7% increase expected theoretically.

The optical study involved in this work will be further extended to the case of a fully functional solar cell, enabling electro-optical characterization. As the considered stack in this work is closed to a realistic c-Si solar cell stack, the design modification will be limited. The remaining challenge stands in the fabrication of nanopatterns over square centimeters using the replication of a large master stamp fabricated by EBL and RIE.

References and links

1. R. Peretti, G. Gomard, L. Lalouat, C. Seassal, and E. Drouard, "Absorption control in pseudodisordered photonic-crystal thin films," Physical Review A **88**, 053835 (2013).
2. G. Gomard, R. Peretti, E. Drouard, X. Meng, and C. Seassal, "Photonic crystals and optical mode engineering for thin film photovoltaics," Optics Express **21**, A515-A527 (2013).
3. X. Meng, V. Depauw, G. Gomard, O. El Daif, C. Trompoukis, E. Drouard, C. Jamois, A. Fave, F. Dross, I. Gordon, and C. Seassal, "Design, fabrication and optical characterization of photonic crystal assisted thin film monocrystalline-silicon solar cells," Optics Express **20**, A465-A475 (2012).
4. X. Meng, E. Drouard, G. Gomard, R. Peretti, A. Fave, and C. Seassal, "Combined front and back diffraction gratings for broad band light trapping in thin film solar cell," Optics Express **20**, A560-A571 (2012).
5. Z. Xia, Y. Wu, H. Jiao, H. Cao, Z. Liang, J. Zhou, and X. Qin, "Thin film silicon solar cells with non-simple integral period ratio between front and back gratings," Journal of Optics **16**, 105011 (2014).
6. Y. Shi, X. Wang, W. Liu, T. Yang, and F. Yang, "Light-absorption enhancement in thin-film silicon solar cells with front grating and rear-located nanoparticle grating," physica status solidi (a) **212**, 312-316 (2015).
7. F. Gao, H. Wang, Y. Gao, Y. Wu, S. F. Liu, S. Zhou, F. Li, X. Zheng, H. Wu, and T. Liu, "Lateral matching of periodic front and back textures in thin film silicon solar cells," Optics Communications **357**, 28-33 (2015).
8. K. Vynck, M. Burresi, F. Riboli, and D. S. Wiersma, "Photon management in two-dimensional disordered media," Nat Mater **11**, 1017-1022 (2012).
9. F. Pratesi, M. Burresi, F. Riboli, K. Vynck, and D. S. Wiersma, "Disordered photonic structures for light harvesting in solar cells," Optics Express **21**, A460-A468 (2013).
10. M. Burresi, F. Pratesi, K. Vynck, M. Prasciolu, M. Tormen, and D. S. Wiersma, "Two-dimensional disorder for broadband, omnidirectional and polarization-insensitive absorption," Optics Express **21**, A268-A275 (2013).
11. U. W. Paetzold, M. Smeets, M. Meier, K. Bittkau, T. Merdzhanova, V. Smirnov, D. Michaelis, C. Waechter, R. Carius, and U. Rau, "Disorder improves

nanophotonic light trapping in thin-film solar cells," Applied Physics Letters **104**, 131102 (2014).

12. A. Oskooi, P. A. Favuzzi, Y. Tanaka, H. Shigeta, Y. Kawakami, and S. Noda, "Partially disordered photonic-crystal thin films for enhanced and robust photovoltaics," Applied Physics Letters **100**, 181110 (2012).
13. C. Lin, L. J. Martínez, and M. L. Povinelli, "Experimental broadband absorption enhancement in silicon nanohole structures with optimized complex unit cells," Optics Express **21**, A872-A882 (2013).
14. E. R. Martins, J. Li, Y. Liu, V. Depauw, Z. Chen, J. Zhou, and T. F. Krauss, "Deterministic quasi-random nanostructures for photon control," Nat Commun **4**(2013).
15. G. M. Conley, M. Burresi, F. Pratesi, K. Vynck, and D. S. Wiersma, "Light Transport and Localization in Two-Dimensional Correlated Disorder," Physical Review Letters **112**, 143901 (2014).
16. A. Oskooi, Y. Tanaka, and S. Noda, "Tandem photonic-crystal thin films surpassing Lambertian light-trapping limit over broad bandwidth and angular range," Applied Physics Letters **104**, 091121 (2014).
17. A. Oskooi, M. De Zoysa, K. Ishizaki, and S. Noda, "Experimental Demonstration of Quasi-resonant Absorption in Silicon Thin Films for Enhanced Solar Light Trapping," ACS Photonics **1**, 304-309 (2014).
18. X. Fang, M. Lou, H. Bao, and C. Y. Zhao, "Thin films with disordered nanohole patterns for solar radiation absorbers," Journal of Quantitative Spectroscopy and Radiative Transfer (2015).
19. H. Ren, Q. Du, F. Ren, and C. Png, "Photonic quasicrystal nanopatterned silicon thin film for photovoltaic applications," Journal of Optics **17**, 035901 (2015).
20. P. A. Postigo and J. M. Llorens, "Optical absorption enhancement by photonic quasicrystals in thin films for photovoltaic applications," in *Transparent Optical Networks (ICTON), 2013 15th International Conference on*, 2013), 1-4.
21. J. Xavier, J. Probst, F. Back, P. Wyss, D. Eisenhauer, B. Löchel, E. Rudigier-Voigt, and C. Becker, "Quasicrystalline-structured light harvesting nanophotonic silicon films on nanoimprinted glass for ultra-thin photovoltaics," Optical Materials Express **4**, 2290-2299 (2014).
22. M. C. van Lare and A. Polman, "Optimized Scattering Power Spectral Density of Photovoltaic Light-Trapping Patterns," ACS Photonics **2**, 822-831 (2015).

23. V. Depauw, X. Meng, O. El Daif, G. Gomard, L. Lalouat, E. Drouard, C. Trompoukis, A. Fave, C. Seassal, and I. Gordon, "Micrometer-thin crystalline-silicon solar cells integrating numerically optimized 2-D photonic crystals," Photovoltaics, IEEE Journal of **4**, 215-223 (2014).
24. M. Qi, E. Lidorikis, P. T. Rakich, S. G. Johnson, J. Joannopoulos, E. P. Ippen, and H. I. Smith, "A three-dimensional optical photonic crystal with designed point defects," Nature **429**, 538-542 (2004).
25. G. Subramania and S. Lin, "Fabrication of three-dimensional photonic crystal with alignment based on electron beam lithography," Applied physics letters **85**, 5037-5039 (2004).
26. X. Meng, G. Gomard, O. El Daif, E. Drouard, R. Orobtchouk, A. Kaminski, A. Fave, M. Lemiti, A. Abramov, and P. R. i Cabarrocas, "Absorbing photonic crystals for silicon thin-film solar cells: Design, fabrication and experimental investigation," Solar Energy Materials and Solar Cells **95**, S32-S38 (2011).

6. Design rules for net absorption enhancement in pseudo-disordered photonic crystal assisted thin film solar cell

In this chapter, we will deeply analyze the influence of the pseudo-disorder on the thin film solar cells with numerical RCWA simulations. The pseudo-disordered structure introduced in the 1μm thick c-Si layer stack in the chapter 5 leads to a larger global absorption than the optimized pure periodic cylindrical holes structure both in the numerical and experimental cases. However, the considered stack has no ITO, the thickness is very limited, and the mechanisms of the possible light trapping improvement need further investigation. Meanwhile, a basic stack composition to complete the solar cells, which contains the ITO and metal contact, should be used in the simulations. Therefore, we use RWCA method to optimize the net absorption of pseudo-disordered designs in a realistic solar cell stack with a 1, 2, 4 and 8μm thick c-Si layer compared to the corresponding optimized simply periodic cases.

In the beginning, we first consider as references light trapping structures based on a fully optimized and robust PC solar cell stack. Then, on the basis of the optimized square lattice of holes structure, the pseudo-disordered structures are made of supercells of randomly located holes, periodically repeated in a square lattice. We investigate numerically the absorption mechanisms in such structures, both in the real and Fourier space, with a view to determine design guidelines to enable a net increase of the absorption. At last, we discuss the angular response of the patterned stack.

6.1 Thin film solar cells design and simulation methodology

The solar cell stack considered in this work is depicted in Fig. 6-1a. It consists of a thin absorbing layer of c-Si bonded onto a 1µm thick aluminum (Al) layer that acts as a back mirror and back contact (index see annex 1). Then a 2D PC structure is patterned on top of the c-Si layer, as depicted in Fig. 6-1b and 6-1c. Finally, the patterned c-Si layer is covered by a continuous indium tin oxide (ITO) layer. As shown in Fig.1b, the thickness of the ITO layer is not the same for horizontal surfaces and sidewalls, as it is the case for fabricated solar cells [1].

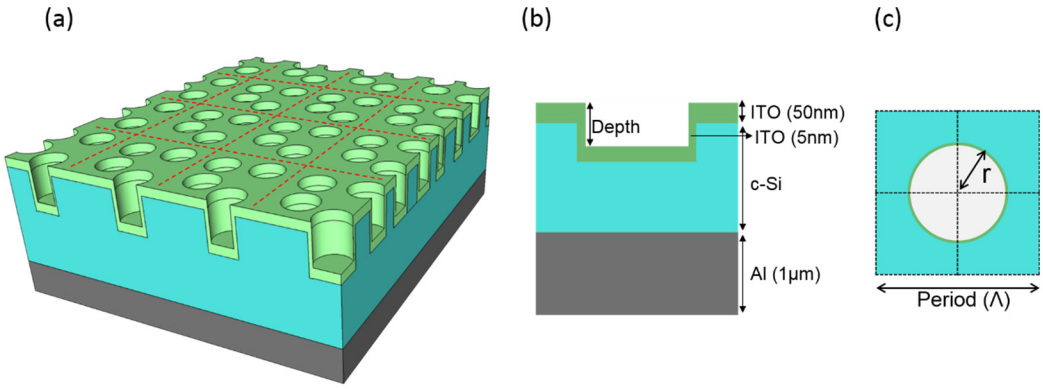

Figure 6-1. (a) Schematic view of the thin film solar cells stack with pseudo-disordered structure. (b) side-view and (c) top view of the thin film solar cell.

Optical indices of the materials are presented in appendix [2, 3]. Unpolarized light at normal incidence is used to mimic the solar illumination. The spectral range is restricted to 300-1100nm, which is realistic for c-Si solar cells. The spectral resolution is carefully chosen considering the absorption peaks linewidth, which depends on the thickness of the c-Si layer. In the short wavelength range (i.e. 300-700nm), the spectral resolution is set to 1nm for all thicknesses of the solar cells. While in the long wavelength range, i.e. 700-1100nm, it is set to 0.5nm for the 1/2/4µm thick c-Si layers, and to 0.25nm for the 8µm thick case. The absorption is calculated thanks to the reflection at the front interface and the transmission at the c-Si/metal interface. It includes the parasitic absorption in ITO; still its impact remains limited and almost constant for all the considered configurations. To establish a fair comparison between a pseudo-disordered structure and a simply periodic one, we first need to optimize the periodic square lattice of air holes structure.

6.2 Optimization of the square lattice of cylindrical holes

The 2D square lattice of air holes is based on the elementary pattern shown in Fig. 6-1b and 6-1c. It is fully determined by three parameters: the period (Λ), the air-surface filling fraction (*ff*) (ratio between the area of the air hole and the total area, given by $ff = \pi r^2/\Lambda^2$, r being the radius of the cylindrical hole) and the etching depth (h). The optimization of the PC structure is performed by scanning these three parameters within technologically realistic ranges: for the 2µm thick c-Si layer stack, the period is comprised between 500 and 660nm, *ff* between 0.3 and 0.5 and the etching depth between 130 and 240nm. The results of the optimization are given in Table. 6-1 for the different thicknesses of the c-Si layer, and for a stack including the Al and ITO layers.

Table.6-1 Achievable current density (Jsc, mA/cm²) with and without a square lattice of holes, for different thicknesses of the c-Si layer. The parameters (period, filling fraction and the depth of the hole) correspond to the maximal value for the optimized square lattice of holes structure.

c-Si (µm)	J_{sc} (mA/cm²)		Period (nm)	Filling fraction (*ff*)	Etching depth (nm)
	Flat	Square Lattice			
1	13.82	19.96	620	0.38	165
2	17.96	23.71	570	0.42	180
4	21.91	27.46	620	0.42	200
8	25.42	30.69	650	0.44	210

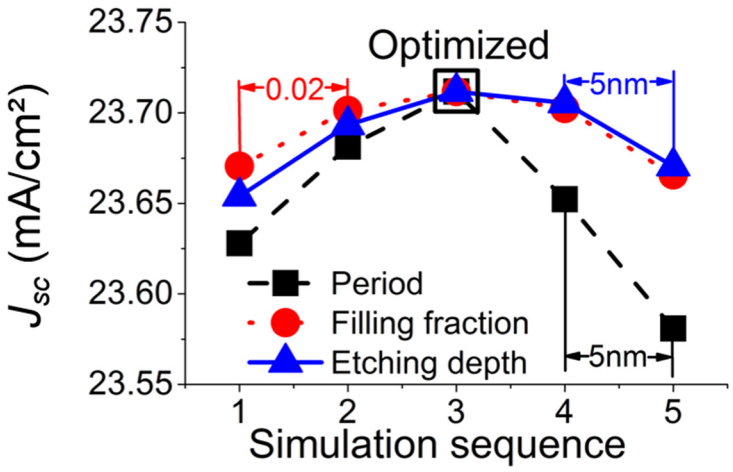

Figure 6-2. J_{sc} calculated for the optimized geometrical parameters in the case of the square lattice of holes with 2µm thick c-Si layers, and for geometries modified to mimic technological fluctuations. Each step of the simulation sequence refers to a modification of each of the three key parameters, with the magnitude shown on the figure.

Thanks to the optimized square lattice of holes, the achievable J_{sc} exhibits a significant increase, up to 44% for the 1µm thick layer. As expected, and observed in the case of other designs [4], this relative enhancement is limited to 21% for the 8µm thick case, even if the volume of the pattern increases thanks to deeper holes. In order to investigate the robustness of the optimized design, we tuned each parameter (period, *ff* and etching depth) from its optimized value in order to mimic technological fluctuations. The result for the stack including a 2µm thick c-Si layer is shown in Fig. 6-2. These slight variations of the filling fraction (0.02 step) as well as of the etching depth (5nm step) have a limited influence on the optical performance of the thin film solar cells: the maximal J_{sc} decrease is only of 0.05mA/cm². While the influence of the period (5nm step) is more important, this parameter can be more easily controlled than the other two during the fabrication process. This robustness of the J_{sc} with regards to the geometrical parameters enables a good compatibility with standard technological processes. As shown in the following, the typical influence of the fluctuations (of the order of one-step, as indicated on Fig. 6-2) is far below the effect of the controlled perturbations introduced in pseudo-disordered structures.

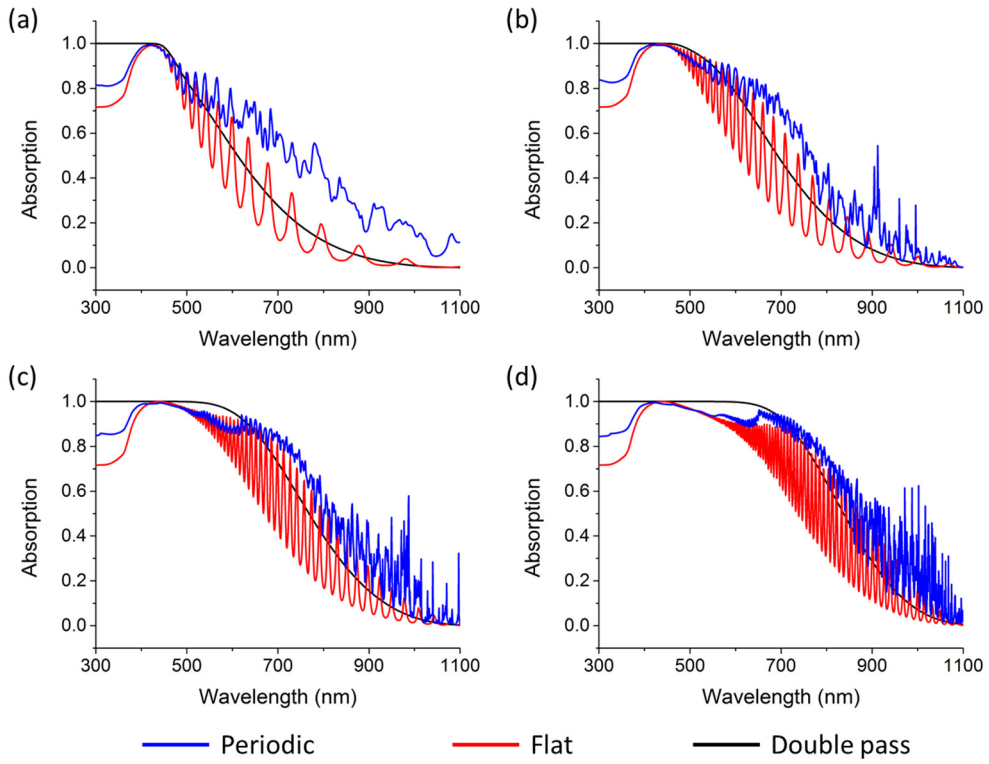

Figure 6-3. Absorption spectra of the unpatterned structure (red line), the optimized square lattice of holes (blue line) and the corresponding thickness absorption of double pass (black line) for different thickness of the c-Si layer from 1 to 8 µm..

Fig. 6-3 shows the comparison of absorption spectra between the flat and the optimized square lattice of holes structure, as well as the double pass absorption spectra with different thicknesses of c-Si layer, from 1µm to 8µm. No sharp absorption peak appears in the wavelength range from 300 to 500nm, where the penetration length of the photons in the c-Si is shorter than the absorbing layer thickness. For the wavelength range from 500 to 700nm, several absorption resonances corresponding to the Fabry-Perot modes come out. In the 700-1100nm, wavelength range, and compared to the unpatterned stack, the square lattice of holes structures exhibit densely packed and irregular absorption peaks due to Bloch mode resonances [5]. Besides, for each selected thickness, the absorption spectrum of the optimized square lattice of holes is almost always higher than the absorption of the flat thin-film stack. This type of behavior is well established in solar cell stacks including simply periodic patterns in absorbing layers in the micrometer range, see e.g. [1, 5]. Compared to the flat design and the double pass scheme, the absorption of the optimized PC structure is clearly above them: this is a clear additional proof of light trapping effect.

6.3 Pseudo-disordered lattices of cylindrical holes

6.3.1 Pseudo-disordered supercells definition

In order to further increase the absorption of thin film solar cells, we propose to integrate pseudo-disordered nanopatterns. In a square lattice of holes PC, the structure is highly efficient only for specific wavelengths; this corresponds to the sharp peaks displayed in Fig. 6-3. To overcome these limitations, pseudo-disordered PC structures relying on carefully controlled positioned holes will be exploited.

In such designs, each hole of a supercell is moved from its original position as shown in Fig. 6-4a. The hole is shifted by a distance *dp*, with an angle of α. The value of *dp* is determined by a Gaussian distribution, while the angle is determined by a uniform distribution. Then this perturbation process is applied to N^2 holes (e.g. 3×3, depicted in Fig. 3b) composing a $N \times N$ supercell. This supercell is then replicated in a square lattice. To avoid numerical issues and to keep a realistic design, only the cases in which holes do not merge are considered.

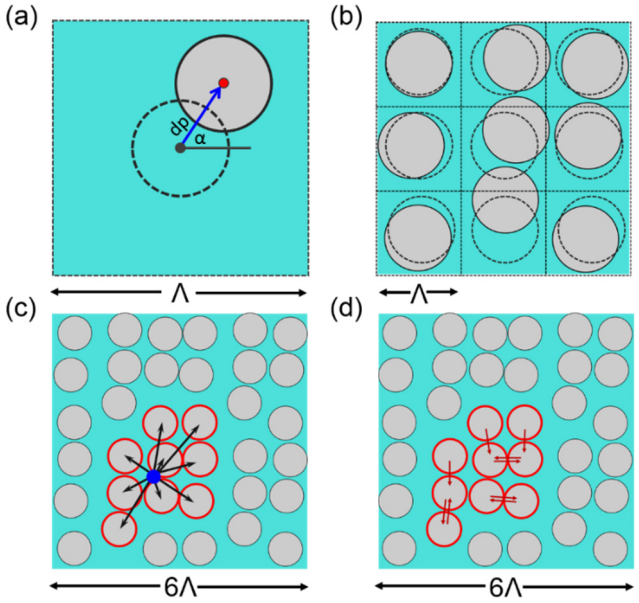

Figure 6-4. Schematic view of the perturbation (a) for a single hole and (b) for 9 holes in a 3×3n supercell structure. (c & d) Determination of the pseudo-disordered structure parameter thanks to replication of the 3×3 supercell. (c) The blue point represents the centroid of the selected red holes, which is used to determine the "compactness" parameter. (d) The minimum distance between the 9 holes depicted by the red arrows determines the "clustering" parameter.

As the pattern designs are obtained by using a non-deterministic process, the effect of the pseudo-disorder is evaluated by the protocol defined below. Since the *dp* is determined thanks to a Gaussian distribution, we simulated at least 10 different pseudo-disordered structures with the same mean *dp* value for three different supercell sizes (from 2×2 to 4×4). This has been done for four different values of the mean *dp*, We additionally consider all the thickness mentioned previously (1, 2, 4 and 8µm thick c-Si layer).

6.3.2 Metric parameters for pseudo-disordered structures

As shown later, supercells exhibit various shapes that can lead to very different situations, like clusters of holes or more evenly positioned and spaced holes. In order to analyze the effects of the introduced disorder in the real space, we need to define relevant metrics that can classify the pseudo-disordered structures. Thus, we define two parameters to describe the pseudo-disordered structure, in terms of clustering and compactness.

Among all the possible arrangement of holes within the lattice of supercells, we select that with the lowest mean distance between each of the N^2 holes and their centroid. In the example shown in Fig. 3c) and d), the group of N^2 holes selected using this criterion corresponds to the red circles, this group constitutes an alternative supercell to the initial square one. This lowest mean distance will be referred to as the compactness parameter. This parameter obviously grows with N. Then, for the corresponding set of N^2 holes, we compute the average distance between each hole and its nearest neighbor (Fig. 3d). This value will be referred to as the clustering parameter; a low clustering value corresponds to the presence of cluster(s) of holes in the supercell. It also means that a low compactness parameter associated to a low clustering value indicates that the pattern is made of a single cluster of N^2 holes, whereas a large compactness parameter with a low clustering value corresponds to several clusters of holes. While one can anticipate that these two parameters are insightful for the investigation of pseudo-disordered structures, it should be noticed that they are not meant to fully describe them.

6.3.3 Best / worst pattern results

The maximal / minimal achievable J_{sc} for pseudo-disordered structures among all the calculated patterns for each considered thickness are summarized in Table. 2. For all the considered thicknesses, the J_{sc} associated to the best pseudo-disordered structure is always higher than the J_{sc} of the optimized square lattice of holes. The best pseudo-disordered structures exhibit a relative increase of 2% in J_{sc} in the 2, 4 and 8µm thick c-Si layer stacks, but only a very limited increase can be obtained for the 1µm thick c-Si layer stack. For this lowest thickness, the clustering and the compactness parameters are occasionally the same, but the distributions of the holes are different, leading to different values of J_{sc}. Since the current will anyway remain limited for 1µm thick c-Si layer, we will focus on larger thicknesses in the following.

Table 2. Achievable current density (J_{sc}, mA/cm²) for the different thicknesses of c-Si layer for 3 specific cases: optimized square lattice of holes and extrema results (best and worst) obtained on pseudo-disordered structures.

c-Si (µm)	Square Lattice	Pseudo-disordered structures	
		Best	Worst
1	19.96	20.02	19.48
2	23.71	24.38	23.59
4	27.46	27.95	27.51
8	30.69	31.28	30.56

It is noticeable that for the 2 to 8µm thick c-Si layers, the best pseudo-disordered structures always exhibit a higher clustering parameter (i.e. less clusters of holes) than the structures leading to the lowest J_{sc}. It should additionally be noted that while the highest J_{sc} corresponds to a 2×2 supercell in the 2 and 8µm thick layers, it is a 3×3 supercell in the 4µm case. The compactness parameter is higher in the latter case since it also depends on the supercell size. In addition, for a lower thickness, the best pseudo-disordered structures are achieved with a relatively low mean shift ($dp \approx 11$nm),

especially for the 1μm thick c-Si layer stack. As the J_{sc} is obtained from the integrated absorption spectra, we will now focus on these in the following section.

6.3.4 Absorption spectra analysis

In this section, the absorption spectra of the optimized pseudo-disordered structure will be analyzed. Firstly, we will focus on the absorption spectra and then compare with result of the corresponding thick optimized square lattice of holes to realize the main enhancement range. Secondly, focusing on the increase range, we will characterize the absorption spectra to realize the light coupling.

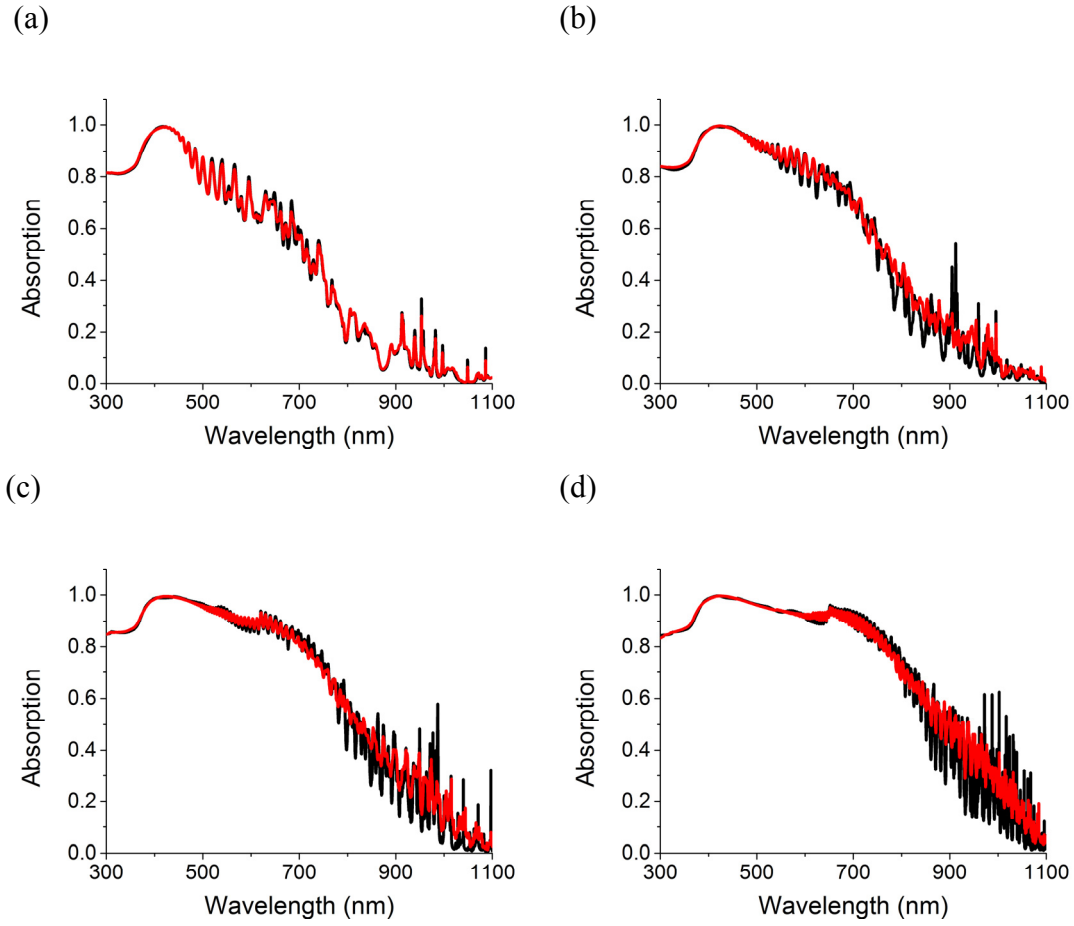

Figure 6-5. The comparison of the absorption spectra of the optimized square lattice of holes (black line) and the best pseudo disordered structure (red line) with the 1μm (a), 2μm (b), 4μm (c) and 8μm (d) thick c-Si layer stack.

Fig. 6-5 displays the absorption spectra of the square lattice of holes and the pseudo-disordered structure in each thickness of the c-Si layer stack. From the result of

the different thickness shown in Fig. 6-5a, b, c and d, the absorption spectra of the pseudo disordered structures are clear smoother than the corresponding square lattice of holes structure, which both the maximum and minimum amplitude of the peaks are smaller in the pseudo-disordered designs. On the contrary, in the short wavelengths range of 300-700nm, there is almost no difference in the absorption spectra between the two designs, indicating lower impact on the anti-reflection effect with pseudo-disorder compared to the square lattice of holes pattern. In the 1µm thick case, the optimized pseudo-disordered structure with this thickness is a quite specific case, in which the spectrum is very close to the square lattice of holes structure, due to smaller positional perturbation.

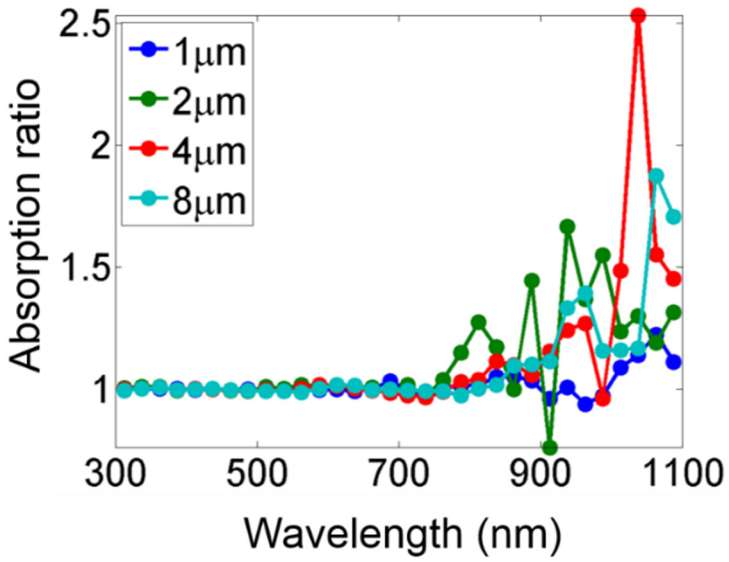

Figure 6-6. Ratio of the absorption associated to the best pseudo-disordered structure divided by the absorption corresponding to the optimized square lattice of holes structure. For a sake of clarity, this ratio is averaged over a 25nm spectral range.

In order to clearly identify the enhancement by the introduced pseudo-disorder, Fig. 6-6 displays the ratio between the absorption in the best pseudo-disordered structures and that of the optimized square lattice of holes, in the case of the four different c-Si thicknesses considered here. On this figure, it clearly appears that the improvement mainly occurs at long wavelengths (700-1100nm), where the Bloch modes can efficiently trap the incoming sun light. On the contrary, in the short wavelengths range, 300-700nm, the pseudo-disorder doesn't impact the anti-reflection

effect of the square lattice of holes pattern. Additionally, the main increase by the introduced pseudo-disorder occurs at longer wavelengths for a thicker c-Si layer stack.

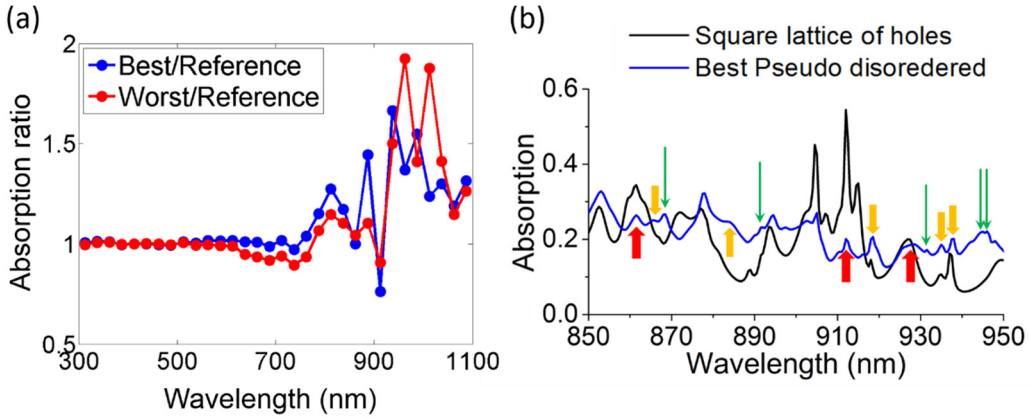

Figure 6-7. (a) Ratio of the absorption associated to the best/worst pseudo-disordered structure divided by the absorption corresponding to the optimized square lattice of holes structure for the 2µm thick c-Si layer stack. For a sake of clarity, this ratio is averaged over a 25nm spectral range. (b) Comparison between the absorption spectra of the best pseudo-disordered structure and the optimized square lattice of holes design for a spectral range comprised between 850 and 950nm in order to highlight new absorption peaks (depicted by green arrows), broaden peaks (depicted by slide yellow arrows) or small magnitude peaks (depicted by red arrows).

Among the different thicknesses of the c-Si layer stack, we focus on the case of the 2µm thick designs to analyze the pseudo-disorder effect. Fig. 6-7b shows the ratios between the best or worst pseudo-disordered structures and the optimized square lattice of holes, in the case of 2µm thick c-Si layers. The main differences between these two spectra are in the 500-1100nm wavelength range. The worst pseudo-disordered pattern exhibits a significantly lower (2.5% decrease) absorption than the reference optimized square lattice of holes in the 500-700nm range. In the 700-1100nm wavelength range, both spectra corresponding to best and worst pseudo-disordered structures exhibit a higher absorption than the reference. The obtained enhancement for the best pseudo-disordered structure reaches a value of 10.9%, while this value is divided by a factor 2 for the worst pseudo-disordered structure. Moreover, though the absorption ratio corresponding to the worst structure is higher than the one corresponding to the best

one around 1000nm, there is less AM1.5G solar photon flux in that range, resulting in a lower enhancement.

Detailed absorption spectra are given in Fig. 6-7b, for the 2µm thick layer stack. Compared to the optimal square lattice of holes, the absorption spectrum of the best pseudo-disordered pattern exhibits broadened peaks, and peaks with smaller amplitude. It also displays additional peaks corresponding to higher diffraction orders due to the larger periodicity; the corresponding modes contribute to the absorption enhancement [6]. The broad and low amplitude peaks can also lead to a larger integrated absorption than sharp, high amplitude peaks [7-9].

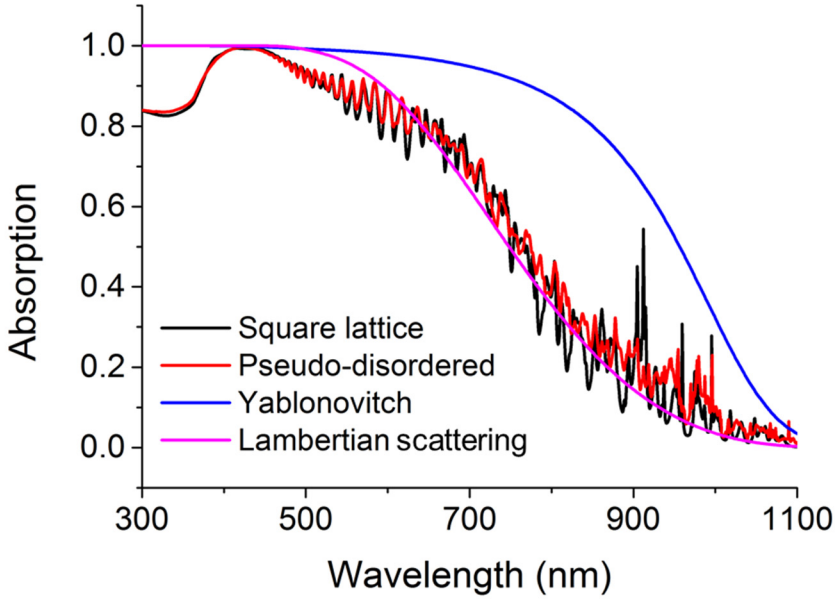

Figure 6-7. The absorption spectra of the Yablonovitch limit and Lambertian scattering limit in the 2µm thick case, as well as the optimized square lattice of holes and best pseudo-disordered designs.

Then we consider the absorption of the optimized square lattice of holes and the best pseudo-disordered design compared to the widespread limit of Yablonovitch and Lambertian scattering limit, which are fundamental benchmarks for the PV solar cells (see Annex 3). From the Fig. 6-7, it can be realized that the absorption for both patterned solar cells is mainly above the Lambertian scattering limit at large wavelengths. This proves a good light trapping. However, since even the absorption of the best pseudo-disordered structure is still below the Yablonovitch limit, there might be room for further increase of the spectral density of modes in the thin film. In any case, it is

established that the Yablonovicth limit suits mostly for bulk solar cells. It can thus only be reached at a limited wavelength range in thin film solar cells.

6.4 Analysis of the pseudo-disordered structure

It has been shown that depending on the considered pseudo-disordered structure, the integrated absorption, and thus the J_{sc}, can either be increased or decreased compared to a fully optimized square lattice of holes. So in this section, we will investigate the link between the real/reciprocal space distribution of holes inside the $N \times N$ supercell and the absorption efficiency of the solar cell stacks.

6.4.1 Real space analysis

In order to sort the distribution of holes in the real space, we will refer to the metric parameters presented in section 6.3.2. For the 2µm thick c-Si layer stack, all the results from simulation are plotted in Fig. 6-8a. If few holes are too close to each other, leading to a low clustering value, as in the holes distributions shown in Fig. 6-8f and 6-8g, the resulting J_{sc} is low. If additionally the compactness parameter is low, like for the distribution of holes in Fig. 6-8e, there is only one cluster of holes within each $N \times N$ supercell and then the J_{sc} of the pseudo-disordered structure is even lower. The highest values of J_{sc} are obtained for pseudo-disordered structures that exhibit relatively high value of the clustering. For the 2×2 supercell, the statistical analysis indicates that the structure corresponding to the highest J_{sc}, presented in Fig. 6-8b, exhibits a "homogeneous" distribution, with evenly distributed holes and no clustering effect. On the contrary, the pseudo-disordered structure corresponding to the lowest J_{sc} presented in Fig. 6-8e exhibits the opposite situation. For the 3×3 and 4×4 supercells, the highest obtained J_{sc} corresponds to larger clustering parameters (Fig. 6-8c and 6-8d), even if not the largest one. The lowest J_{sc} corresponds to patterns which exhibit a strong clustering (Fig. 6-8f and 6-8g), the clustering parameter being among the lowest values of the sampling.

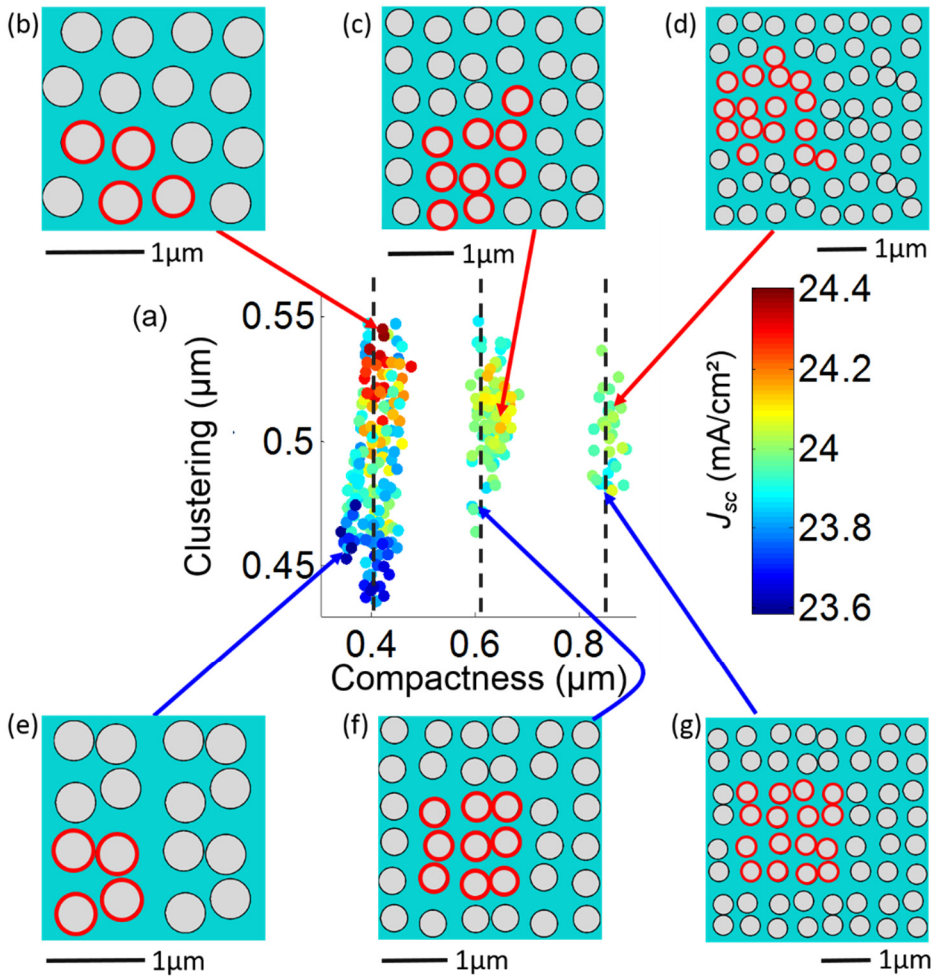

Figure 6-8. Current density (J_{sc}, mA/cm²) map (a) as a function of clustering and compactness parameters of pseudo-disordered structure for the 2μm thick c-Si layer case. The dashed black lines represent the compactness parameter of the optimized square lattice of holes (reference) structure for 2×2 supercell (close to 0.40μm), 3×3 supercell (~0.61μm) and 4×4 supercell (~0.85μm). The clustering parameter of the optimized square lattice of holes structure corresponds to the period of the lattice and is 0.57μm. The schematic views correspond to hole distribution of the pseudo-disordered structure that exhibit highest J_{sc} for 2×2, 3×3 and 4×4 supercells (b, c, d) lowest J_{sc} for the same cases (e, f, g). The red circles highlight the selected hole of the supercell.

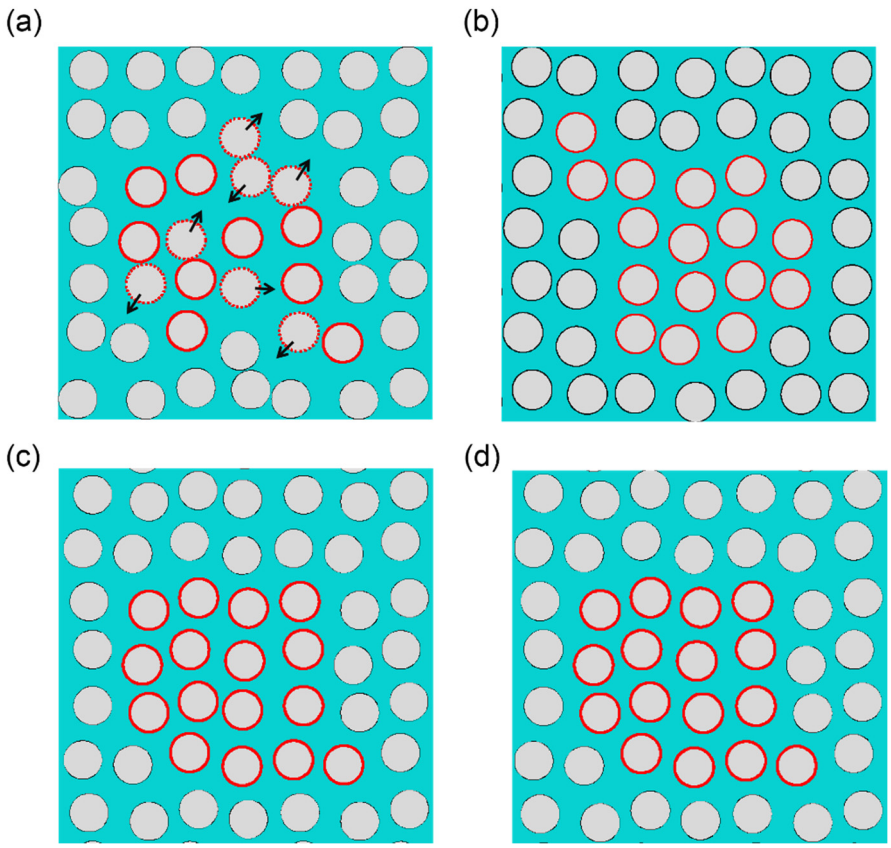

Figure 6-9. The schematic view of the best 4×4 pseudo-disordered structure from the set of simulation discussed above and already shown Fig. 6-9d is shown again, together with the structure modified using the design rules inspired from the 2×2 supercell analysis. From the original distribution (a), selected holes (depicted the red dash circles) are shifted in the direction depicted by the arrow in order to break the small clusters of holes, leading to more homogeneously distributed holes (b, c and d).

However, it is still possible to further optimize such patterns using these conclusions as a design rules, especially in the case of 4×4 pseudo-disordered structures. Indeed, in this case, considering that the simulations are highly time consuming, the number of situations analyzed is not sufficient to approach the optimum structure. Since the best 4×4 pseudo-disordered structure displayed in Fig. 6-9d still exhibits clusters of holes, this structure can be further modified by moving the holes marked by the red dash circles in the direction shown by the arrow (Fig. 6-9a). The resulting designs are from the Fig. 6-9b to the Fig. 6-9d seems to be more homogeneous.

(a) (b) (c)

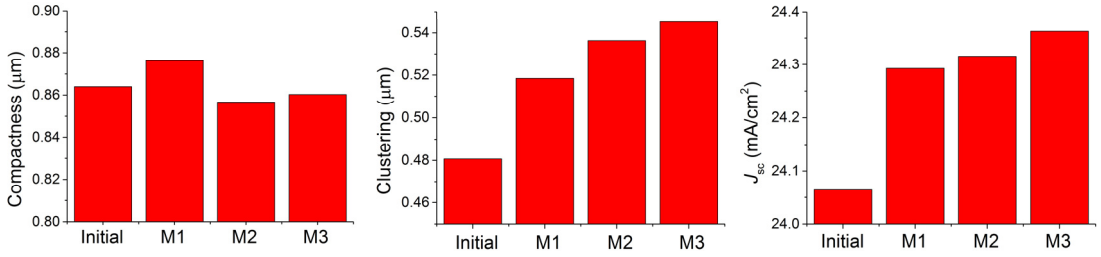

(d)

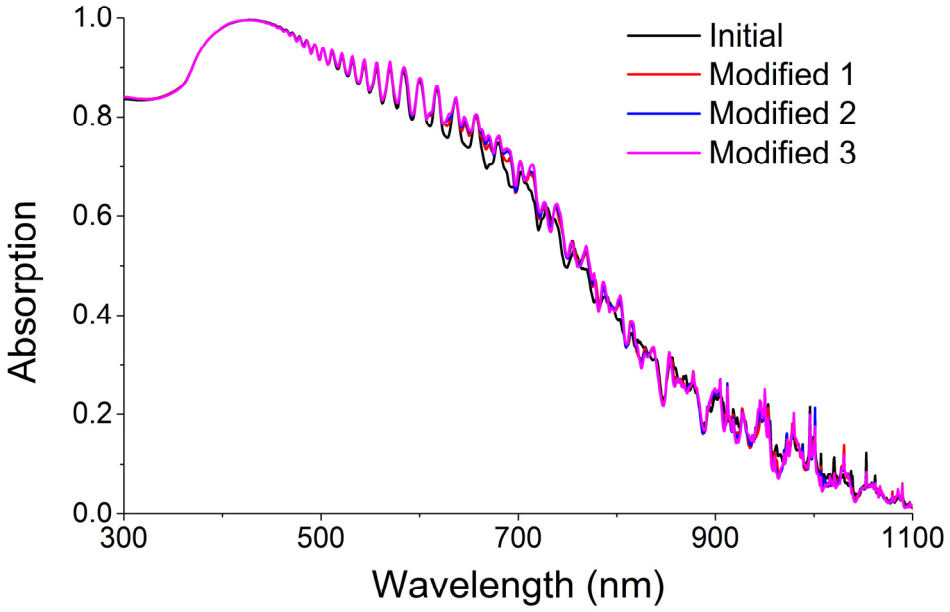

Figure 6-10. Current density (a), compactness parameter (b), clustering parameter (c) and absorption spectra (d) of the original design and the refined designed, which the modified 1 (M1), modified 2 (M2) and modified 3(M3) correspond to the design in Fig. 6-9b, c and d respectively.

The resulting metrics are in Fig 6-10a and b. As shown in Fig 6-10c, the best J_{sc} is obtained for "M3", i.e. the design in Fig 6-9d. The best modified pseudo-disordered design has a higher clustering parameter, indicating a low clustering effect as discussed previously. Since the initial design is already a relatively good design before the refinements, the compactness is only slightly lower, as it can be seen as a second order parameter to constrain the clustering effect. As a consequence, a J_{sc} (Fig. 6-10c) of 24.36mA/cm² is obtained, 0.30mA/cm² above that corresponding to the initial 4×4 pseudo-periodic structure, which is significantly higher (+2.7%) than the J_{sc} expected for the optimized square lattice pattern. It should be noted that even for this refined 4×4 pseudo-disordered structure, the derived J_{sc} remains smaller than that of the best 2×2

case. As all the 2×2 supercell possibilities are only a part of the 4×4 supercell possibilities, the pseudo-disordered structures in 4×4 supercells need more permutations and combinations to achieve a fully optimal design.

From the evolution of the absorption spectra from the initial pseudo-disordered design to the modified cases, we could see the enhancement mainly occurs in the 500-750nm wavelength range (+3.6% of integrated absorption). Conversely, in the wavelength range of 750-1100nm, the integrated absorption of the best-modified design has a relative 2% decrease. Indeed, the relatively highly perturbed design (corresponding to a low value of the clustering parameter among these four designs) could increase the absorption in a long wavelength range, but it is not sufficient to cover the losses in other wavelength range. Meanwhile, the magnitude of solar spectrum in the wavelength of 750-1100nm is lower in the range of 500-750nm, it also could explain the best-modified pseudo-disordered design has a better J_{sc}.

While the influence of clustering and compactness parameters has been discussed for the 2μm thick c-Si layer case, similar results have been found for the 4 and 8 μm thicknesses. The negative influence of clusters of holes can be related to a result established by Bozzola et al [10] for 1D binary gratings with perturbed widths and positions. Indeed, they have found that the deviation of the pattern width should be half of the position shift, thus reducing the risk of clustering patterns. In this section, we have investigated the pseudo-disordered structure in the direct space; we will now discuss on the basis of the analysis in the reciprocal space.

6.4.2 Spatial frequency analysis

Fig. 6-11 presents the discrete Fourier space map of the dielectric function of the optimized simple PC structure with a square lattice (Fig. 6-11a) and the pseudo-disordered structures (Fig. 6-11b) in the 2μm thick c-Si layer stack. Pseudo-disordered structures, with larger periods than the square lattices of holes, obviously exhibit richer frequencies distributions. In order to make a clear comparison of the changes in the Fourier components, we transfer these 2D maps into 1D in the following, integrating the spatial frequencies in the thin layer plane, over 360° in polar coordinates. As in the case of the analysis in the real space, only the stack based on the 2μm c-Si layer will be detailed.

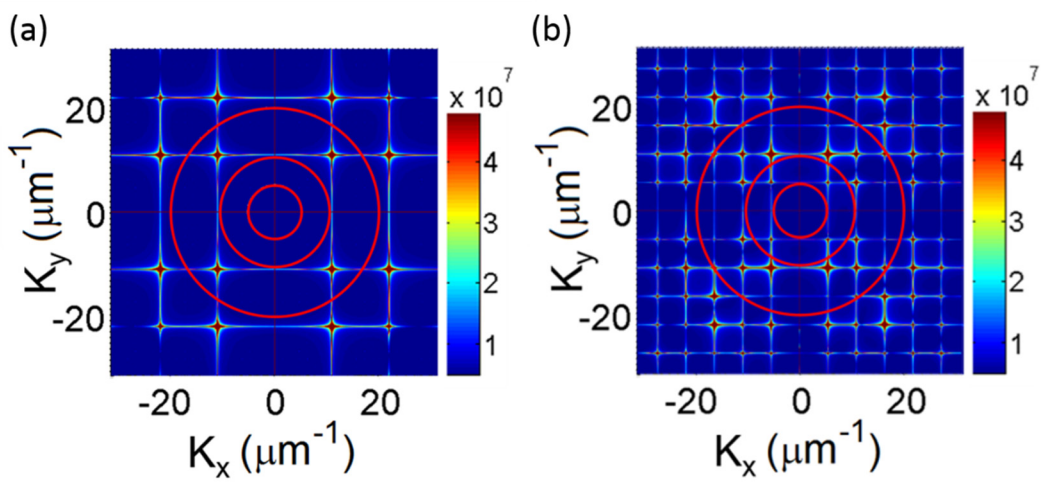

Figure 6-11. Fourier space map of the topography of the optimized square lattice of holes structure and pseudo-disordered structure in a 2×2 supercell. The red circles represent the k at 5.2, 10.5 and 20.1μm^{-1} respectively.

The angularly integrated magnitude (along the azimuth) of the Fourier component of the dielectric functions of few selected structures (the best and worst pseudo-disordered structures, and the optimized square lattice of holes structure), which will be referred to as the AIMF, are plotted in Fig. 6-12a, b and c for each supercell size. In these three figures, it appears that the AIMF of all pseudo-disordered structures are almost always higher than the ones of the optimized square lattice of holes, over the whole spatial frequency range of interest. In addition, it appears that the worst structures exhibit low spatial frequency components (<10μm^{-1}) with higher amplitudes than the best designs. Then focusing on the best pseudo-disordered structures for each different supercell size (Fig. 6-12d) and compared to the optimized square lattice of holes, it is noticeable that the best J_{sc} is obtained in the 2×2 case, and corresponds to the smallest increase of the Fourier components in the low spatial frequency range (<10μm^{-1}).

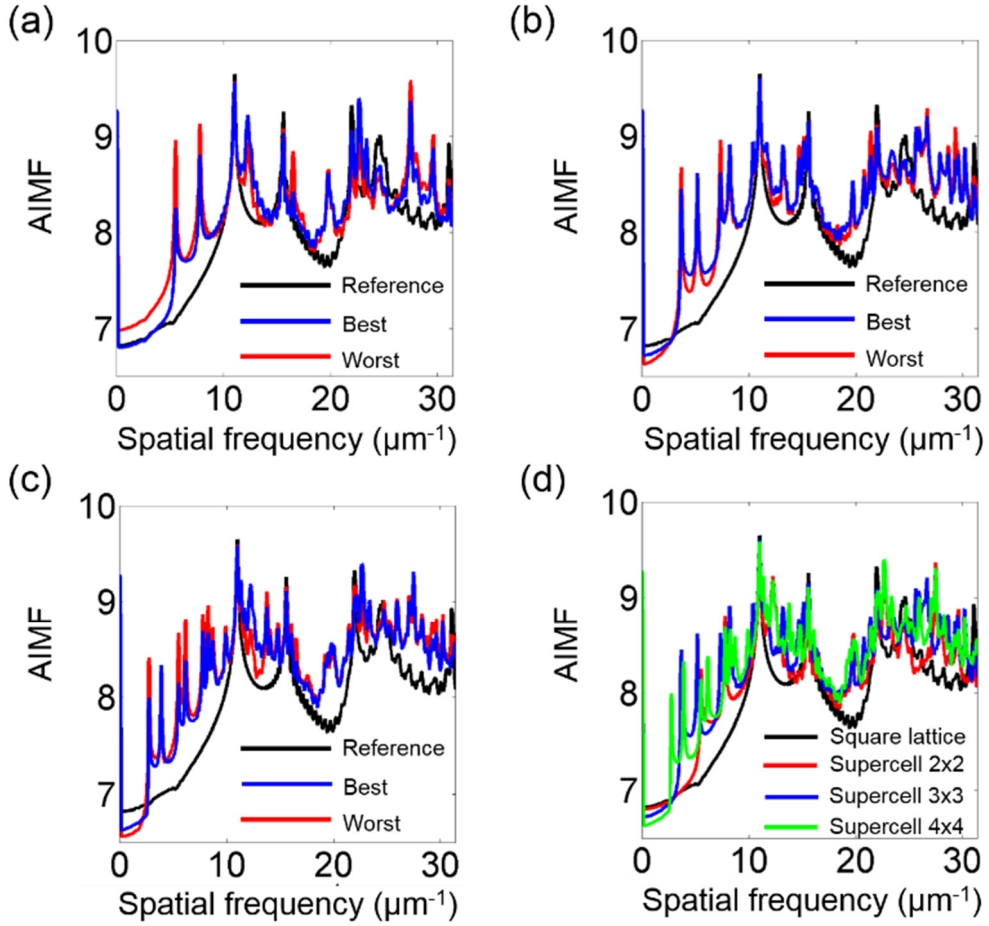

Figure 6-12. Angularly integrated magnitude of Fourier component of the dielectric function of the considered nanostructure is integrated over polar coordinate (AIMF). For the 2μm thick c-Si stack, the results for the best (res. worst) pseudo-disordered structure is plotted in blue (resp. red) line and for the optimized square lattice of holes structure in black in the case of a 2×2 (a), 3×3 (b) and 4×4 (c) supercell. The best pseudo-disordered structure for each supercell size and the square lattice of holes structure are also plotted together (d).

These results can be compared to previous works on complex absorbing patterns. It is firstly supposed that at normal incidence, the diffraction efficiency of incoming light and thus the absorption of a thin layer are directly proportional to the magnitude of the Fourier component of the dielectric function. Under this assumption, Bozzola et al. [10] chose to increase the diffraction efficiency in the high frequency range, which leads to a structure that makes use of numerous components of possibly high amplitude. On the other hand, Martins et al [11] directly optimized their structure in the Fourier space considering that the air light line corresponds to the limit between quasi-guided,

trapped mode and photon leakage. Their optimization led to a pattern that exhibits Fourier components with low magnitude in a low frequency range, up to $2\pi/\lambda_0$ with λ_0 corresponding to a wavelength where the absorption in silicon becomes weak. In our case, we set the limit between the low and high frequency ranges to $2\pi/\Lambda$, Λ being the period of the square lattice of holes, close to the value of λ_0 chosen in [11].

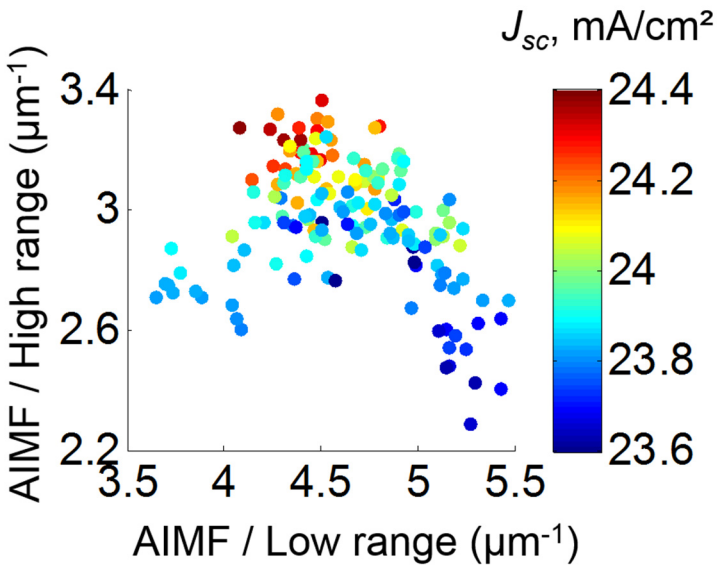

Figure 6-13. Current density (J_{sc}, mA/cm²) map of the 2µm thick c-Si layer stack patterned by pseudo-disordered structures in a 2×2 supercell in function of the weight of low and high frequency components. The weight of low (resp. high) frequency components is determined by the AIMF in [0 $2\pi/\Lambda$] (resp. [$2\pi/\Lambda$ $4\pi/\Lambda$]).

Our results are then sorted according to the previous two criteria. For 2×2 supercell and the 2µm thick c-Si layer stack, the current densities are displayed as a function of the AIMF over the two frequency ranges, as shown in Fig. 6-13. High values of J_{sc} are achieved for patterns with large magnitude of the integrated dielectric function in the high frequency range, and a relatively low magnitude in the low frequency range. It then appears that both criteria suggested in the former studies mentioned above are overall satisfied.

However, since the air filling fraction is always the same as the one of the optimized square lattice of holes, the integration over the full spectral range of the square of the magnitude of the Fourier components of all structures of a given thickness is constant, according to the Parseval's theorem. Thus, the achievable values over the

two selected frequency ranges are limited. But still, such considerations could make it possible to minimize the quantity of pseudo-disordered structures to be simulated and this indicates guidelines for the optimization, which is especially valuable for large supercells.

Finally, as mentioned previously, the distribution of the Fourier components of the various structures considered have been constrained considering a fixed area filling fraction. In that sense, clusters of holes can simultaneously lead to significant diffraction at low and very high (higher than $4\pi/\Lambda$) spatial frequencies, and thus may not satisfy the previous criteria. This confirms the tendency observed in the real space. All these analyses are done under normal incidence. Considering the large number of addressable optical modes, pseudo-disordered structures are also expected to be less sensitive to the angle of incidence of the impinging light. This will be investigated in the next section.

6.5 Angular response of the PC architecture

The absorption under oblique incidence is a critical property for photovoltaic devices without solar trackers. As depicted in Fig. 6-14a and for a nanopaterned stack, the oblique unpolarized incidence is characterized by two parameters: the incident angle (θ) and the conical angle (Φ). In order to determine J_{sc} under an incidence angle (θ) in a rigorous way, we calculate the average of J_{sc} for all conical angles Φ (from 0° to 360° with a step of 45°).

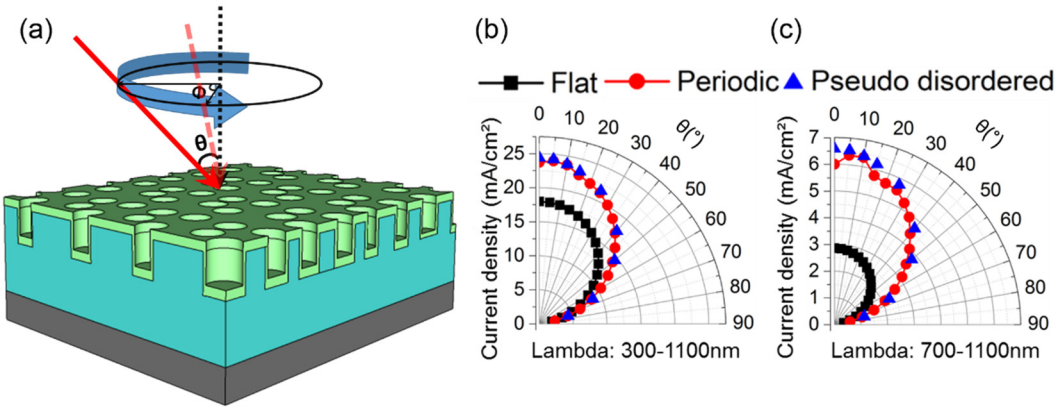

Figure 6-14. (a) Schematic view of an oblique incident light under an incidence angle θ with a conical angle Φ. For the 2µm thick c-Si layer stack, evolution of J_{sc} for the optimized square lattice of holes structure (red dot), for the best pseudo-disordered structures (blue triangle) and for the flat case (black square) over a spectrum which extends from 300 to 1100nm (b) and from 700 to 1100nm (c).

The short circuit current density predicted using this approach is plotted in Fig. 6-14b for the whole range of angles of incidence (θ), and for different structures: the unpatterned stack, the optimized square lattice of holes structure and the best pseudo-disordered structure in the 2×2 supercell, with 2 µm thick c-Si layers. Firstly, this shows that the J_{sc} value associated to the best pseudo-disordered structure is always higher than that corresponding to the optimized square lattice of holes structure. Secondly, the optimized square lattice of holes structure exhibits an unusual increase of J_{sc} at small angles (around 5-10° off the vertical axis) due to the possibility of coupling the incident light into resonances by the symmetry breaking under the oblique incidence [12, 13]. Around this angle, the difference between the optimized square lattice of holes and the best pseudo-disordered structure is the lowest; it is only 0.5% higher with the pseudo-disordered structure. For a higher angle of incidence, the difference in J_{sc} increases up to 2.3%. Overall, in all cases, the J_{sc} decreases when the angle of incidence is increased. This behavior is general for all types of solar cells without trackers, and is mainly due to a decrease of the incidence power density at the surface of the solar cells; this is a simple geometrical effect. As shown on the averaged spectra of Fig. 6-6, the pseudo-disorder especially influences absorption efficiency in the long wavelength range. Focusing on the 700-1100nm range (Fig. 6-14c), the impact of nanopatterning doubles the absorption efficiency of a flat thin layer stack for all incidence angles. As expected, the gain between pseudo-disordered structure and square lattice of holes structure is

higher for that wavelength range, with a relative increase up to 4.4%. Finally, one can notice that the J_{sc} fluctuations occurring below 30° for the square lattice of holes disappear in the case of the pseudo-disordered structure, leading to a slowly decreasing J_{sc} for large angles of incidence.

6.6 Perturbation of the diameters of the holes the size of the element

Until now, we have considered pseudo-disordered structures obtained only by shifting the position of the holes. In fact, the changes also could occur on the size of the holes [12, 14], as well combine both of them to compose the pseudo-disordered structure.

The following preliminary results intends to pave the way for more complete future developments on the topic.

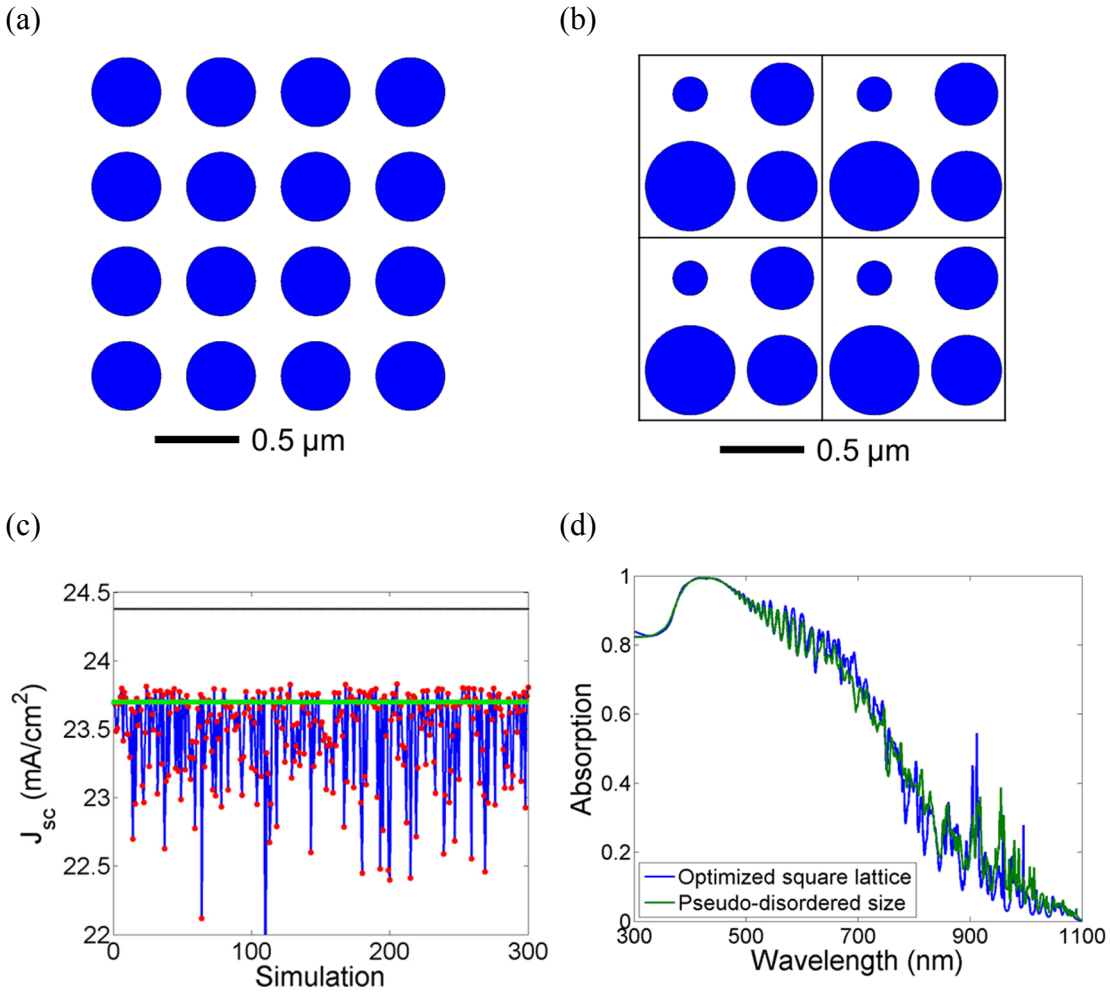

Fig 6-15. Pseudo-disordered structure based on the perturbation of the size of the holes. (a) Schematic image of the optimized square lattice of holes in the 2 μm thick c-Si layer stack. (b) Schematic image of best pseudo-disordered sized design in a 2×2 supercell. (c) Distribution of the current density (J_{sc}, mA/cm²) of the pseudo-disordered sized simulations with different size of the holes. The green line represents the J_{sc} of the optimized square lattice of the holes, and the dark line represents the best design of pseudo-disorder in position in a 2x2 supercell in the previous simulations (d) Comparison of absorption spectra between the best design of pseudo-disorder in size and the optimized square lattice of holes.

Firstly, we consider the perturbation only on the size of the hole, which the sized perturbation is introduced into the optimized square lattice of holes structure (Fig 6-15a). The position of the holes is kept, while we change the size of the holes under the Gaussian distribution. It should be noted the total filling fraction in a supercells is constant, and the overlapping should be avoided. For instance, the design of pseudo-

disorder in size in 2×2 supercells in a 2 μm thick c-Si thin film in the stack is considered. However, the J_{sc} of the appropriate pseudo-disorder in size (Fig. 6-15b) among 300 simulations (Fig. 6-15c) is only better than the optimized square lattice of holes design, but it remains far from the best design of pseudo-disorder in position deriving from the previous simulations. From these results, it seems that pseudo-disordered sized design could not provide sufficient modes compared to the shifted position (Fig. 6-15d).

Secondly, we introduce the perturbations on both the position and size of the holes. For instance, the perturbation is introduced in the size of the holes using the best pseudo-disordered positional structure in a 2×2 supercell (Fig. 6-16a). It means the position of the holes in this best pseudo-disordered positional design is kept, meanwhile the size of holes is changed under the Gaussian distribution in order to find the best case (Fig. 6-16b). Indeed, this dual pseudo-disordered concept with both positional and sized pseudo-disordered design could easily defeat the optimized square lattice of holes. However, the best dual pseudo-disordered design only has a limited increase compared to the reference of the best pseudo-disordered positional design (Fig. 6-16c), and the corresponding spectra almost overlap each other (Fig. 6-17).

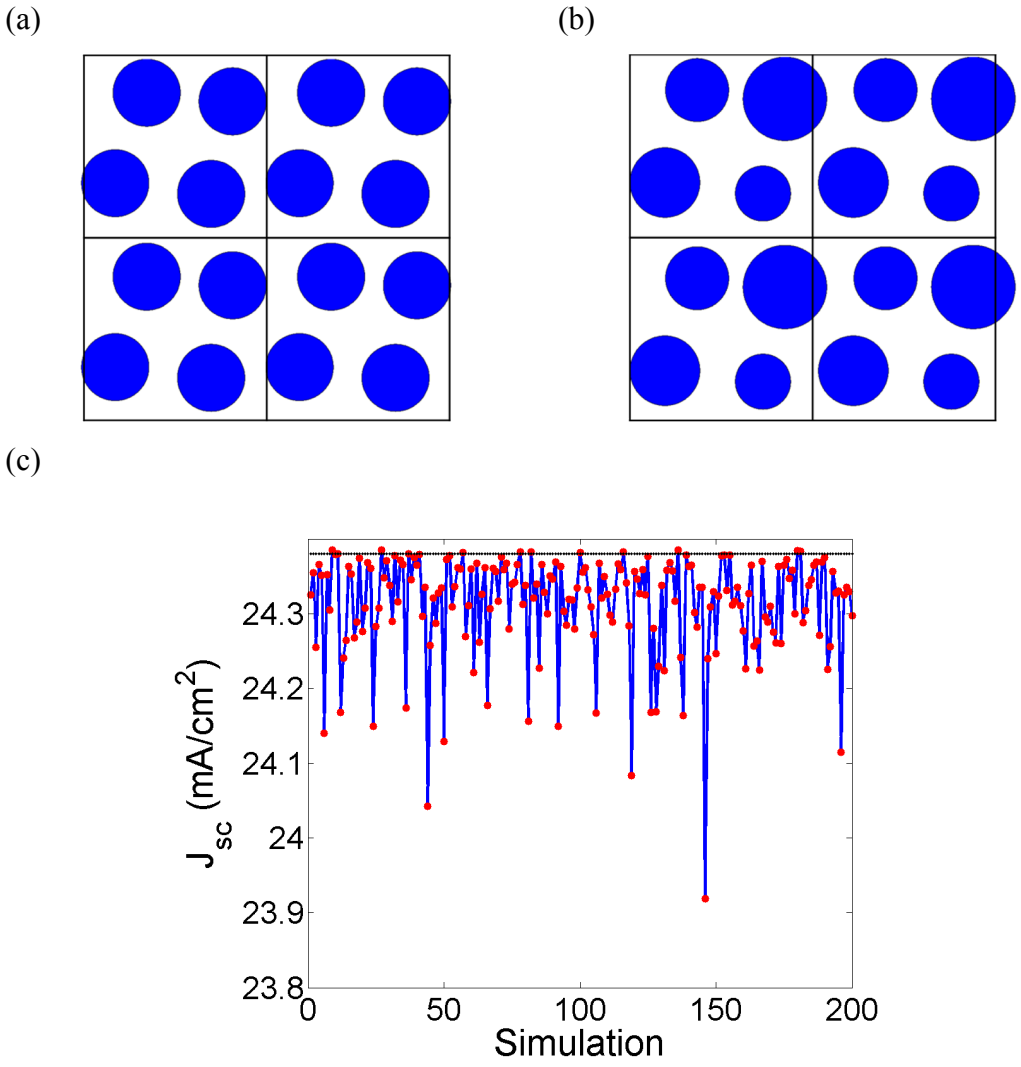

Fig 6-16. Pseudo-disordered structure based on the perturbation on both the position and size of the holes. (a) Schematic image of the best pseudo-disordered positional design in 2x2 supercells with 2 μm thick c-Si stack. (b) Schematic image of the best dual (position and size) pseudo-disordered design in a 2×2 supercell. (c) Distribution of the current density (J_{sc}, mA/cm²) of the dual pseudo-disordered simulations with different size of the holes. The dark line represents the best pseudo-disordered positional design in a 2x2 supercell in the previous simulations

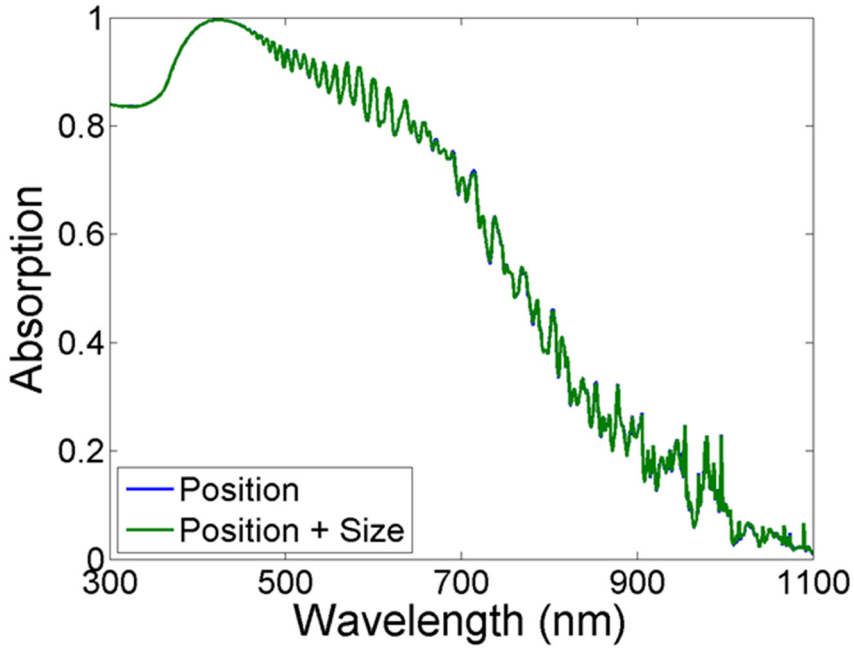

Fig. 6-17 Comparison of absorption spectra between the best pseudo-disordered dual design and the best pseudo-disordered positional design.

In these primarily process of optimization on the sized perturbation, we could realize that it is not easy to make a design with high J_{sc} compared to only the pseudo-disordered positional design. In another aspect, changing size of holes could have a limited effect on the J_{sc} of the pseudo-disordered design, which could give a certain extent help to make the fabrication. In the future, by aid of the guides proposed in the real and reciprocal space, we could try to further optimize the pseudo-disordered structure based on this dual perturbation.

6.7 Conclusion and perspective

We have studied the effect of a pseudo-disordered pattern on the absorption of technologically realistic solar cell stacks including a thin absorbing c-Si layer, a front transparent electrode, and a metallic layer on the back. First, we have shown that the absorption of the pseudo-disordered structure overpasses the absorption of an optimized 2D square lattice of holes structure within a large range of c-Si layer thicknesses. Then, thanks to the metrics used to characterize the pseudo-disorder, we evidence that clustering of holes needs to be avoided to achieve a high J_{sc}. Studying these structures in the reciprocal space, we have also shown that the two criteria separately suggested

in the literature to optimize complex nanopatterns need to be satisfied simultaneously. The redistribution of the spatial frequencies over the whole frequency ranges is another argument against the clustering of holes. Lastly, pseudo-disordered structures lead to a high J_{sc} not only for normal incidence, but also for a large range of angles of incidence. In addition, preliminary pseudo-disordered structures combining shifts and resizing of the holes have been developed in order to further increase the J_{sc}. Only tiny enhancement has been obtained, but these results need further investigations.

Thanks to Nano-Imprint Lithography techniques based on replication of master stamp associated with transfer processes like plasma etching [15], the pseudo-disordered structure proposed in this thesis can be realized using exactly same processes as the optimized square lattice of holes with no additional cost. Using the design rules presented in this chapter together with relevant nanopatterning processes is therefore expected to lead to highly efficient and angularly stable thin film solar cells.

References and links

1. V. Depauw, X. Meng, O. El Daif, G. Gomard, L. Lalouat, E. Drouard, C. Trompoukis, A. Fave, C. Seassal, and I. Gordon, "Micrometer-thin crystalline-silicon solar cells integrating numerically optimized 2-D photonic crystals," Photovoltaics, IEEE Journal of **4**, 215-223 (2014).
2. C. Herzinger, B. Johs, W. McGahan, J. Woollam, and W. Paulson, "Ellipsometric determination of optical constants for silicon and thermally grown silicon dioxide via a multi-sample, multi-wavelength, multi-angle investigation," Journal of Applied Physics **83**, 3323-3336 (1998).
3. E. D. Palik, *Handbook of optical constants of solids* (Academic press, 1998), Vol. 3.
4. A. Bozzola, M. Liscidini, and L. C. Andreani, "Photonic light-trapping versus Lambertian limits in thin film silicon solar cells with 1D and 2D periodic patterns," Optics Express **20**, A224-A244 (2012).
5. X. Meng, V. Depauw, G. Gomard, O. El Daif, C. Trompoukis, E. Drouard, C. Jamois, A. Fave, F. Dross, I. Gordon, and C. Seassal, "Design, fabrication and optical characterization of photonic crystal assisted thin film monocrystalline-silicon solar cells," Optics Express **20**, A465-A475 (2012).
6. R. Peretti, G. Gomard, L. Lalouat, C. Seassal, and E. Drouard, "Absorption control in pseudodisordered photonic-crystal thin films," Physical Review A **88**, 053835 (2013).
7. G. Gomard, R. Peretti, E. Drouard, X. Meng, and C. Seassal, "Photonic crystals and optical mode engineering for thin film photovoltaics," Optics Express **21**, A515-A527 (2013).
8. A. Oskooi, M. De Zoysa, K. Ishizaki, and S. Noda, "Experimental Demonstration of Quasi-resonant Absorption in Silicon Thin Films for Enhanced Solar Light Trapping," ACS Photonics **1**, 304-309 (2014).
9. A. Oskooi, P. A. Favuzzi, Y. Tanaka, H. Shigeta, Y. Kawakami, and S. Noda, "Partially disordered photonic-crystal thin films for enhanced and robust photovoltaics," Applied Physics Letters **100**, 181110 (2012).
10. A. Bozzola, M. Liscidini, and L. C. Andreani, "Broadband light trapping with disordered photonic structures in thin-film silicon solar cells," Progress in Photovoltaics: Research and Applications **22**, 1237-1245 (2014).

11. E. R. Martins, J. Li, Y. Liu, V. Depauw, Z. Chen, J. Zhou, and T. F. Krauss, "Deterministic quasi-random nanostructures for photon control," Nat Commun **4**(2013).
12. X. Fang, M. Lou, H. Bao, and C. Y. Zhao, "Thin films with disordered nanohole patterns for solar radiation absorbers," Journal of Quantitative Spectroscopy and Radiative Transfer (2015).
13. Z. Yu, A. Raman, and S. Fan, "Fundamental limit of light trapping in grating structures," Optics express **18**, A366-A380 (2010).
14. B. C. Sturmberg, K. B. Dossou, L. C. Botten, A. A. Asatryan, C. G. Poulton, R. C. McPhedran, and C. M. de Sterke, "Nanowire array photovoltaics: Radial disorder versus design for optimal efficiency," Applied Physics Letters **101**, 173902 (2012).
15. C. Trompoukis, O. El Daif, V. Depauw, I. Gordon, and J. Poortmans, "Photonic assisted light trapping integrated in ultrathin crystalline silicon solar cells by nanoimprint lithography," Applied Physics Letters **101**, 103901 (2012).

7. Conclusions and perspectives

7.1 Conclusions

In this thesis, we have proposed novel light trapping strategies for thin film crystalline silicon (c-Si) solar cells, based on photonic crystals (PCs). Light trapping structures and realistic PC-assisted solar cells were all investigated numerically and partly experimentally. Two kinds of patterns have been considered: simple square lattices and pseudo-disordered structures. Both enable a substantial increase of the absorption in thin film c-Si solar cells, compared to unpatterned ones. The aims have been to understand the mechanism of the light trapping in these types of the PCs, to identify and investigate the structure that can provide efficient light trapping within realistic configurations and meanwhile propose the method to generate the optimized design.

We first considered square lattice PCs with elementary patterns made of cylindrical holes or inverted nano-pyramids. These patterns were positioned on the top layers of thin film solar cells including an absorbing c-Si layer with a thickness on the micrometer range. The specific absorption in the absorbing layer in the complete solar cells has been considered. By performing the numerical simulations based on FDTD method, the optimized designs were realized and the role of the PC structure could be clearly evidenced and quantified: current densities (J_{sc}) are increased by 56.4% (cylindrical holes) and 104.8% (inverted nano-pyramids) compared to the unpatterned case respectively. Meanwhile, the absorption in each layer in the solar cells has been computed. It appears that the inverted pyramid structure has a better performance than the cylindrical holes structure, which is mainly due to a more robust anti-reflectivity property and a higher light coupling efficiency in the longer wavelength. At last, an additional cylindrical holes structure can be introduced on the bottom of the thin film solar cell, in order to compose a dual cylindrical holes design to increase the absorption in the long wavelength range. This led to an expected J_{sc} of 32.96mA/cm², 2.39mA/cm² higher than the single grating structure in the whole spectrum. These designs have been considered to realize demonstrator devices in the frame of the EU PhotoNvoltaics project.

Second, in order to increase the absorption in a large wavelength range, over that achieved for a fully optimized single periodic structure, a pseudo-disordered structure has been proposed. The general goal is to increase the spectral density of modes of the PCs.

With this numerically optimized pseudo-disordered structure, and considering a 3x3 supercells, the patterns were primarily fabricated in a SOI wafer, in order to highlight the influence of experimental fluctuations related to the process imperfections, and the impact of the illumination conditions on the expected absorption spectra. Then selected pseudo-disordered patterns have been integrated in a thin c-Si film bonded on top of the metal layer. The experimental integrated absorption measured in this solar cell stack almost exhibits the same behavior as the theoretical one, despite a constant offset. Compared to a square lattice of holes, the best pseudo-disordered structure led to an absorption increased up to 2.1%, which is in good agreement with the 2.7% increase expected theoretically.

Thirdly, we have deeply analyzed the influence of the pseudo-disordered structure in different supercells size with several thicknesses of the c-Si layer. Thanks to the metrics introduced to characterize the pseudo-disorder, we evidence that clustering of holes needs to be avoided to achieve a high J_{sc}. Studying these structures in the reciprocal space, we have also shown that the two criteria separately suggested in the literature to optimize complex nanopatterns need to be satisfied simultaneously. The redistribution of the spatial frequencies over the whole frequency ranges is another argument against the clustering of holes. Finally, pseudo-disordered structures lead to a high J_{sc} not only for normal incidence, but also for a large range of angles of incidence.

Lastly, preliminary researches of pseudo-disordered structures based on the perturbation of the size together with the position of the holes have been implemented. Resulting current densities are slightly above the value of the best design with pseudo disorder only in position. However, it could be noted that the proposed design guideline in the real and reciprocal space could help to obtain the designs with even larger J_{sc}.

7.2 Perspectives

In the future, we could take advantage of the Nano-Imprint Lithography techniques [1-3] based on replication of master stamp associated with transfer processes like plasma etching, to fabricate the pseudo-disordered structure proposed in this thesis.

Compared to the optimized square lattice of holes, it can be realized with no additional cost. Using the design rules presented in this work together with a relevant nanopatterning processes is therefore expected to lead to highly efficient and angularly stable thin film solar cells. Moreover, large surface area patterned sample could be measured using integrating sphere to fully take into account the diffracted orders at wavelengths smaller than the period as well as the scattered light. Finally, the deposition the passivation and antireflection layer would allow to determine the electrical performances.

As well, we would like to further develop the pseudo-disordered designs based on different geometric shapes [4], such as inverted nano-pyramid [5], cone, ellipse, and nano-dots [6]. Meanwhile, the perturbation of the pseudo-disordered structure could be introduced with one or several factor(s), including the size and position [7], as well as the symmetry of the patterned element [8-10]. Furthermore, it could be interesting to compare pseudo-disordered design with the optimized square lattice with different geometric shapes, for instance, the best pseudo-disordered holes structure and the optimized square lattice of the inverted pyramid structure. Unfortunately, the two design were used with different stacks in the thesis, so it not easy to tell which one has a better performance. In the square lattice, the inverted nano-pyramids structure has a better anti-reflection effect and relative higher absorption in large wavelength range than the nano-holes element. However, as shown in the thesis, the optimized design with inverted nano-pyramid has a quite large period, so it could be hard to have highly disordered positional design. The pseudo-disordered pyramid based on the size or the broken symmetry of the shape could be another choice to enhance its performance. Indeed, the cost of designs based on the pseudo-disorder and square lattice has a quite limited difference by aid of the NIL techniques, and it means that only a high performance design will be welcomed without considering the order or disorder. In the future, the seeking for the high J_{sc} of design will be performed with several geometric shapes.

Furthermore, based on this advanced pseudo-disorder light trapping scheme, we could adopt it to other PV devices in order to have a high efficiency, e.g. the organic and perovskite thin film solar cells. The pseudo-disorder could only in the antireflection layer, or the passivation and active layers, depending on the properties of the solar cells. In another point of view, the LEDs [11, 12]also could profit this scheme to provide a wide and high efficient illumination.

References and links

1. W. Zhou, *Nanoimprint Lithography: An Enabling Process for Nanofabrication: An Enabling Process for Nanofabrication* (Springer Science & Business Media, 2013).
2. C. Trompoukis, O. El Daif, V. Depauw, I. Gordon, and J. Poortmans, "Photonic assisted light trapping integrated in ultrathin crystalline silicon solar cells by nanoimprint lithography," Applied Physics Letters **101**, 103901 (2012).
3. J. Xavier, J. Probst, F. Back, P. Wyss, D. Eisenhauer, B. Löchel, E. Rudigier-Voigt, and C. Becker, "Quasicrystalline-structured light harvesting nanophotonic silicon films on nanoimprinted glass for ultra-thin photovoltaics," Optical Materials Express **4**, 2290-2299 (2014).
4. J. Gjessing, A. S. Sudbø, and E. S. Marstein, "Comparison of periodic light-trapping structures in thin crystalline silicon solar cells," Journal of Applied Physics **110**, 033104 (2011).
5. J. Muller, A. Herman, A. Mayer, and O. Deparis, "A fair comparison between ultrathin crystalline-silicon solar cells with either periodic or correlated disorder inverted pyramid textures," Optics express **23**, A657-A670 (2015).
6. E. R. Martins, J. Li, Y. Liu, V. Depauw, Z. Chen, J. Zhou, and T. F. Krauss, "Deterministic quasi-random nanostructures for photon control," Nat Commun **4**(2013).
7. F. Pratesi, M. Burresi, F. Riboli, K. Vynck, and D. S. Wiersma, "Disordered photonic structures for light harvesting in solar cells," Optics Express **21**, A460-A468 (2013).
8. T. Cai and S. E. Han, "Effect of symmetry in periodic nanostructures on light trapping in thin film solar cells," JOSA B **32**, 2264-2270 (2015).
9. Z. Xia, X. Qin, Y. Wu, Y. Pan, J. Zhou, and Z. Zhang, "Efficient broadband light absorption in elliptical nanohole arrays for photovoltaic application," Optics letters **40**, 5814-5817 (2015).
10. Y. Wu, Z. Xia, Z. Liang, J. Zhou, H. Jiao, H. Cao, and X. Qin, "Broadband absorption enhancement in elliptical silicon nanowire arrays for photovoltaic applications," Optics express **22**, A1292-A1302 (2014).
11. A. F. Koenderink, A. Alù, and A. Polman, "Nanophotonics: Shrinking light-based technology," Science **348**, 516-521 (2015).

12. S. Noda and M. Fujita, "Light-emitting diodes: Photonic crystal efficiency boost," Nature photonics **3**, 129-130 (2009).

Annex

Annex. 1

The refractive indices and extinction coefficients used in the optical simulations and corresponding to a-Si[1], ZnO [2], c-Si (two types, which are name “c-Si_EPI” and “c-Si_Herzinger”)[1], Al [2], ITO [2] and SiO_2 [2], which are from experimental data provided by IMEC.

In chapter 4, for the simulation of the c-Si substrate case (ITO/a-Si:H/c-Si[1]/c-Si[2]) with the inverted pyramid and cylindrical holes structures, the absorbing layer (c-Si[1]) uses the c-Si index: “c-Si_EPI” and the substrate layer uses the c-Si index “c-Si_Herzinger”. In the metal-based case (ITO/a-Si:H/c-Si/BSF/ITO/Al) with the inverted pyramid and cylindrical holes structures , the c-Si uses the index “c-Si_Herzinger”. In the metal-based case (ITO/a-Si:H/c-Si/BSF/ZnO/Al), the c-Si uses the index “c-Si_EPI”.

In chapter 5 and 6, for all the simulation with the pseudo-disordered structure, the c-Si uses the index “c-Si_Herzinger”.

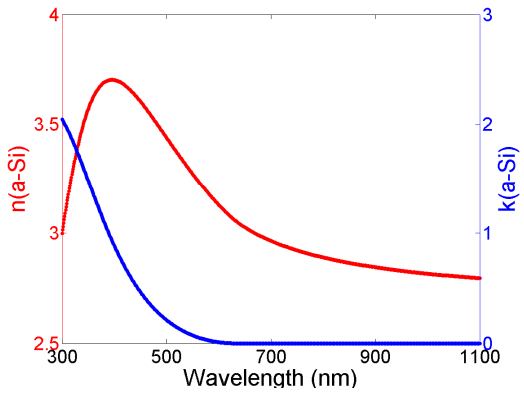

c-Si_EPI

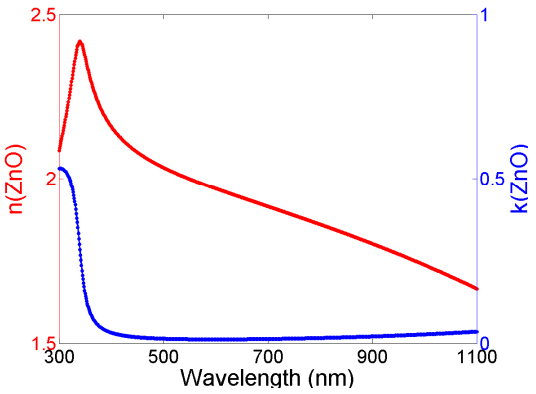

c-Si_Herzinger

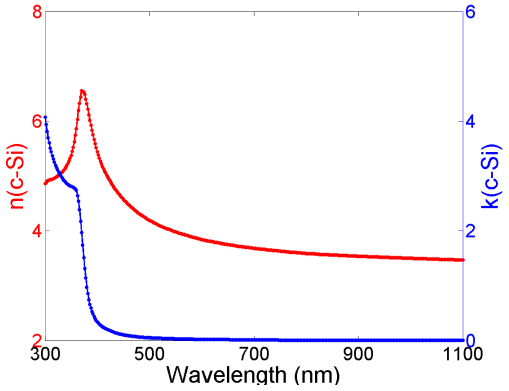
n(c-Si)
k(c-Si)
Wavelength (nm)

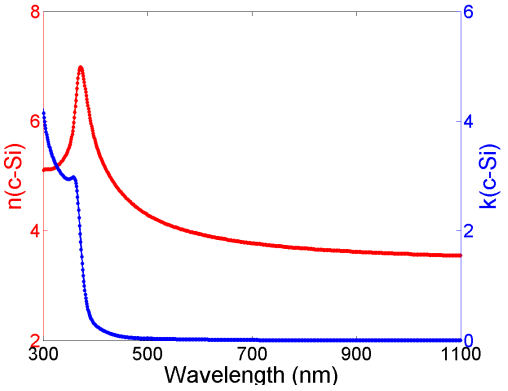
n(c-Si)
k(c-Si)
Wavelength (nm)

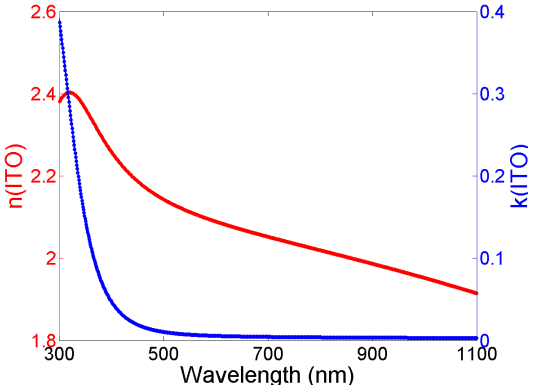
n(ITO)
k(ITO)
Wavelength (nm)

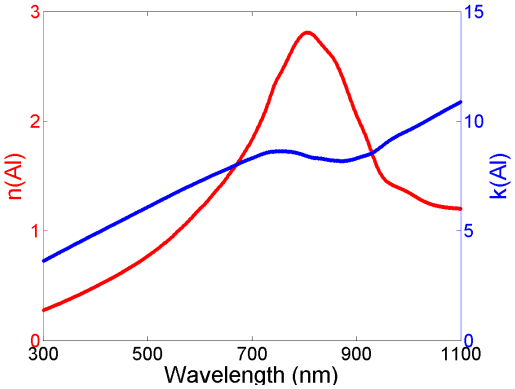
n(Al)
k(Al)
Wavelength (nm)

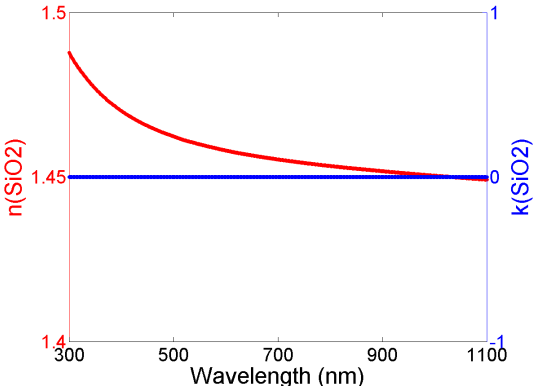
n(SiO2)
k(SiO2)
Wavelength (nm)

Annex. 2

This script is used to calculate the generate rate (G) as:

$$G = \frac{-0.5\left|E\right|^2 imag(\varepsilon)}{\hbar}$$

In order to calculate the generate rate in the numerical simulation with Lumerical software, we need to know the electric field intensity (E) and the imaginary of the permittivity (ε). It could be measured by the following script, which is the 2D photonic crystal structure design in the 3D simulation:

```
################################################
# Generation Rate
# This script calculates generate from the formula
# G = -0.5 *|E|^2 * imag(eps)/ hbar
# Output properties:
# unit m-3s-1
################################################
load("xxxxx.fsp");
namemat = "xxxx.mat";
# get raw data from monitors
x=getdata("field","x");
y=getdata("field","y");
z=getdata("field","z");
f=getdata("field","f");
nx=size(x);nx=nx(1,1);#nx=(nx(1,1)+1)/2; # due to the symmetry and anti-symmetry boundary setting
ny=size(y);ny=ny(1,1);#ny=(ny(1,1)+1)/2;
nz=size(z);nz=nz(1,1);
nf=size(f);nf=nf(1,1);
E2_matrix=getelectric("field");
if (havedata("index","index_x")) {
n_matrix=getdata("index","index_x");
} else {
n_matrix=getdata("index","index_z");
}
epsilon = eps0*n_matrix^2;
#######filter#########################################
# create filter for cSi and integrate over the area
filter=matrix(nx,ny,nz,nf);
for(i=1:nf) {
filter(1:nx,1:ny,1:nz,i) =
imag(eps0*n_matrix(1:nx,1:ny,1:nz,i)^2)*(real(n_matrix(1:nx,1:ny,1:nz,i))==real(n_matrix(nx/5,ny/5,
nz/3,i)));
}
################################################
##load the file amg1.5#############################
amg15=readdata("amg15.txt");
amg15_size = size(amg15);
am_lambda_old=matrix(1,amg15_size(1,1));
am_e=matrix(1,amg15_size(1,1)); #vaule of the AM1.5
for(i=1:amg15_size(1,1)){ #get the lambda and the value of the spectrum
am_lambda_old(i)=amg15(i,1);
am_e(i)=amg15(i,3);
}
```

```
lam_nm = c/f*1e9; # wavelength (1 nm)
lambda_step=lam_nm(2,1)-lam_nm(1,1); #step wavelength (nm)
am_new=interp(am_e,am_lambda_old,lam_nm);
amg15_even=matrix(1,nf);
amg15_even(1,1)=am_new(1,1); #the first equal vaule did not change
for(i=2:nf)
{
amg15_even(i)=(am_new(i)+am_new(i-1))/2; #average vaule
}
############################################################
norma = meshgrid4d(4,x,y,z,amg15_even);
SI=meshgrid4d(4,x,y,z,sourceintensity(f));
G_matrix_polychromatic= 0.5*E2_matrix*filter/hbar/SI*norma;
G_integrated_polychromatic=matrix(nx,ny,nz);
G_integrated_polychromatic=integrate(G_matrix_polychromatic,4,lam_nm);
############################################################
wavelength = lam_nm;
matlabsave(namemat,wavelength,x,y,z,nx,ny,nz,nf,G_integrated_polychromatic);
exit(2);
```

Annex. 3

All the considered limits are under the hypothesis of no reflection at the front interface, and a perfect reflection at the bottom interface of the active layer.

In a simple thin film under normal incidence, the double pass absorption derives from:

$$A = 1 - \exp(-2\alpha d)$$

The Lambertian scattering limit [3, 4] basically supposes a Lambertian scattering at front interface, which can be calculated by

$$A = 1 - \frac{1}{\pi} \iint_{\substack{0<\theta<\frac{\pi}{2} \\ 0<\varphi<2\pi}} cos\theta sin\theta \exp\left(-\frac{2\alpha d}{cos\theta}\right) d\theta d\varphi$$

Finally, the Yablonovitch limit [5] can be regarded as:

$$A = \frac{\alpha d}{\alpha d + \frac{1}{4n^2}}$$

Where $\alpha(\lambda)$ is the spectrally resolved absorption coefficient given by $\alpha(\lambda) = 4\pi\kappa(\lambda)/\lambda$, n (λ) and κ (λ) are the real and imaginary part of the refractive index of absorbing material respectively, and d is the thickness of the absorbing layer.

Precisely, the Lambertian scattering limit is the maximum light path enhancement by considering the scattering only of the incoming light at the surface of the solar cells. Due to the perfect back reflector on the bottom, one round-trip reflection is taken into considered. Compared to the double pass scheme, the Lambertian scattering limit could highly enhance the absorption by randomizing the incoming light.

Furthermore, the Yablonovitch limit represents the absorption enhancement with a full scattering surface and a perfect back mirror, i.e. by taking into account a light trapping effect thank to partial back scattering of the light at the front interface after round trips in the layer. However, it is only applicable for the low κ-index of the absorbing medium and it does not takes into account any interference effect in the film.

References and links

1. C. Herzinger, B. Johs, W. McGahan, J. Woollam, and W. Paulson, "Ellipsometric determination of optical constants for silicon and thermally grown silicon dioxide via a multi-sample, multi-wavelength, multi-angle investigation," Journal of Applied Physics **83**, 3323-3336 (1998).
2. E. D. Palik, *Handbook of optical constants of solids* (Academic press, 1998), Vol. 3.
3. A. Bozzola, M. Liscidini, and L. C. Andreani, "Photonic light-trapping versus Lambertian limits in thin film silicon solar cells with 1D and 2D periodic patterns," Optics Express **20**, A224-A244 (2012).
4. L. Andreani, A. Bozzola, P. Kowalczewski, and M. Liscidini, "Towards the lambertian limit in thin film silicon solar cells with photonic structures," in *27th European Photovoltaic Solar Energy Conference and Exhibition: Material Studies, New Concepts and Ultra-High Efficiency Fundamental Material Studies*, 2012),
5. T. Tiedje, E. Yablonovitch, G. D. Cody, and B. G. Brooks, "Limiting efficiency of silicon solar cells," Electron Devices, IEEE Transactions on **31**, 711-716 (1984).

Abstract

In thin film silicon solar cells, it is important to take control of the absorption efficiency, in order to reach a high enough short-circuit current density (J_{sc}). To reach this goal, we have developed light trapping strategies based on simply periodic photonic crystals (PC) and more complex pattern structures. This work aims at integrating such structures into thin film crystalline silicon (c-Si) solar cells.

Firstly, a simply periodic square lattice PC structure of cylindrical holes or inverted nano-pyramids have been considered in a-Si:H/c-Si heterojunction thin film solar cells. The absorption in the sole absorbing layer (c-Si) is considered and optimized in numerical simulations based on the Finite Difference Time Domain method. The J_{sc} are increased by 56.4% (cylindrical holes) and 104.8% (inverted nano-pyramids) compared to the unpatterned case. We also considered more advanced structures where an additional cylindrical holes structure is introduced in the bottom.

Secondly, we have considered complex but realistic "pseudo-disordered" nanostructures, based on periodically reproduced supercells where the holes are randomly shifted. In such structures the absorption could be increased compared with fully optimized square lattice of holes, by increasing the spectral density of optical modes. Simulation based on Rigorous Coupled Wave Analysis and fabrication by electronic beam lithography and reactive ion etching technologies have been performed, leading to a net absorption increase of about 2.1% theoretically, and 2.7% experimentally.

Lastly, we have introduced pseudo-disordered structures with supercells of different size, in c-Si layers of several thicknesses in the 1-8µm range. The absorption mechanisms in such structures were analyzed, both in the real and reciprocal spaces, with a view to determine design guidelines. Moreover, the angular response of the optimized pseudo-disordered structure appears to be more stable than in the optimized square lattice of holes periodic case, especially in the long wavelength range.

Keyword: Photovoltaic, thin films, silicon, photonic crystals, disorder, light trapping

RESUME FRANCAIS :

Photovoltaïques cellules solaires en couches minces avancées à cristaux photoniques : de l'ordre au pseudo- désordre

Présentée devant
Ecole Centrale de Lyon

Spécialité: Photonique

Pour obtenir
Le grade de docteur

École doctorale : Electronique, Electrotechnique et Automatisme de Lyon

Par

He DING

Laboratoire de recherche: Institut des Nanotechnologies de Lyon (INL) – CNRS UMR 5270

1. Introduction

L'énergie est l'essence de toute activité humaine [1]. Les sources d'énergie traditionnelles, comme le charbon, le pétrole et le gaz, jouent un rôle important et forment aujourd'hui les sources d'énergie dominantes. Comme ces combustibles fossiles ont un impact négatif sur l'environnement, les énergies renouvelables (hydroélectricité, énergie éolienne, énergie solaire) sont appelées à devenir importantes dans notre vie quotidienne.

Les cellules solaires photovoltaïques (PV) classiques sont constituées de matériaux semi-conducteurs qui absorbent les photons de la lumière solaire et les convertissent en électricité [2, 3]. Au cours de la dernière décennie, grâce à de nouvelles technologies, aux économies d'échelle, l'industrie photovoltaïque est en plein essor avec des taux de croissance bien au-delà de 30% par an et le coût est réduit en permanence d'environ 19,6% à chaque fois que la production cumulée double [4, 5]. En dépit de la vitesse de croissance élevée et de la baisse des prix, le PV est encore dépendant de subventions sur les principaux marchés du monde, et est fortement affectée par les politiques gouvernementales. Afin de développer davantage le marché de PV, et d'attirer davantage d'entreprises, les coûts devraient être encore réduits, et les cellules solaires efficacités améliorées, afin d'atteindre ou même de dépasser la parité réseau [6, 7].

Pour réussir, de nombreuses solutions basées sur différents matériaux et différentes technologies sont proposées, qui sont divisés en trois générations [6]. Parmi ces trois générations, la plupart des cellules solaires actuellement sur le marché sont de première génération, en plaquettes de silicium, et cette domination devrait se poursuivre dans l'avenir. En effet, le silicium est non-toxique et disponible en abondance dans la croûte terrestre, et le silicium cristallin (c-Si) des modules PV a montré sa stabilité à long terme dans la pratique [8]. Cependant, les plaquettes sont rigides et l'énergie nécessaire pour les produire n'est pas négligeable. En outre, le coût d'un module PV en c-Si est clairement dominé par le coût des matériaux, en particulier celui de la tranche de silicium. Dans ce contexte, les cellules solaires en couches minces, également considérées comme des dispositifs de deuxième génération, offrent des avantages substantiels puisque le coût matière est réduit. Ces cellules solaires à couches minces pourraient être faites d'une large gamme de matériaux, y compris le silicium, mais aussi d'autres matériaux comme, par exemple, le cuivre indium gallium séléniure (CIGS).

Ces matériaux conduisent à des gains d'efficacité par rapport à ceux de silicium multi-cristallin en laboratoire [4]. Dans ces cellules solaires de seconde génération, l'efficacité de conversion reste limitée par l'absorption dans des couches aussi minces que quelques centaines de nanomètres à quelques micromètres. Par conséquent, il apparaît nécessaire de surmonter cette limitation pour atteindre des rendements acceptables. Enfin, la troisième génération de cellules solaires vise à des dispositifs avec des rendements généralement supérieurs à la limite de Shockley-Queisser pour une cellule solaire à jonction unique [9]. Ils utilisent des concepts avancés, dont les cellules tandem. Cependant, l'incorporation de nouveaux concepts a encore besoin de la recherche à long terme et de développements pour être disponible pour les applications grand public. Notre objectif raisonnable à court terme est d'obtenir un rendement de conversion élevé dans les cellules solaires à couches minces, en améliorant l'absorption.

Dans cette thèse, nous proposons de mettre en œuvre et d'optimiser des structures de nanophotonique avancée pour effectuer un piégeage de la lumière efficace dans les cellules solaires à couches minces. De 2008 à 2012, l'intérêt des CP a été étudié à l'INL et dans d'autres instituts. Ce fut le principal sujet de deux étudiants de doctorat à l'INL, Guillaume Gomard et Xianqin Meng. Durant ma thèse, 2012-2015, j'ai continué de développer cette approche, y compris les structures pseudo-désordonnées, pour améliorer l'absorption des cellules solaires en couches minces de c-Si.

Parmi les différentes natures de silicium dans les cellules solaires PV, nous prenons en compte le c-Si monocristallin en tant que matériau absorbant principalement en raison de sa bonne qualité. Les inconvénients des autres siliciums, par exemple, les recombinaisons élevées du silicium amorphe hydrogéné a-Si :H ou encore du poly-Si limites les épaisseurs et donc leur potentiel. Compte tenu des contraintes du domaine de PV, nous allons utiliser une hétérojonction de film mince à base de technologie "epifree" recouverte par une couche extrême mince de a-Si: H.

J'ai contribué à l'intégration de CP dans les cellules solaires c-Si en couches minces, en collaboration avec l'IMEC, LPICM et LPN. Dans ce contexte, mon rôle était de réaliser des simulations optiques pour concevoir et optimiser les cellules solaires en couches minces en intégrant des motifs réguliers, puis à optimiser les modèles pseudo-désordonnés. J'ai également contribué à la fabrication de ces motifs dans des couches minces de c-Si, afin d'étudier expérimentalement les effets de piégeage de la lumière.

Dans ce manuscrit, nous présentons d'abord les cellules solaires photovoltaïques, puis donnons ensuite une brève revue des stratégies de piégeage de la lumière dans le

chapitre 2. Nous décrivons les méthodes utilisées pour effectuer des simulations et des expériences numériques, au chapitre 3. Puis dans le chapitre 4, nous nous concentrons sur l'absorption nette de la couche absorbante dans les cellules complètes solaires à couches minces, dans lequel les couches supérieures et actives sont structurées avec deux types de CP réguliers différents, soit des pyramides inversées soit des trous cylindriques. Les simulations optiques révèlent que les motifs dans la couche active (c-Si) permettent d'augmenter sensiblement son absorption intégrée dans une gamme de 300-1100 nm par rapport à l'empilement sans motif. En outre, le potentiel d'un réseau de diffraction en face arrière pour améliorer encore le piégeage de lumière est évalué pour la même configuration réaliste. Dans le chapitre 5, afin d'augmenter encore l'absorption tout en maintenant le coût et la faisabilité de la conception, les structures du CP pseudo-désordonnées sont proposées. La comparaison de l'absorption totale de la cellule solaire entre la structure pseudo-désordonnée et le réseau de trous carrés optimisé sera étudiée. Après cela, ces dessins à motifs sont fabriqués sur un silicium sur isolant (SOI), et sur les couches c-Si plus réalistes collées sur une surface métallique. Les expériences sont réalisées sur des échantillons pour évaluer leur performance optique. Dans le chapitre 6, nous discutons des propriétés des modèles pseudo-désordonnés en utilisant la simulation numérique, afin de donner des règles et des critères de conception clés pour atteindre la plus haute augmentation de l'absorption nette dans les cellules solaires.

2. Les cellules solaires et le piégeage de la lumière

Dans ce chapitre, nous avons d'abord introduit le principe de fonctionnement de cellules solaires. Ici, nous présentons les mécanismes de piégeage de la lumière dans les cellules solaires, avec une attention particulière pour les structures à l'échelle de la longueur d'onde de la lumière. Le but ultime est de faire une couche absorbante aussi mince que possible tout en conservant de bonnes performances d'absorption.

L'épaisseur du film varie de quelques nanomètres (nm) à des dizaines de micromètres (µm). Ceci permet aux cellules en couches minces d'offrir de nombreux avantages, tels que leur faible coût, de la souplesse et une tension potentiellement améliorée. Le chemin optique des photons dans la couche mince doit être suffisamment long pour permettre une absorption de la lumière solaire efficace, en particulier dans les gammes infrarouge et rouge. Par conséquent, afin d'obtenir un courant élevé, les systèmes de piégeage de la lumière doivent être considérés.

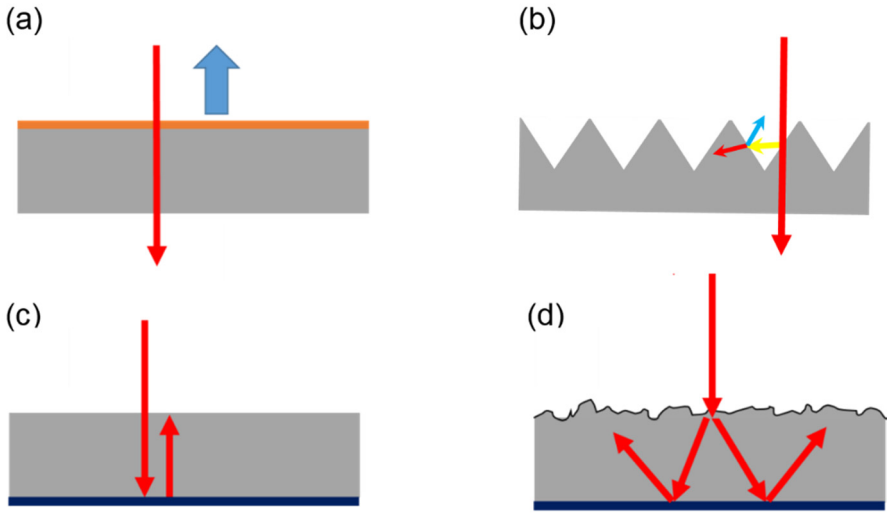

Figure 2-1. Régimes conventionnels pour la réduction des pertes optiques avec l'anti-réflecteur (a), texturations de surface (b), le miroir arrière (c) et les textures de diffusion aléatoires idéales (d) appliqués à la couche simple.

Les moyens classiques pour la réduction des pertes optiques se concentrent principalement sur les cellules solaires de première génération. Ils utilisent des revêtements antireflet (AR) (Fig. 2-1a) et des texturations de surface (Fig. 2-1b). Nous pourrions aussi ajouter simplement un miroir à l'arrière de la couche absorbante (Fig. 2-1a), qui double la longueur du trajet de la lumière. En outre, Yablonovith a proposé

une limite fondamentale au piégeage de la lumière, avec une surface de diffusion idéale appelée « surface Lambertienne » [10, 11].

Au cours des dix dernières années, un large éventail de schémas a été proposé, et leur intégration dans les cellules solaires à couches minces a été largement étudiée. Nous allons examiné des nano/micro motifs, avec les dimensions géométriques, tels que le paramètre de maille dans le cas d'une structure périodique, de l'ordre de la longueur d'onde de la lumière incidente. L'optique géométrique est donc inappropriée pour décrire le comportement de ces structures. Inversement, elles peuvent tirer profit de la nature ondulatoire de la lumière, et leur comportement peut dépendre fortement de sa longueur d'onde et de l'angle d'incidence.

Il y a une grande variété de structures de piégeage de la lumière, y compris les nano-fils [12, 13], des réseaux diélectriques [14-17], les structures plasmoniques [18-20] et les CP diélectriques [21-25]. Parmi ces structures, les CP présentent un large éventail de modes et résonances optiques, avec de nombreux paramètres réglables. En outre, ils ne conduisent pas à des pertes d'absorption dans les nanostructures métalliques. Pour ces raisons, nous avons choisi de faire usage de ces structures, et de les intégrer dans les cellules solaires à couches minces.

Les CP sont des structures optiques, où l'indice de réfraction présente une modulation périodique avec une constante de réseau de l'ordre de la longueur d'onde de fonctionnement [26]. Cette propriété permet de contrôler une propagation de la lumière de façon non conventionnelle. Bien que la structure du CP puisse être 1D, 2D ou 3D, nous considérons principalement les CP 2D fabriqués en couches minces dans ce travail. Tandis que la plus grande partie des articles publiés à ce jour concernent des structures intégrées dans une seule couche absorbante, notre objectif sera d'examiner l'ensemble de l'empilement, y compris électrodes avant et arrière, et couches dopées. Nous allons notamment tenir compte de l'effet de nano-trous ou nanopyramids périodiques sur l'absorption dans la seule couche absorbante intrinsèque. Cela conduira à une évaluation juste du gain attendu des nanostructures photoniques (voir chapitre 4).

Jusqu'à ce point, nous avons considéré les architectures de cellules solaires avec des motifs de lumière de piégeage simplement périodiques, conduisant à une augmentation de l'absorption par rapport au cas sans motif. Toutefois, l'amélioration de l'absorption globale obtenue est encore loin des limites. Par conséquent, les cellules solaires à couches minces devraient être développées en utilisant des modèles plus complexes [27-30]. Les deux principaux objectifs sont : (1) faire usage de plusieurs

modes par unité de longueur d'onde et (2) permettre à ces modes d'absorber plus de lumière [31, 32].

Les structures pseudo-désordonnées sont difficiles à optimiser pour maximiser l'absorption intégrée, en raison du très grand nombre de configurations possibles. Dans cette thèse, nous allons notamment (1) comparer les structures pseudo-désordonnées avec des motifs simples périodiques optimisés, (2) examiner le cas d'une couche absorbante recouverte d'une couche antireflet et collé sur une couche de réflecteur arri ère, et (3) d'étudier la cas des différentes épaisseurs de c-Si des couches absorbantes des cellules solaires.

3. Simulation, fabrication et de caractérisation des méthodes de cristal photonique assistée cellules solaires en couches minces

Dans ce chapitre, nous allons présenter les méthodologies de simulation numérique et les procédés de fabrication des cellules solaires à couches minces et CP. Les méthodes de caractérisation utilisées pour évaluer les propriétés des structures fabriquées seront également présentés.

Des simulations numériques basées sur la résolution des équations de Maxwell sont des méthodes efficaces pour concevoir et optimiser la géométrie de la cellule solaire et donc de maximiser son courant de court-circuit donc son efficacité. Parmi les nombreuses méthodes, la méthode des différences finies dans le domaine temporel (FDTD) [21, 33] et la méthode « Rigorous Coupled Wave Analysis » (RCWA) [34, 35] dans le domaine fréquentiel, sont utilisées dans cette thèse, selon les fonctionnalités disponibles.

La plupart des empilements sont basés sur des couches de c-Si fabriquées par le groupe IMEC PV, en utilisant le procédé « epi-free » [36, 37]. La structuration des structures complexes ciblées est réalisée par lithographie par faisceau d'électrons, ce qui est assez souple, et la gravure ionique réactive. Ensuite, nous observons la topographie de l'échantillon fabriqué pour vérifier sa qualité, pour la comparaison entre les paramètres optimisée numériquement, et de la géométrie vraiment réalisée, par microscopie électronique à balayage (MEB) et microscopie à force atomique (AFM). L'étape suivante est d'évaluer la qualité optique de l'échantillon fabriqué, nous aurons recours à un banc de micro-réflectivité mis au point à l'INL.

4. Optimisation numérique de la structure à cristal photonique assistée de cellule solaire en couches minces

Dans ce chapitre, nous allons étudier numériquement l'influence de différents types de CP dans le c-Si mince (moins de 2 um d'épaisseur) des cellules solaires, ainsi que l'optimisation correspondante de l'absorption. Nous nous concentrons sur des réseaux de trous cylindriques et de pyramides inversées. Les comparaisons des spectres d'absorption entre les différentes structures seront analysés. Les cartogrpahies de taux de génération de paires électrons/trous correspondantes sont calculés afin d'effectuer les simulations électriques. Le CP a été tout d'abord sur le substrat de silicium, puis sur une couche reportée sur un réflecteur métallique. Enfin, un double réseau de trous cylindriques, face avant et face arrière, est proposé afin d'augmenter encore l'absorption des cellules solaires, en particulier aux grandes longueurs d'onde.

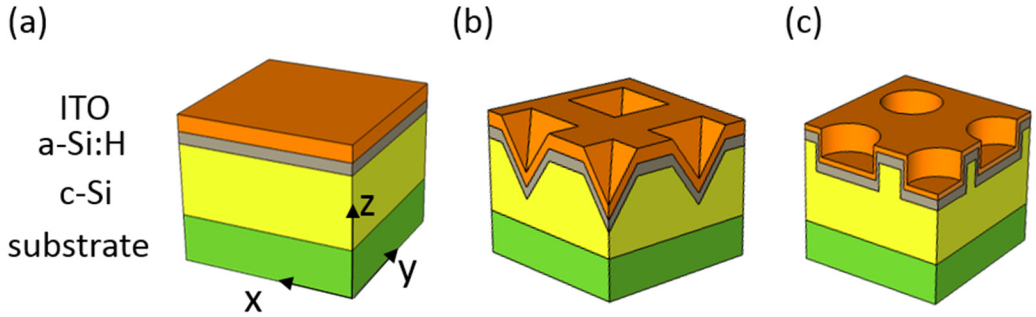

Figure. 4-1 Schéma des cellules solaires avec la structure (a) de pyramides inversées (b) ou de trous cylindriques (c) appliquée sur les couches supérieures, y compris la couche active.

Les cellules solaires en couche mince considéré à hétérojonction silicium typiquement consistent, de haut en bas, en une électrode ITO avant, une couche de a-Si:H , puis une couche de c-Si faiblement dopée sur un substrat c-Si fortement dopé, tel que décrit sur la figure 4-1a. Les CP sont introduits sur les couches supérieures des cellules solaires comme le montre la Fig. 4-1b et 4-1c, y compris la couche de c-Si actif. Afin de permettre une passivation de surface plus facile, la couche de a-Si:H est censée

être déposée après la gravure et donc continue. Dans les études préliminaires, les couches minces sont considérées comme illimitées, sans contact métallique arrière et r éflecteur.

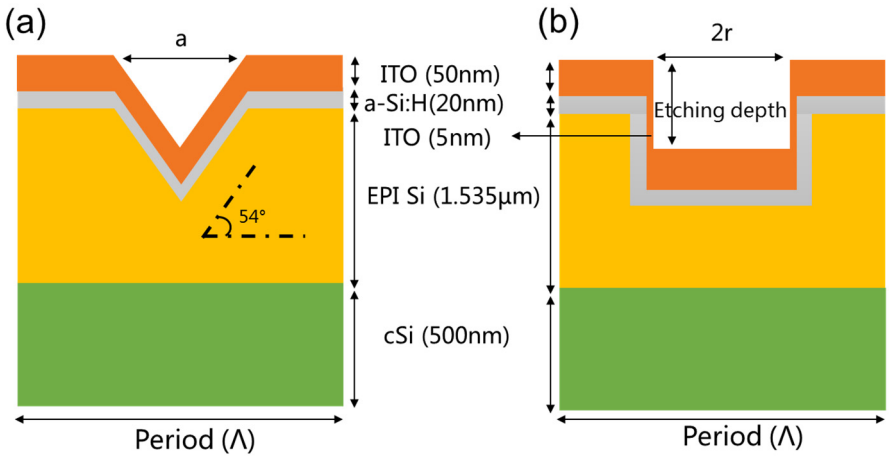

Figure 4-2. Schéma de l'empilement silicium substrat avec structure pyramides inversées (a) et trous cylindriques (b).

Dans la simulation numérique, nous allons considéré les paramètres de la structure de l'ordinateur (Fig. 2.4), la période (Λ), le facteur de remplissage en air (*ff*, par a^2 / Λ^2 pour les pyramides ou $\pi r^2 / L^2$ pour la trous cylindriques, a (r) étant la longueur (rayon) du trou d'air) et la profondeur de gravure (uniquement dans le cas de la structure des trous cylindriques, puisque pour la structure des pyramides ce paramètre est réglé par l'angle de 54,7 ° de la gravure humide du c-Si). Par souci de simplicité, nous nous limitons à trois périodes différentes (300 nm, 450 nm et 600 nm) pour effectuer l'optimisation pour les deux pyramides inversées et des trous cylindriques modèles. Ensuite, nous avons réglé les autres paramètres, c'est-à-dire *ff* et la profondeur de gravure, pour trouver la plus grande efficacité avec les deux types de structures pour chaque période.

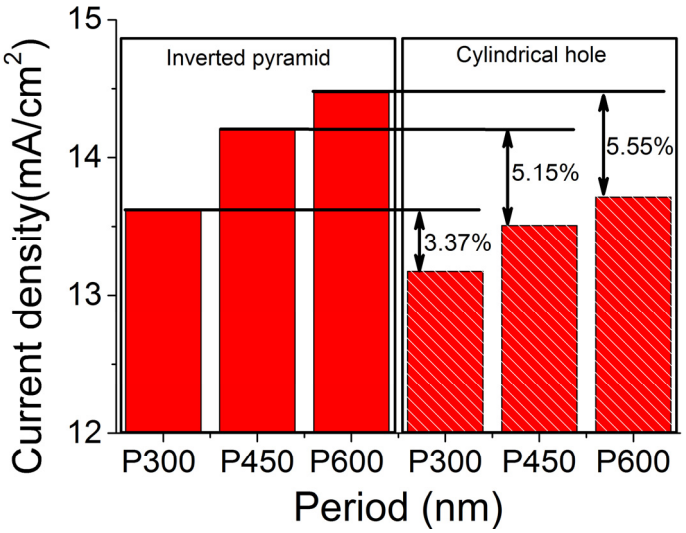

Figure 4-3. La comparaison de la meilleure densité de courant (Jsc, mA / cm²) pour chaque période (300, 450 et 600 nm) avec des motifs de la structure : pyramides inversées et trous cylindriques.

Le J_{sc} maximal réalisable indique directement le rendement des cellules solaires en couches minces avec différentes périodes pour des motifs à la fois le pyramidales et cylindriques ; ils sont résumés dans la Fig. 4-3. Tout d'abord, pour les deux CP, la configuration optimale, de plus grande période conduit au meilleur J_{sc}. En second lieu, on peut voir que le J_{sc} des pyramides inversées est supérieure à celle de la structure des trous cylindriques correspondant.

Dans la suite, nous allons étudier des cellules solaires en couche mince avec empilement complet et face arrière métallique à la place du substrat de silicium. Nous ajoutons un espaceur optique [38-40] entre le zone fortement dopée en face arrière (BSF) et le contact métallique arrière comme illustré sur la Fig. 4-3, afin de réduire l'absorption parasite dans le métal. Les motifs sont toujours les pyramides inversées (Fig. 4-3a et c) et les trous cylindriques (Fig. 4-3b et d).

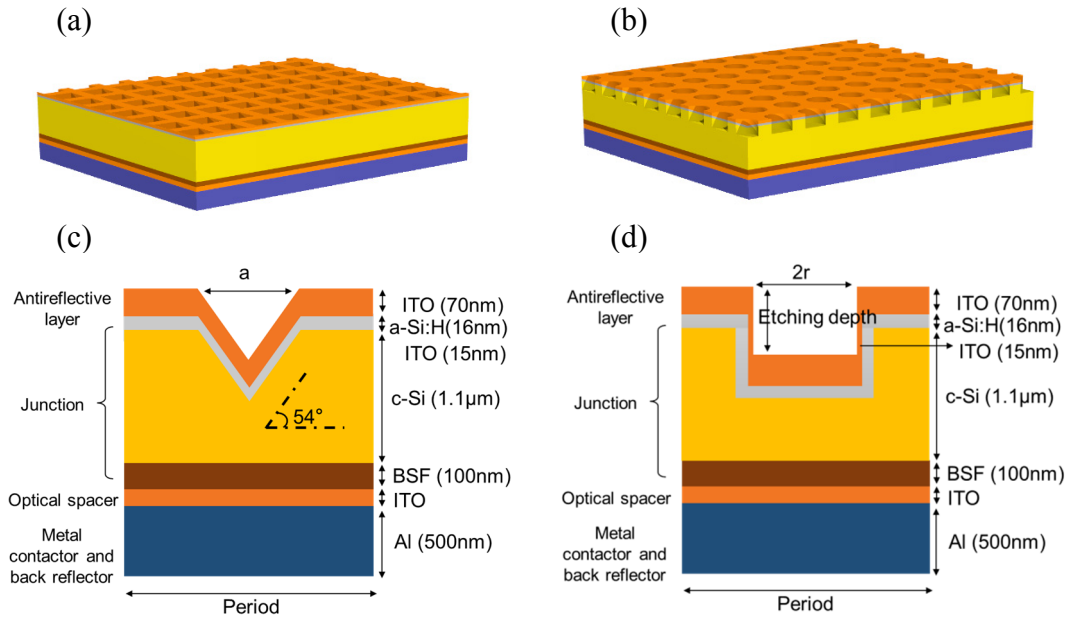

Figure 4-4. Schéma des pyramides inversées (a, croix section verticale c) et les trous cylindriques (b, croix section verticale d) structures.

Le processus d'optimisation est effectué de même sur la structure de pyramides inversées ou de trous du CP. Une telle méthode "manuelle" a été préférée à un algorithme d'optimisation plus "aveugle" comme un algorithme génétique ou l'optimisation par essaim de particules. Le J_{sc} optimisé avec la structure de trous cylindriques du CP est 18,02 mA / cm², avec une période de 580 nm, un *ff* de 0,29, une profondeur de gravure de 110nm et une épaisseur d'espaceur optique de 100nm. La structure des pyramides inversées optimisée fournira un J_{sc} de 23,59mA/cm², avec une période de 800 nm, un *ff* de 0,85 et une épaisseur d'espaceur optique de 110 nm. Par rapport à la conception sans motif (11,52mA/cm²), toutes les nanostructures donnent un plus grand J_{sc}, les trous cylindriques avec une augmentation relative de 56,4% et les pyramides inversées une augmentation relative de 104,8% (Fig. 4-10).

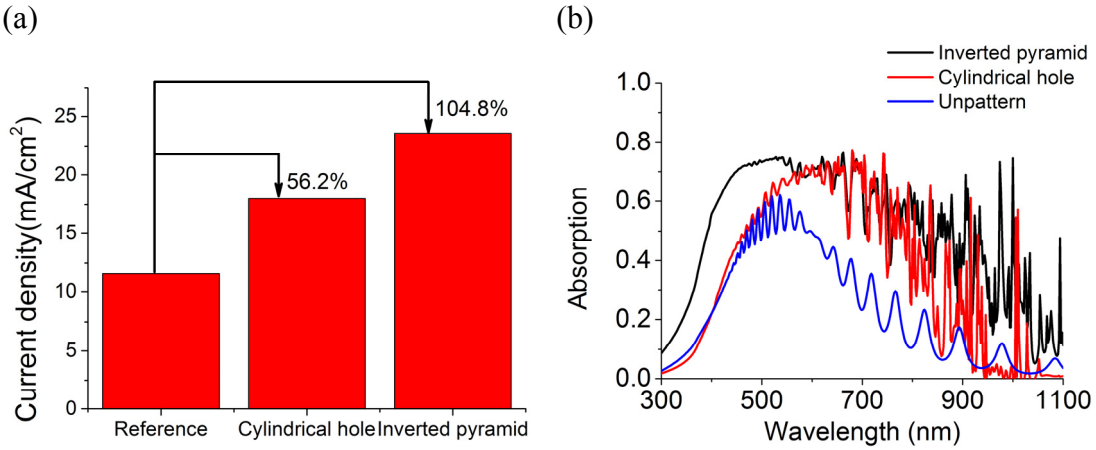

Figure 4-5. (a) La comparaison de la densité de courant (J_{sc}) des pyramides optimisés inversées, des trous cylindriques et la structure sans motif (b) La comparaison des spectres d'absorption entre les pyramides inversées, des trous cylindriques et la structure sans motif dans le mince film solaire complelte cellules.

Afin d'analyser en profondeur l'augmentation de J_{sc} grâce au CP, nous allons nous concentrer sur les spectres d'absorption de la couche de c-Si dans les structures optimisées des deux CP différents et de la référence sans motif. De les spectres d'absorption des deux structures à CP et la structure de référence sans motif représenté sur la Fig. 4-5b, l'absorption des structures à motifs est nettement au-dessus de celle de la structure sans motif, en particulier pour la structure des pyramides inversées. Plus précisément, dans la gamme de longueurs d'onde de 300-500nm court, l'effet anti-réfléchissant est le plus efficace. Par ailleurs, il pourrait être noté qu'aucun pic d'absorption n'apparaît aux courtes longueur d'onde, où la longueur de pénétration des photons dans le c-Si est plus courte que l'épaisseur de la couche absorbante. Pour la plage de longueur d'onde de 500 à 700 nm, plusieurs résonances d'absorption correspondant aux modes de Fabry-Pérot se produisent sur les interfaces c-Si / ITO / Al. Par rapport à la configuration sans motif, dans la plage de longueurs d'onde de 700-1100nm, les trous cylindriques et les pyramides inversées présentent des résonances denses et irrégulières en absorption. Ces résonances correspondent à des modes de Bloch dans le matériau fortement dispersif et le guide d'onde multimode. Grâce aux motifs, la lumière entrante peut être couplée dans ces modes, puis sentir une absorption accrue par le mécanisme de piégeage de la lumière.

L'amélioration de l'absorption reste limitée aux grandes longueurs d'onde, en

particulier pour la structure des trous cylindriques. Par conséquent, un photon durée de vie plus longue est nécessaire pour tirer pleinement profit des résonances optiques de la structure. Une solution est d'introduire un CP à l'interface arrière pour augmenter l'absorption des cellules solaires [41-44]. Il diffracte la lumière non-absorbée propagée dans la couche active, ce qui équivaut à augmenter la longueur de trajet de la lumière. Ce concept en 1D structure de réseau a été développé dans nos études précédentes [14] et a prouvé numériquement une amélioration de J_{sc}. Dans cette section, un tel modèle avec double trous cylindriques est proposé pour augmenter encore l'absorption à grande longueur d'onde.

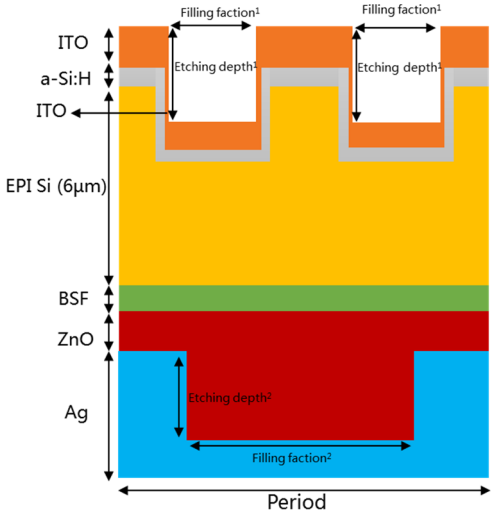

Figure 4-6 L'image schématique des motifs double (trous cylindriques de structure du CP) conçoit dans la vue de profil.

Comme le montre la séchma de la conception à la Fig. 4-6, tout l'empilement de cellule solaire est composé, de bas en haut, d'une couche d'argent en tant que contact et réflecteur, l'oxyde de zinc (ZnO) couche (comme un espaceur optique, 100 nm), 6μm d'épaisseur couche active c-Si reposant sur un c-Si fortement dopé agissant comme une couche BSF (100nm), passivée par la couche conforme (20nm) de a-Si:H et ensuite recouverte par la couche d'ITO continu (50 nm de l'épaisseur verticale sur le dessus, 7 nm sur la paroi latérale). Le ZnO a été utilisé à la place d'ITO, car il peut être moins absorbant. La structure de trous cylindriques périodique ont été introduits sur le dessus des couches ITO, a-Si:H et c-Si et dans la couche d'argent remplie de ZnO, avec 4 trous cylindriques dans une supercellule 2x2 sur le dessus et un trou cylindrique simple sur le fond en une seule période. Il peut être remarqué que comme le motif doit être répété

périodiquement pour la simulation, la période doit inclure des nombres entiers de motifs à la fois sur le haut et le grille inférieure. Le procédé d'optimisation par réglage de la géométrie des motifs du CP a été réalisé dans cette structure d'épaisseur de c-Si de 6 μm. En outre, nous avons également simulé seulement le réseau face avant afin de mettre en évidence l'amélioration de l'absorption.

Pour un double réseau optimisé de trous cylindriques, la période est de 680nm, le *ff* sur le dessus pour chaque trou est de 0,1 et sur le fond est de 0,5, et la profondeur de gravure pour le trou sur le dessus est de 150nm et sur le fond est de 200nm respectivement. La J_{sc} correspondant est 32.96mA/cm², ce qui est 2.39mA/cm² supérieur à la structure simple de trous cylindriques en face avant.

Conclusion

Dans ce chapitre, nous avons proposé les deux types de structures à CP: les pyramides inversées et les trous cylindriques, appliquées aux cellules solaires à couches minces complètes sur le dessus des couches. En effectuant les simulations numériques basées sur la méthode FDTD, les configurations optimisées ont été obtenues et on que le CP aidera les cellules solaires à couches minces à avoir un J_{sc} avec une augmentation relative jusqu'à 104,8 % par rapport à l'empilement sans motif. A partir de l'analyse de l'absorption dans chaque couche, la structure de pyramides inversées a une meilleure performance que la structure à trous cylindriques, principalement due à une anti-réflexion plus robuste et une efficacité de couplage supérieure aux grandes longueur d'ondes. Enfin, une seconde structure de trous cylindriques introduite en face arrière de la cellule solaire augmente l'absorption aux grandes longueurs d'onde, avec une densité de courant 2,39 mA/cm² supérieure à celle de structure face avant.

En tout, l'absorption de cellules solaires en couches minces avec une structure du CP périodique unique est meilleur que le design plat sans motif, mais reste encore faible aux grandes longueurs d'onde. L'ajout d'un second motif va augmenter l'absorption mais il augmente également le coût en même temps. Ainsi, dans le chapitre suivant, nous allons nous concentrer sur une autre conception pour augmenter encore l'absorption et maintenir le coût.

5. Simulation et fabrication de structures du CP pseudo-désordonné assisté cellules solaires en couches minces

Nous avons conçu des réseaux carrés de CP pour accroître l'absorption des cellules solaires en couches minces. Cependant, l'absorption dans la large gamme de longueur d'onde est encore faible. Cela est dû à la densité spectrale de modes limitée du CP. Ainsi, nous choisissons d'utiliser des structures pseudo-désordonné faites d'une supercellule répétée périodiquement dans un réseau carré. La supercellule est alors un ensemble aléatoire de trous cylindriques. Ces modèles peuvent encore être simulés avec les mêmes méthodes RCWA ou FDTD que précédemment. Pour la fabrication, la méthode d'écriture directe tels que la lithographie par faisceau d'électrons (EBL) sera généralement nécessaire pour un premier échantillon ou pour un masque qui peut être reproduit par une lithographie par nano-impression.

Un travail antérieur dans le groupe [31] a démontré numériquement l'intérêt dans un 200nm d'épaisseur de a-Si:H couche sur verre. Si cette structure est facile à analyser, grâce à un nombre réduit de modes guidés, l'intérêt pour le PV est très limité.

Le premier objectif de ce chapitre est de vérifier le potentiel de cette approche dans une configuration de cellules solaires plus réaliste, basé sur c-Si collé sur une couche métallique. Ensuite, des échantillons peuvent être obtenus et caractérisés. Dans le chapitre suivant, nous allons aller plus loin dans l'analyse et l'optimisation des modèles de pseudo-désordonné. Afin de révéler clairement l'influence de la structure pseudo-désordonné, nous nous sommes concentrés tout simplement sur l’empilement qui est un absorbeur (c-Si) sur un contact dans ce chapitre. Plus précisément, l’empilement à l'étude est un couche mince de 1 μm c-Si (voir annexe 1) collée sur une épaisseur de 1 μm d'aluminium (Al) sur un substrat de verre comme le montre la Fig. 5-1a.

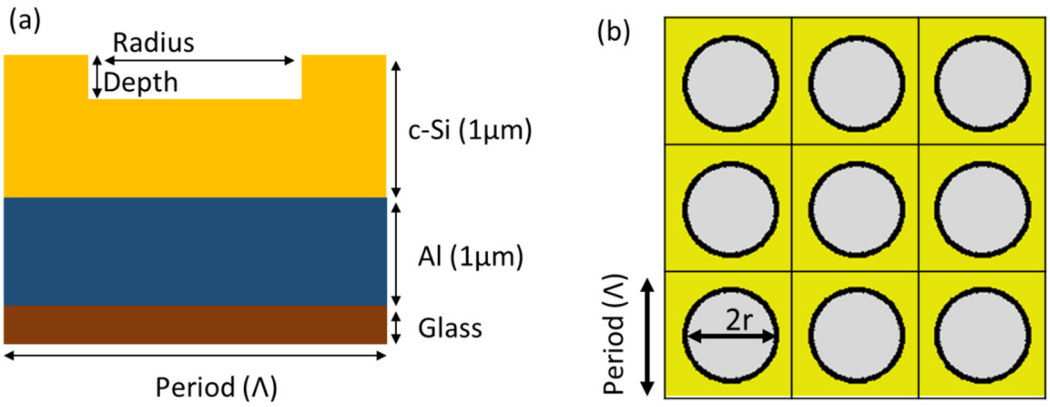

Figure 5-1. (a) c-Si mince sur une couche métallique collé sur un substrat de verre. (b) un réseau carré (période Λ) partiellement gravé (gravure de profondeur, h) trou (rayon, r) est utilisé pour augmenter l'absorption de l'empilement.

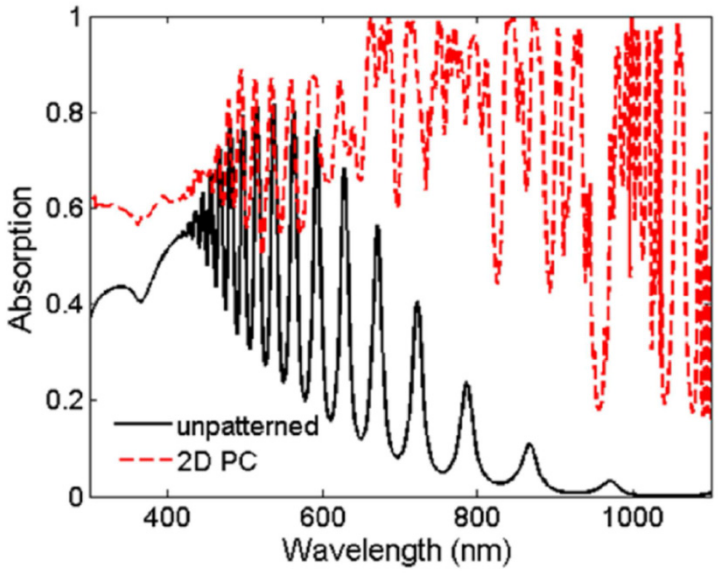

Figure 5-2. Comparaison de l'absorption entre les couches minces planes (courbe noire) et l'absorption du CP carré optimisé (ligne rouge pointillée) avec des couches en c-Si de 1µm d'épaisseur.

En réglant les paramètres, le période optimisée est période de 657 nm, le *ff* de 0,42 et la profondeur de gravure de 213,5nm. Le réseau carré de trous est très efficace pour les longueurs d'onde et des angles spécifiques en raison de la périodicité; ce qui correspond aux pics affichés sur la Fig. 5-2 par rapport au cas sans motif. Grâce à la structure du CP, l'absorption intégrée est améliorée de 37,7% (le cas sans motif) à 70,7% (réseau carré de la structure optimisée trous du CP), soit une amélioration relative de 87,8%.

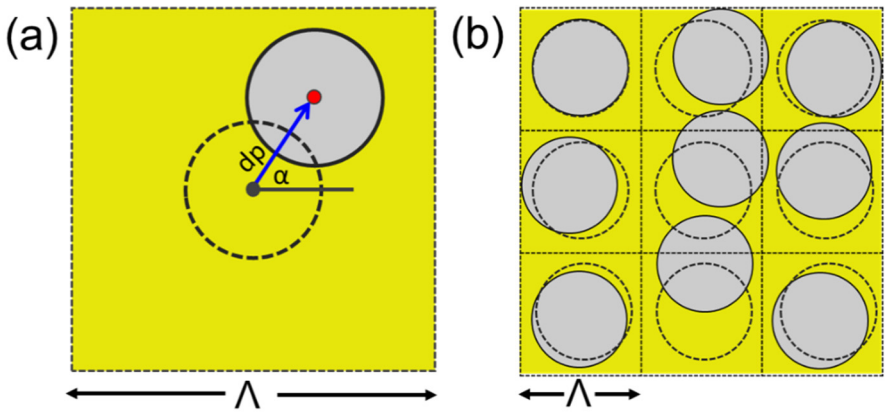

Figure 5-3. Schéma de la perturbation (a) pour un seul trou et (b) pour 9 trous dans une supercellule 3 x 3.

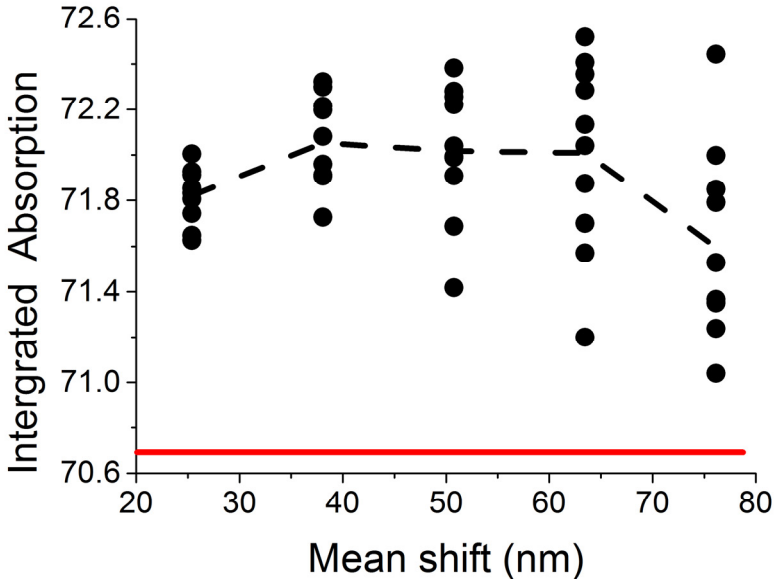

*Figure 5-4. Evolution de l'absorption intégrée théorique de 10*5 structures pseudo-désordonnées (points). La valeur moyenne de l'absorption intégrée (ligne noire pointillée) reste supérieure au CP optimisé de trous de référence (ligne horizontale rouge).*

Afin de surmonter ces limitations et ensuite augmenter l'absorption des cellules solaires à couches minces, nous proposons de modifier le CP régulier par le cas pseudo-désordonnée. Basé sur les paramètres du réseau carré de trous optimisé la structure, nous avons déplacé le trou indiqué sur la Fig. 5-3a à une distance de décalage (d*p*) sous un angle de *α*. La valeur de d*p* est déterminée par une distribution de Gauss, tandis que

l'angle est déterminé par une distribution uniforme. Puis ce processus de perturbation a été appliqué à 9 trous (Fig. 5-3b) composant une supercellule 3x3 et la supercellule est alors encore répliquée dans un réseau carré. Pour éviter les problèmes numériques et garder un design très réaliste, seuls les cas dans lesquels des trous ne fusionnent pas ont été considérés. Pour chaque valeur choisie de déplacement moyen (moyenne d*p*), nous avons simulé 10 structures différentes. Comme nous avons sélectionné 5 des valeurs différentes pour le changement moyen de 25nm à 75nm, nous avons calculé l'absorption intégré pour 50 structures différentes.

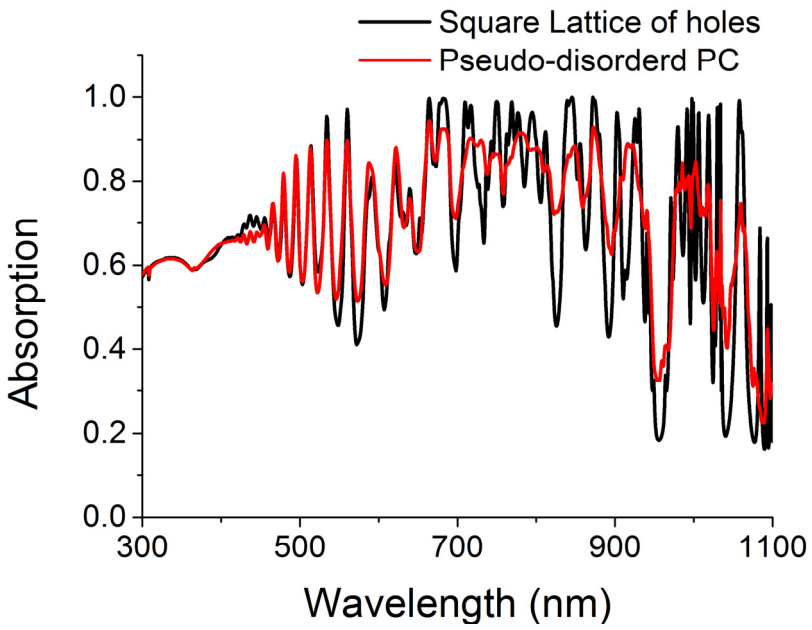

Figure 5-5. Comparaison entre l'absorption théorique du réseau carré optimisée de structure de trous (ligne noire) et de la meilleure structure pseudo-désordonnée (ligne rouge).

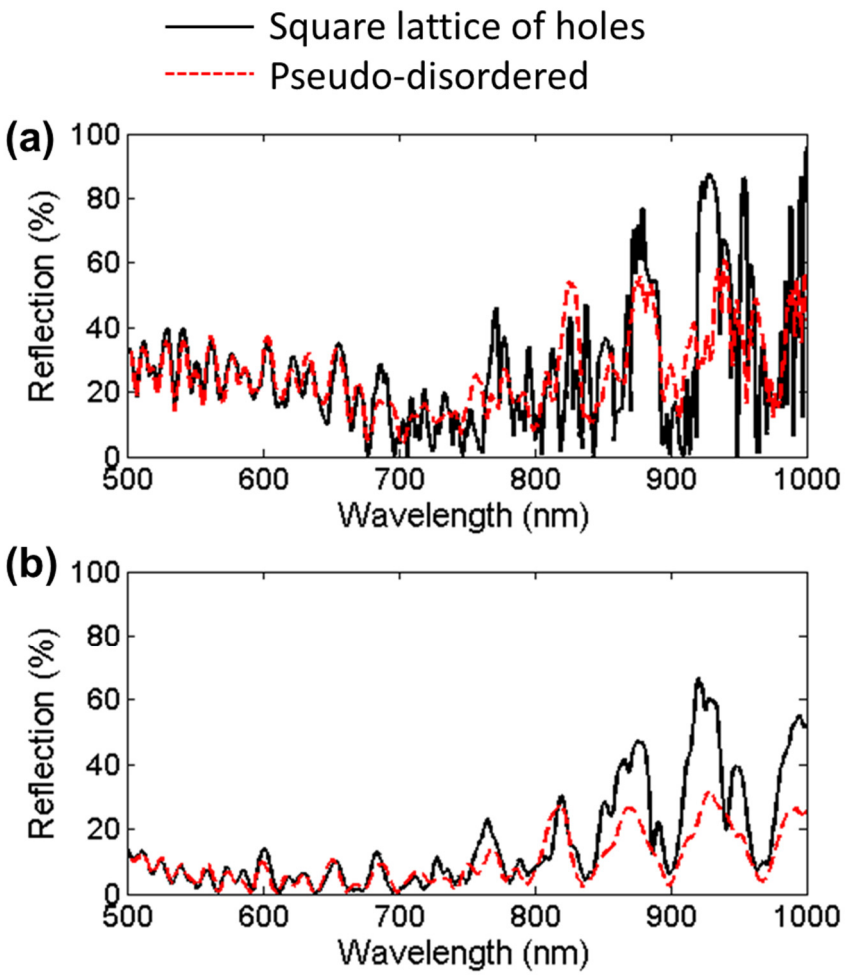

Figure 5-6 Comparaison entre la réflexion théorique (a) et réflexion expérimentale (b) spectres obtenus pour le réseau carré de trous (ligne noire) et la structure pseudo-désordonnée (ligne rouge pointillée).

Dans un premier temps, nous avons fait la comparaison théorie/expérience de réflexion (1-absorption) entre le réseau carré optimisé de trous et la structure de pseudo-désordonné sur l'échantillon SOI. Dans ce résultat théorique (Fig. 5-6a), la structure pseudo-désordonnée se comporte presque de la même façon que le réseau carré de trous dans la gamme de longueur d'onde inférieure à 700 nm, la même remarque peut être faite pour l'expérience (Fig. 5-6b). Conformément à cet accord à la fois dans le réseau carré de trous et la structure pseudo-désordonnée, nous pouvons conclure que le pseudo-désordre n'a aucun effet particulier sur l'absorption à ces longueurs d'onde. Dans la gamme de longueur d'onde 700-1000nm, les pics acérés du réseau carré de trous sont élargis dans la structure pseudo-désordonnée sur le spectre théorique (Fig. 5-6a). Les pics acérés attendus dans le cas pseudo-désordonnés sont liés à l'efficacité de

diffraction limitée de l'onde plane incidente dans les ordres ajoutée, même si leur intensité peut être petite. Cependant, comme la lumière incidente expérimentalement est un faisceau gaussien, la cohérence de cette lumière est inférieure à la cohérence de l'onde plane théorique. Ainsi, ces pics aigus ne sont pas visibles sur le spectre expérimental représenté sur la Fig. 5-6b. Pour les longueurs d'onde entre 700-1000nm, la réflexion expérimentale (Fig. 5-6b) de la structure de pseudo-désordonné est presque toujours inférieure à celle du réseau carré de trous.

A partir de ces résultats des deux modèles différents à la fois dans l'expérience et la simulation, les structures pseudo-désordonnées introduites ne modifient pas la réflexion aux courtes longueurs d'onde. Cependant, la réflexion inférieure à la plage de spectre expérimental de la simulation numérique dans la courte longueur d'onde qui est principalement dû à des variations expérimentales sur la rugosité de surface et la circularité des trous. Dans la longue plage de longueur d'onde, les écarts entre les conditions d'éclairage dans les cas expérimentaux et numériques (principalement faisceau gaussien vs onde plane), et compte tenu aussi du reste de la rugosité et la non-uniformité dans les structures fabriquées, les spectres de réflexion présentent de larges pics qui pourraient augmenter artificiellement l'absorption intégré mesurée. Pourtant, l'introduction d'un pseudo-désordre dans un PC simplement périodique ne conduit pas à une diminution de la réflexion à grandes longueurs d'onde.

Tenant compte de toutes ces remarques, nous allons maintenant faire l'étude de l'effet du pseudo-désordre sur une mince couche de c-Si collée sur une couche de métal sur un substrat de verre.

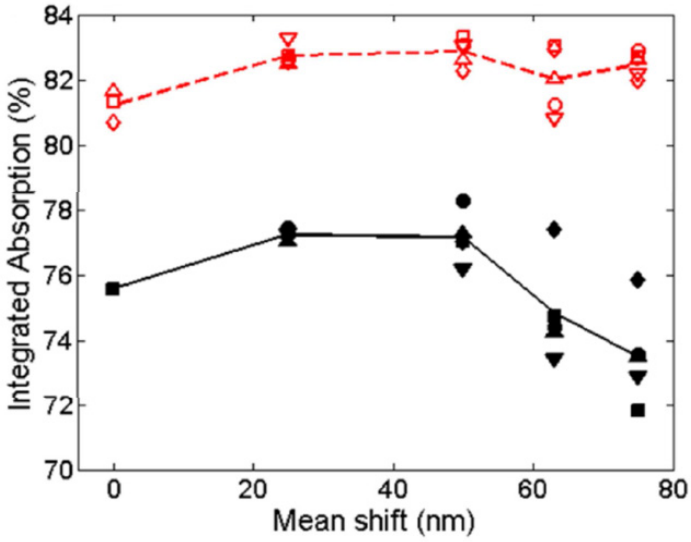

Figure 5-7. Evolution de la moyenne intégrée d'absorption expérimentalement (ligne rouge pointillée) et théoriquement (noir ligne). Les symboles remplis (symboles vides) correspondent à mesure (simulation) d'absorption intégrée pour différente structure désordonnée Pseudo-aléatoire. La valeur de référence pour le réseau carré de trous correspond à une valeur de décalage de 0nm.

La Fig. 5-7 montre que la valeur moyenne de l'absorption intégrée pour les structures théoriques et expérimentales pseudo-désordonnées présentent à peu près le même comportement. Dans un premier temps, on observe à la fois l'augmentation de l'absorption théorique et expérimentale avec la faible augmentation de la valeur de décalage moyenne. Ensuite, si la valeur de décalage moyen pour continuer à augmenter, l'absorption moyenne diminue. La principale différence entre les 2 courbes apparaît pour le décalage moyen le plus élevé : l'absorption expérimentale ne diminue pas. De plus, quand le décalage moyenne augmente, l'écart type des augmentations d'absorption intégrée expérimentalement ainsi que théoriquement augmentent. Même si la valeur moyenne de l'absorption optique mesurée est de 5,7% plus élevé que celle simulée, les améliorations maximales de la valeur moyenne du fait du pseudo-désordre sont tout à fait comparables dans les expériences et simulation (environ 1,7% en valeur absolue). Pour la meilleure structure pseudo-désordonnée, l'absorption intégrée expérimentale augmente de 2,1% par rapport au réseau carré de trous, soit un peu moins que l'augmentation théorique de 2,7%.

Conclusion

Grâce à la simulation par la methode de RCWA, nous avons introduit une conception de cellule solaire basée sur une couche de 1 µm de c-Si sur une couche Al, structurée en CP régulier ou pseudo-désordonné. L'absorption intégrée de ce dernier est supérieure à celle d'un réseau carré entièrement optimisé, tandis que sa fabrication peut être réalisée en utilisant exactement le même processus. Afin de démontrer davantage l'intérêt de ces modèles complexes nanophotonique, des expériences ont été réalisées sur des motifs réguliers et pseudo-désordonnés dans une plaquette SOI, afin de mettre en évidence l'influence des fluctuations expérimentales liées aux imperfections du processus, et de l'impact des conditions d'éclairage sur les spectres d'absorption attendue. Les imperfections technologiques augmentent principalement l'absorption optique dans la couche c-Si aux longueurs d'onde les plus courtes du spectre solaire. Puis les pseudo-désordonnés alors sélectionnés ont été réalisés dans un film de c-Si mince collé sur le dessus de la couche de métal. L'absorption intégrée mesurée expérimentalement dans cet empilement de cellule solaire présente presque le même comportement que celui théorique, malgré un décalage constant. Comparé à un cristal photonique simplement périodique, la meilleure structure de pseudo-désordonné améliore l'absorption optique jusqu'à 2,1%, ce qui est en bon accord avec l'augmentation de 2,7% théoriquement prévue.

L'étude optique sera ultérieurement étendue au cas d'une cellule solaire entièrement fonctionnelle, permettant la caractérisation électro-optique. Le défi se trouve dans la fabrication de structures de plus d’un centimètre carré en utilisant la réplication d'un masque maître fabriqué par EBL et RIE.

6. Règles de conception pour l'amélioration de l'absorption nette en cristal photonique pseudo-désordonné assistés cellules solaires en couches minces

Dans ce chapitre, nous allons profondément analyser l'influence du pseudo-désordre sur les cellules solaires en couches minces avec des simulations numériques RCWA. La structure de pseudo-désordre introduite dans la couche de c-Si de 1 µm au chapitre 5 conduit à une absorption globale plus importante que dans la structure régulière optimisé de trous cylindriques à la fois dans les cas numérique et expérimental. Cependant, l'empilement considéré n'a pas d'ITO, l'épaisseur est très limitée, et aucune régle de conception n'est mise en évidence. Par conséquent, nous utilisons la méthode RWCA pour optimiser l'absorption nette du pseudo-désordonné dans un schéma de cellule solaire plus réaliste avec une couche épaisse de 1, 2, 4 et 8 um c-Si recouvert d'ITO, par rapport à des cas périodiques purs optimisés correspondant.

Nous étudions numériquement les mécanismes d'absorption dans ces structures, à la fois dans l'espace réel et de Fourier, en vue de déterminer les lignes directrices de conception pour permettre une augmentation nette de l'absorption. Enfin, nous discutons de la réponse angulaire de ces structures.

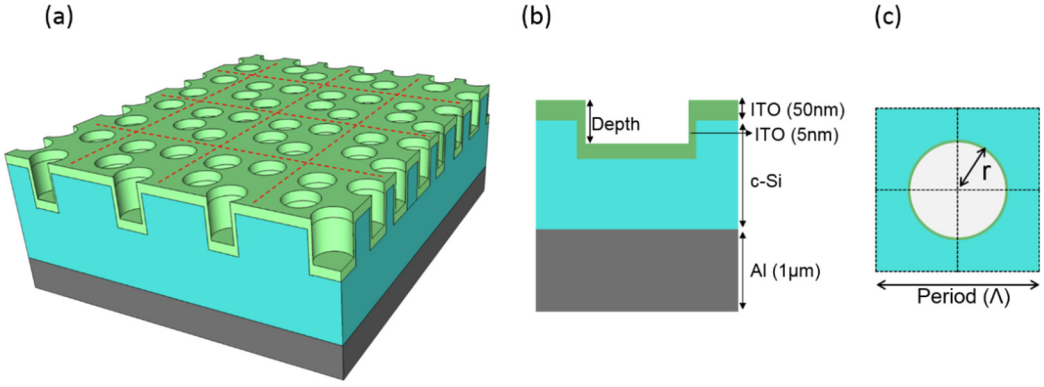

Figure 6-1. (a) Schéma de cellules solaires couche mince pseudo-désordonnée. (b) en vue latérale et (c) en vue de dessus

L'empilement pris en compte dans ce travail est représenté sur la Fig. 6-1a. Il se compose d'une couche absorbante mince de c-Si collé sur une couche de 1 µm d'Al qui

agit comme un miroir et contact arrière (voir indice optique en annexe 1). Ensuite, une structure CP 2D est gravé dans le c-Si, comme représenté sur la Fig. 6-1b et 6-1c, puis recouvert d'ITO. Comme le montre la figure 1b, l'épaisseur de la couche d'ITO est pas la même pour les surfaces horizontales et des parois latérales, comme cela est le cas pour les cellules solaires fabriquées [36].

Les résultats de l'optimisation pour un réseeau carré de trous sont donnés dans le Table.6-1 pour les différentes épaisseurs de la couche c-Si, et pour un empilementcomprenant des couches Al et ITO.

Table.6-1 J_{sc} (mA / cm²) atteignable avec et sans un réseau carré de trous, pour différentes épaisseurs de la couche de c-Si. Les paramètres (période, fraction de remplissage et la profondeur du trou) correspondent à la valeur maximale pour le réseau carré de trous optimisé.

c-Si (μm)	J_{sc} (mA/cm²)		Period (nm)	Filling fraction (*ff*)	Etching depth (nm)
	Flat	Square Lattice			
1	13.82	19.96	620	0.38	165
2	17.96	23.71	570	0.42	180
4	21.91	27.46	620	0.42	200
8	25.42	30.69	650	0.44	210

Afin d'augmenter encore l'absorption de cellules solaires en couches minces, nous proposons d'intégrer des motifs pseudo-désordonnés, comme définis au chapitre précédent.

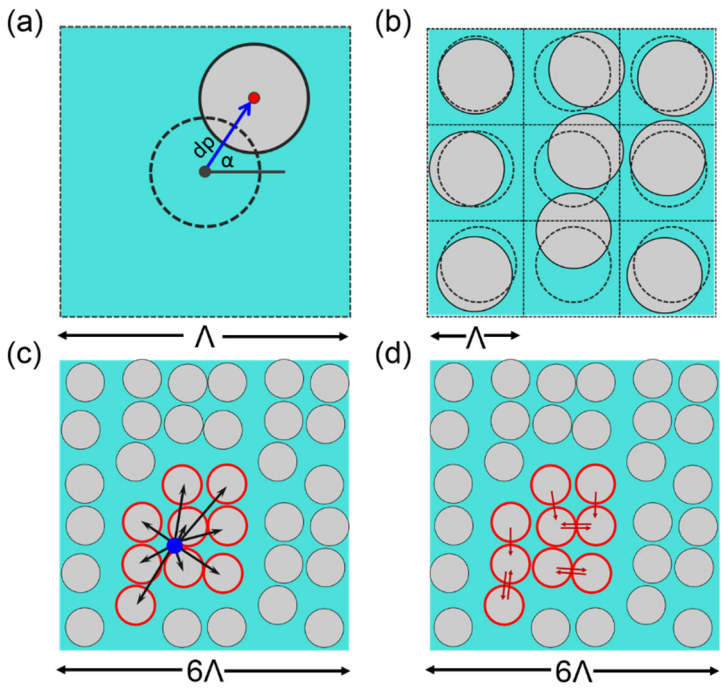

Figure 6-2. Schéma de la perturbation (a) pour un seul trou et (b) pour 9 trous dans une supercellule 3x3. (c&d) Détermination des pseudo-désordonné paramètres de la structure grâce à la réplication de la supercellule 3x3. (c) Le point bleu représente le barycentre des trous rouges sélectionnés, qui est utilisé pour déterminer le paramètre "compacité". (d) La distance minimale entre les 9 trous représentés par les flèches rouges détermine le paramètre de « clustering ».

Comme montré dans la suite, les supercellules présentent différentes formes qui peuvent conduire à des situations très diverses, comme des groupes de trous ou des trous positionnés de manière plus égale et espacée. Afin d'analyser les effets du désordre introduit dans l'espace réel, nous devons définir des métriques pertinentes qui peuvent classer les structures pseudo-désordonné. Ainsi, nous définissons deux paramètres pour décrire la structure de pseudo-désordonné, en termes de regroupement (« clustering ») et de compacité.

Parmi tous les arrangements possibles des trous dans le réseau de supercellules, nous sélectionnons la distance moyenne la plus basse entre chacun des trous N^2 et leur centre de gravité. Dans l'exemple représenté sur la Fig. 6-2c et d, le groupe de trous N^2 sélectionné en utilisant ce critère correspond aux cercles rouges, ce groupe constitue une supercellule alternative à la place initiale d'un. Ensuite, pour l'ensemble correspondant de N^2 trous, on calcule la distance moyenne entre chaque trou et son

voisin le plus proche (Fig. 6-3d). Cette valeur est appelée le paramètre de regroupement; une valeur faible de regroupement correspond à la présence de grappe(s) de trous de la supercellule. Cela signifie également que le paramètre de compacité faible associée à une faible valeur de regroupement indique que le motif est constitué d'un seul groupe de N^2 trous , alors qu'un grand paramètre de compacité d'une valeur faible de regroupement correspondant à plusieurs groupes de trous. Alors que l'on peut anticiper que ces deux paramètres sont perspicaces pour l'étude des structures pseudo-désordonnée, il faut remarquer qu'ils ne sont pas suffisants pour décrire complètement la structure.

Si quelques trous sont trop proches les uns des autres, conduisant à une faible valeur de regroupement, comme dans les distributions indiquées dans la figure. 6-3f et 6-3g, J_{sc} est faible. Si en outre le paramètre de compacité est faible, comme pour la distribution de trous dans la Fig. 6-3e, il y a une seule grappe de trous dans chaque supercellule $N \times N$ et J_{sc} de la structure est encore plus faible. Les valeurs les plus élevées de J_{sc} sont obtenus pour les structures pseudo-désordonné qui présentent une valeur relativement élevée du regroupement. Pour la supercellule 2x2, l'analyse statistique indique que la structure correspondant au Jsc le plus élevé, présenté à la Fig. 6-3b, présente une distribution «homogène», avec des trous répartis uniformément et sans effet de regroupement. Au contraire, la structure pseudo-désordonnée correspondant au plus faible Jsc présenté sur la Fig. 6-3e présente la situation inverse. Pour les 3x3 et 4x4 supercellules, la JSC plus élevé obtenu correspond à de plus grands clusters paramètres (Fig. 6-3c et 6-3d), même si pas le plus important. Le plus bas Jsc correspond à des modèles qui présentent un fort regroupement (Fig. 6-3f et 6-3g), le paramètre de regroupement étant parmi les valeurs les plus basses de l'échantillon.

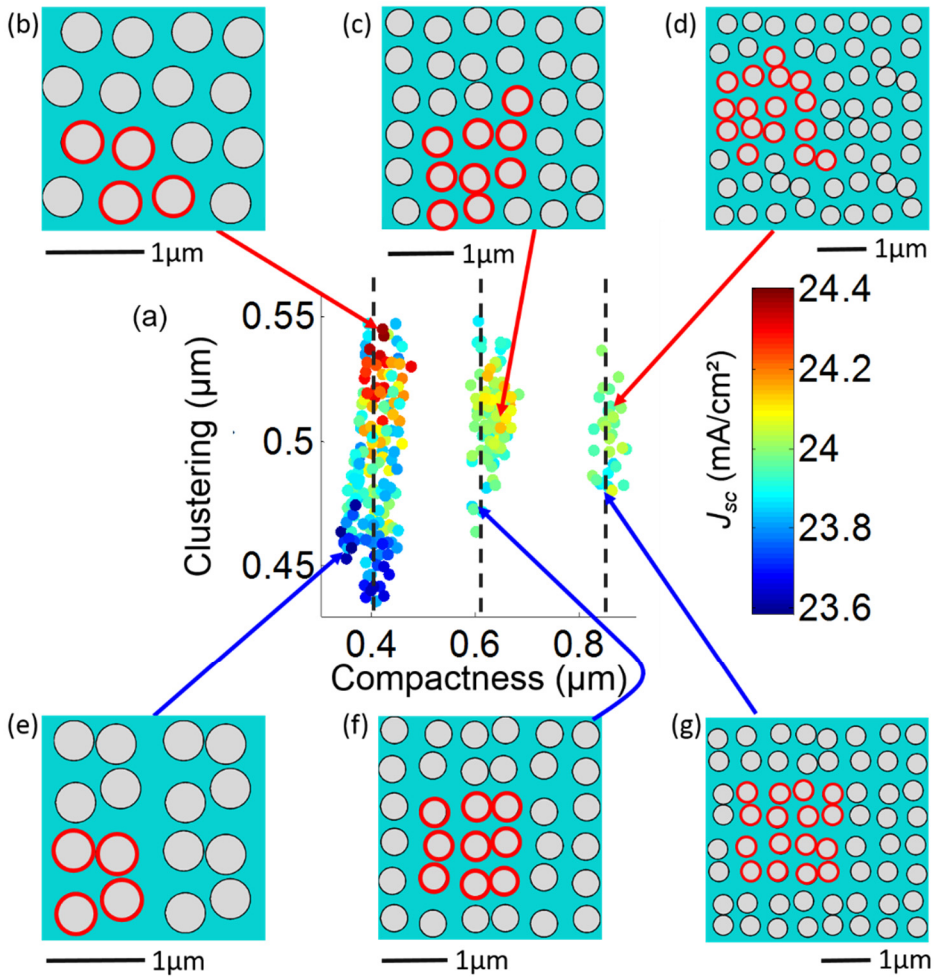

Figure 6-3. Carte des J_{sc} mA / cm² (a) en fonction de regroupement et de compacité paramètres de la structure de pseudo-désordonné pour la couche épaisse de 2 pm cas c-Si. Les lignes noires pointillées représentent le paramètre de compacité du réseau carré optimisé de trous (référence) pour la supercellule 2x2 (près de 0.40µm), 3x3 (~ 0.61µm) et 4x4 (~ 0.85µm). Le paramètre de regroupement ('clustering') du réseau carré optimisé de trous structure correspond à la période du réseau et est 0.57µm. Les vues schématiques correspondent à la distribution de trou de la structure pseudo-désordonnée qui présentent J_{sc} le plus élevé pour les supercellules 2x2, 3x3 et 4x4 (b, c, d), et Jsc le plus bas pour les mêmes cas (e, f, g). Les cercles rouges mettent en évidence la supercellule.

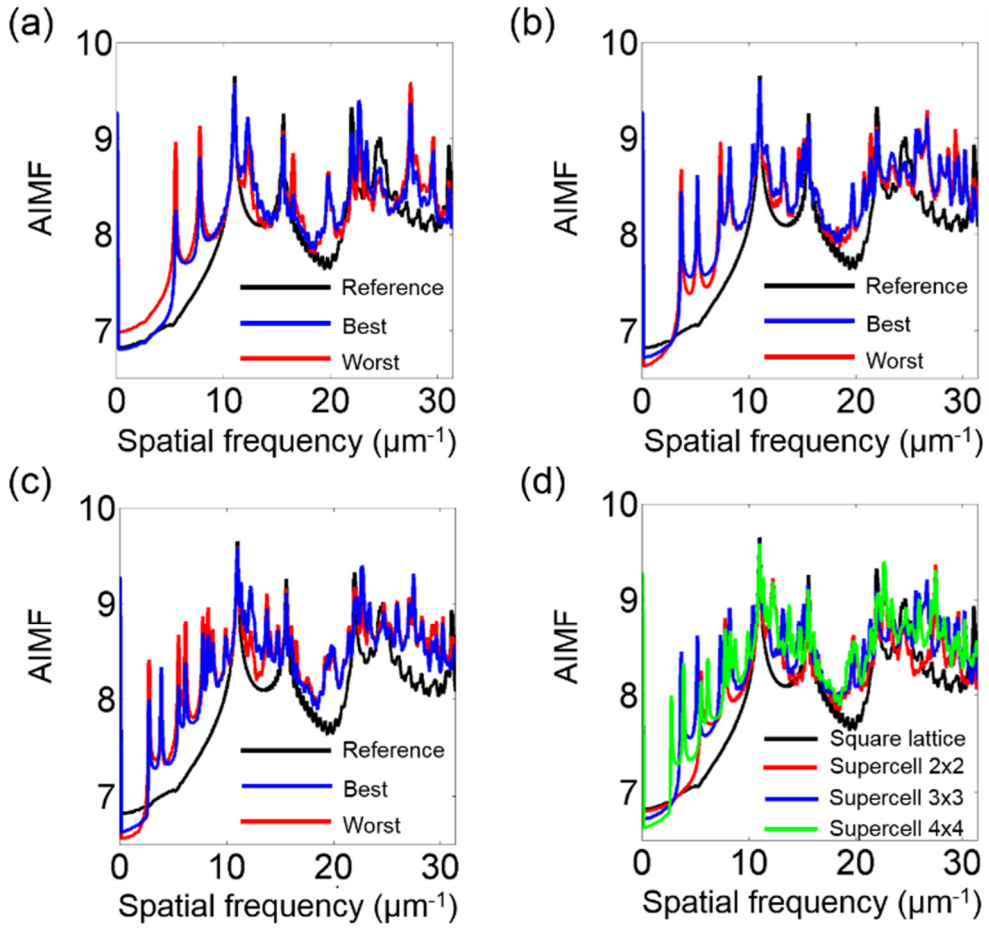

Figure 6-4. Amplitude de la composante de Fourier de la fonction diélectrique de la nanostructure considéré intégrée angulairement (AIMF). Pour 2 µm de c-Si, les résultats pour les meilleurs (rés. pire) structures pseudo-désordonnées sont en bleu (resp. rouge) et pour le réseau carré optimisé de trous en noir dans le cas d'une supercellule 2x2 (a), 3x3 (b) et 4x4 (c). La meilleure structure pseudo-désordonné pour chaque taille de supercellule et le réseau carré de trous structure sont également tracées ensemble (d).

Dans l'espace de Fourier de la fonction diélectrique du PC optimisé avec un réseau carré et les structures pseudo-désordonné dans le 2µm d'épaisseur c-Si empilement de couches. L'ampliture de la composante de Fourier intégrée angulairement (AIMF) des fonctions diélectriques de quelques structures sélectionnées (les meilleures et les pires structures pseudo-désordonnées, et le réseau carré optimisé de trous), sont représntés Fig. 6-4a, b et c pour chaque taille de supercellule. Dans ces trois cas, il apparaît que l'AIMF de toutes les structures pseudo-désordonnées sont presque toujours plus élevés que ceux du réseau carré optimisé de trous, sur toute la plage de fréquences spatiales

d'intérêt. En outre, il apparaît que les pires structures présentent des amplitudes de faibles composantes de fréquence spatiale (<10μm^{-1}) plus élevées que les meilleurs dessins. Puis en se concentrant sur les meilleures structures pseudo-désordonnées pour chaque taille de supercellule (Fig. 6-4d), et par rapport à la trame carrée optimisé de trous, il est à remarquer que le meilleure Jsc est obtenu dans le cas de 2x2, et correspond à la plus petite augmentation des composantes de Fourier dans la gamme de basse fréquence spatiale (<10 μm^{-1}). Leur optimisation a conduit à un schéma qui présente des composantes de Fourier avec une faible amplitude dans une plage de basses fréquences jusqu'à $2\pi/\lambda_0$, laquelle λ_0 correspondant à une longueur d'onde où l'absorption dans le silicium devient faible. Dans notre cas, nous avons mis la limite entre les gammes basse et haute fréquence à $2\pi/\Lambda$, Λ étant la période du réseau carré de trous, proche de la valeur de λ_0 choisi [45].

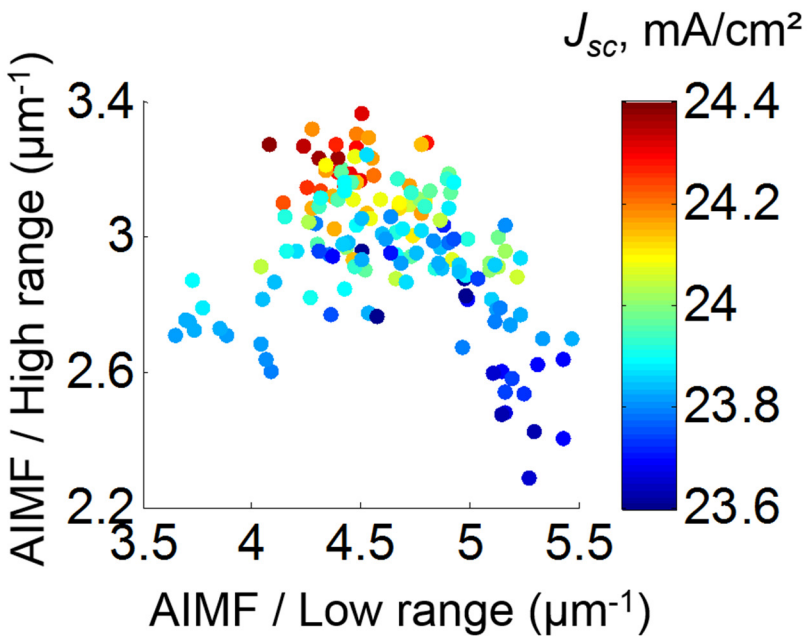

Figure 6-5. Le densité de courant (J_{sc}, mA / cm²) de l'épaisse empilement de couches de c-Si 2μm modelé par des structures pseudo-désordonnée dans une supercellule 2x2 en fonction du poids des composants basse et haute fréquence. Le poids des basses (resp. De haut) composantes de fréquence est déterminée par l'AIMF dans [0 $2\pi/\Lambda$] (resp. [$2\pi/\Lambda$ $4\pi/\Lambda$]).

Nos résultats sont ensuite triés selon les deux critères précédents. Pour une supercellule 2x2 avec la couche de 2μm de c-Si, les Jsc sont affichés en fonction de la AIMF dans les deux gammes de fréquence, comme le montre la Fig. 6-5. Des valeurs

élevées de J_{sc} sont atteintes pour les modèles avec une grande amplitude de la fonction diélectrique intégré dans la gamme de fréquence élevée et une amplitude relativement faible dans la gamme des basses fréquences. Il apparaît alors que deux critères suggérés dans les anciennes études mentionnées ci-dessus doivent être simulatnément satisfaits [45, 46].

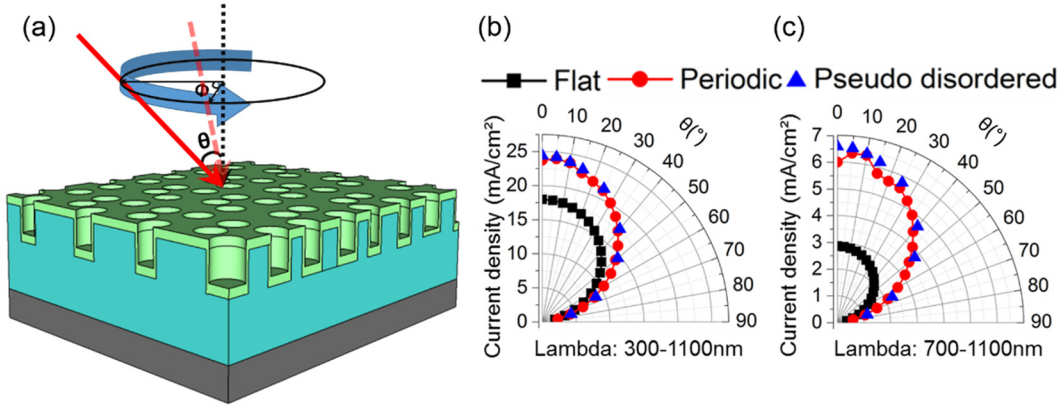

Figure 6-6. (a) Schéma d'une lumière incidente oblique sous un angle d'incidence θ avec un angle Φ conique. Pour la couche épaisse pile de c-Si 2 pm, l'évolution de JSC pour le réseau carré optimisé de trous structure (point rouge), pour les meilleures structures pseudo-désordonné (triangle bleu) et pour le cas plat (carré noir) sur un spectre qui étend de 300 à 1100 nm (b) et de 700 à 1100 nm (c).

La densité courant de court-circuit prédite en utilisant cette approche est tracée dans la Fig. 6-6b pour toute la gamme d'angles d'incidence (θ), et pour différentes structures: l'empilement sans motif, le réseau carré optimisé de trous et la meilleure structure pseudo-désordonnée dans la supercellule de 2x2, avec 2µm de c-Si. En premier lieu, cela montre que le J_{sc} de la meilleure structure pseudo-désordonnée est toujours supérieure à celui du réseau carré de trous optimisé. Deuxièmement, le réseau carré optimisé de trous présente une augmentation inhabituelle de J_{sc} aux petits angles (environ 5-10° sur l'axe vertical) en raison de la possibilité de coupler la lumière incidente en résonances par la brisure de symétrie sous l'incidence oblique [47, 48]. Autour de cet angle, la différence entre le réseau carré optimisé de trous et de la meilleure structure de pseudo-désordonné est la plus faible; l'absorption est seulement 0,5% plus élevée avec la structure de pseudo-désordonné. Pour un angle d'incidence plus élevé, la différence de J_{sc} augmente jusqu'à 2,3%. Dans l'ensemble, dans tous les cas, le J_{sc} diminue lorsque l'angle d'incidence augmente. Ce comportement est général

pour tous les types de cellules solaires sans traqueur, et est principalement due à une diminution de la densité de puissance d'incidence à la surface des cellules solaires; ceci est un simple effet géométrique. Comme représenté avant, le pseudo-désordre influence notamment l'efficacité d'absorption aux grandes longueurs d'onde. Dans la gamme 700-1100nm, la nanostructuration double l'efficacité de l'absorption d'un empilement de couches minces non structuré pour tous les angles d'incidence. Comme prévu, le gain entre la structure pseudo-désordonnée et réseau carré de trous structure est plus élevé pour cette gamme de longueur d'onde, avec une augmentation de 4,4%. Enfin, on peut remarquer que les fluctuations J_{sc} survenant en dessous de 30° pour le réseau carré de trous disparaissent dans le cas de la structure pseudo-désordonnée, conduisant à une diminution lente J_{sc} pour les grands angles d'incidence.

Conclusion

Nous avons étudié l'effet d'un motif pseudo-désordonné sur l'absorption des empilements solaires technologiquement réalistes comprenant une couche mince absorbante c-Si, une électrode avant transparente, et une couche métallique en face arrière. Tout d'abord, nous avons montré que l'absorption de la structure pseudo-désordonnée dépasse l'absorption d'un réseau 2D carré optimisé de trous pour une large gamme d'épaisseurs de c-Si. Puis, grâce aux paramètres utilisés pour caractériser le pseudo-désordre, nous mettons en évidence que le regroupement de trous doit être évité pour atteindre un haut J_{sc}. L'étude de ces structures dans l'espace réciproque montre que les deux critères proposés séparément dans la littérature pour optimiser nanoschémas complexes doivent être remplies simultanément. Enfin, les structures pseudo-désordonné conduisent à une haute J_{sc} non seulement pour une incidence normale, mais aussi pour une large gamme d'angles d'incidence.

Grâce aux techniques de nano-impression basées sur la réplication d'un tampon maître associé aux processus de transfert comme la gravure par plasma [49], la structure pseudo-désordonnée proposée dans cette thèse peut être réalisée en utilisant exactement les mêmes processus que le réseau carré optimisé des trous sans coût supplémentaire. L'utilisation des règles de conception présentés dans ce chapitre ainsi que des procédés de nanostructuration pertinente devrait donc conduire à des cellules solaires à couches minces très efficaces et angulairement stables.

Bibliographie

1. G. Boyle, *Renewable energy* (OXFORD university press, 2004).
2. M. A. Green, "Solar cells: operating principles, technology, and system applications," (1982).
3. A.-E. Becquerel, "Mémoire sur les effets électriques produits sous l'influence des rayons solaires," Comptes Rendus **9**, 1839 (1839).
4. M. A. Green, K. Emery, Y. Hishikawa, W. Warta, and E. D. Dunlop, "Solar cell efficiency tables (Version 45)," Progress in photovoltaics: research and applications **23**, 1-9 (2015).
5. A. El-Ghonemy, "Photovoltaic solar energy: review," International Journal of Scientific & Engineering Research **3**(2012).
6. B. Parida, S. Iniyan, and R. Goic, "A review of solar photovoltaic technologies," Renewable and sustainable energy reviews **15**, 1625-1636 (2011).
7. G. Singh, "Solar power generation by PV (photovoltaic) technology: a review," Energy **53**, 1-13 (2013).
8. S. Wenham and M. Green, "Silicon solar cells," Progress in Photovoltaics: Research and Applications **4**, 3-33 (1996).
9. W. Shockley and H. J. Queisser, "Detailed balance limit of efficiency of p‐n junction solar cells," Journal of applied physics **32**, 510-519 (1961).
10. E. Yablonovitch, "Statistical ray optics," JOSA **72**, 899-907 (1982).
11. T. Tiedje, E. Yablonovitch, G. D. Cody, and B. G. Brooks, "Limiting efficiency of silicon solar cells," Electron Devices, IEEE Transactions on **31**, 711-716 (1984).
12. E. Garnett and P. Yang, "Light Trapping in Silicon Nanowire Solar Cells," Nano Letters **10**, 1082-1087 (2010).
13. J. Michallon, D. Bucci, A. Morand, M. Zanuccoli, V. Consonni, and A. Kaminski-Cachopo, "Light trapping in ZnO nanowire arrays covered with an absorbing shell for solar cells," Optics express **22**, A1174-A1189 (2014).
14. X. Meng, E. Drouard, G. Gomard, R. Peretti, A. Fave, and C. Seassal, "Combined front and back diffraction gratings for broad band light trapping in thin film solar cell," Optics Express **20**, A560-A571 (2012).
15. C. S. Schuster, P. Kowalczewski, E. R. Martins, M. Patrini, M. G. Scullion, M. Liscidini, L. Lewis, C. Reardon, L. C. Andreani, and T. F. Krauss, "Dual gratings

for enhanced light trapping in thin-film solar cells by a layer-transfer technique," Optics express **21**, A433-A439 (2013).

16. Y. Shi, X. Wang, W. Liu, T. Yang, and F. Yang, "Light-absorption enhancement in thin-film silicon solar cells with front grating and rear-located nanoparticle grating," physica status solidi (a) **212**, 312-316 (2015).
17. Z. Xia, Y. Wu, H. Jiao, H. Cao, Z. Liang, J. Zhou, and X. Qin, "Thin film silicon solar cells with non-simple integral period ratio between front and back gratings," Journal of Optics **16**, 105011 (2014).
18. S. Vedraine, P. Torchio, D. Duché, F. Flory, J.-J. Simon, J. Le Rouzo, and L. Escoubas, "Intrinsic absorption of plasmonic structures for organic solar cells," Solar energy materials and solar cells **95**, S57-S64 (2011).
19. K. R. Catchpole and A. Polman, "Plasmonic solar cells," Optics Express **16**, 21793-21800 (2008).
20. H. A. Atwater and A. Polman, "Plasmonics for improved photovoltaic devices," Nat Mater **9**, 205-213 (2010).
21. X. Meng, G. Gomard, O. El Daif, E. Drouard, R. Orobtchouk, A. Kaminski, A. Fave, M. Lemiti, A. Abramov, and P. R. i Cabarrocas, "Absorbing photonic crystals for silicon thin-film solar cells: Design, fabrication and experimental investigation," Solar Energy Materials and Solar Cells **95**, S32-S38 (2011).
22. M. Burresi, F. Pratesi, F. Riboli, and D. S. Wiersma, "Complex Photonic Structures for Light Harvesting," Advanced Optical Materials (2015).
23. X. Sheng, L. Z. Broderick, and L. C. Kimerling, "Photonic crystal structures for light trapping in thin-film Si solar cells: Modeling, process and optimizations," Optics Communications **314**, 41-47 (2014).
24. G. Gomard, R. Peretti, E. Drouard, X. Meng, and C. Seassal, "Photonic crystals and optical mode engineering for thin film photovoltaics," Optics Express **21**, A515-A527 (2013).
25. D. Duché, C. Masclaux, J. Le Rouzo, and C. Gourgon, "Photonic crystals for improving light absorption in organic solar cells," Journal of Applied Physics **117**, 053108 (2015).
26. J. D. Joannopoulos, S. G. Johnson, J. N. Winn, and R. D. Meade, *Photonic crystals: molding the flow of light* (Princeton university press, 2011).
27. F. Pratesi, M. Burresi, F. Riboli, K. Vynck, and D. S. Wiersma, "Disordered photonic structures for light harvesting in solar cells," Optics Express **21**, A460-

A468 (2013).

28. R. A. Pala, J. S. Liu, E. S. Barnard, D. Askarov, E. C. Garnett, S. Fan, and M. L. Brongersma, "Optimization of non-periodic plasmonic light-trapping layers for thin-film solar cells," Nature communications **4**(2013).
29. J. Xavier, J. Probst, F. Back, P. Wyss, D. Eisenhauer, B. Löchel, E. Rudigier-Voigt, and C. Becker, "Quasicrystalline-structured light harvesting nanophotonic silicon films on nanoimprinted glass for ultra-thin photovoltaics," Optical Materials Express **4**, 2290-2299 (2014).
30. D. S. Wiersma, "Disordered photonics," Nature Photonics **7**, 188-196 (2013).
31. R. Peretti, G. Gomard, L. Lalouat, C. Seassal, and E. Drouard, "Absorption control in pseudodisordered photonic-crystal thin films," Physical Review A **88**, 053835 (2013).
32. A. Oskooi, M. De Zoysa, K. Ishizaki, and S. Noda, "Experimental Demonstration of Quasi-resonant Absorption in Silicon Thin Films for Enhanced Solar Light Trapping," ACS Photonics **1**, 304-309 (2014).
33. J. R. Nagel and M. A. Scarpulla, "Enhanced absorption in optically thin solar cells by scattering from embedded dielectric nanoparticles," Optics express **18**, A139-A146 (2010).
34. G. Gomard, X. Meng, E. Drouard, K. El Hajjam, E. Gerelli, R. Peretti, A. Fave, R. Orobtchouk, M. Lemiti, and C. Seassal, "Light harvesting by planar photonic crystals in solar cells: the case of amorphous silicon," Journal of Optics **14**, 024011 (2012).
35. M. Moharam and T. Gaylord, "Rigorous coupled-wave analysis of planar-grating diffraction," JOSA **71**, 811-818 (1981).
36. V. Depauw, X. Meng, O. El Daif, G. Gomard, L. Lalouat, E. Drouard, C. Trompoukis, A. Fave, C. Seassal, and I. Gordon, "Micrometer-thin crystalline-silicon solar cells integrating numerically optimized 2-D photonic crystals," Photovoltaics, IEEE Journal of **4**, 215-223 (2014).
37. V. Depauw, Y. Qiu, K. Van Nieuwenhuysen, I. Gordon, and J. Poortmans, "Epitaxy‐free monocrystalline silicon thin film: first steps beyond proof‐of‐concept solar cells," Progress in Photovoltaics: Research and Applications **19**, 844-850 (2011).
38. J. Y. Kim, S. H. Kim, H. H. Lee, K. Lee, W. Ma, X. Gong, and A. J. Heeger, "New

Architecture for High-Efficiency Polymer Photovoltaic Cells Using Solution-Based Titanium Oxide as an Optical Spacer," Advanced Materials **18**, 572-576 (2006).

39. A. K. K. Kyaw, D. H. Wang, D. Wynands, J. Zhang, T.-Q. Nguyen, G. C. Bazan, and A. J. Heeger, "Improved Light Harvesting and Improved Efficiency by Insertion of an Optical Spacer (ZnO) in Solution-Processed Small-Molecule Solar Cells," Nano Letters **13**, 3796-3801 (2013).
40. G. Gomard, E. Drouard, X. Letartre, X. Meng, A. Kaminski, A. Fave, M. Lemiti, E. Garcia-Caurel, and C. Seassal, "Two-dimensional photonic crystal for absorption enhancement in hydrogenated amorphous silicon thin film solar cells," Journal of Applied Physics **108**, 123102 (2010).
41. L. Zeng, P. Bermel, Y. Yi, B. Alamariu, K. Broderick, J. Liu, C. Hong, X. Duan, J. Joannopoulos, and L. Kimerling, "Demonstration of enhanced absorption in thin film Si solar cells with textured photonic crystal back reflector," Applied Physics Letters **93**, 221105 (2008).
42. J. G. Mutitu, S. Shi, C. Chen, T. Creazzo, A. Barnett, C. Honsberg, and D. W. Prather, "Thin film solar cell design based on photonic crystal and diffractive grating structures," Optics Express **16**, 15238-15248 (2008).
43. Y. Shi, X. Wang, W. Liu, T. Yang, and F. Yang, "Hybrid light trapping structures in thin-film silicon solar cells," Journal of Optics **16**, 075706 (2014).
44. K. X. Wang, Z. Yu, V. Liu, Y. Cui, and S. Fan, "Absorption enhancement in ultrathin crystalline silicon solar cells with antireflection and light-trapping nanocone gratings," Nano letters **12**, 1616-1619 (2012).
45. E. R. Martins, J. Li, Y. Liu, V. Depauw, Z. Chen, J. Zhou, and T. F. Krauss, "Deterministic quasi-random nanostructures for photon control," Nat Commun **4**(2013).
46. A. Bozzola, M. Liscidini, and L. C. Andreani, "Broadband light trapping with disordered photonic structures in thin-film silicon solar cells," Progress in Photovoltaics: Research and Applications **22**, 1237-1245 (2014).
47. X. Fang, M. Lou, H. Bao, and C. Y. Zhao, "Thin films with disordered nanohole patterns for solar radiation absorbers," Journal of Quantitative Spectroscopy and Radiative Transfer (2015).
48. Z. Yu, A. Raman, and S. Fan, "Fundamental limit of light trapping in grating structures," Optics express **18**, A366-A380 (2010).

49. C. Trompoukis, O. El Daif, V. Depauw, I. Gordon, and J. Poortmans, "Photonic assisted light trapping integrated in ultrathin crystalline silicon solar cells by nanoimprint lithography," Applied Physics Letters **101**, 103901 (2012).

Résumé

Dans les cellules solaires en couches minces de silicium, il est important de maximiser l'efficacité d'absorption, notamment afin d'atteindre une densité de courant de court-circuit (J_{sc}) suffisante. Pour atteindre cet objectif, nous avons développé des stratégies de piégeage de la lumière à base de cristaux photoniques (CP) simplement périodiques et des structures plus complexes, pseudo-désordonnées. Ce travail vise à intégrer de telles structures dans des cellules solaires en couches minces de silicium cristallin (c-Si).

Tout d'abord, un CP à maille carrée de trous cylindriques ou de nano-pyramides inversées ont été intégrés dans cellules solaires à hétérojonction a-Si:H/c-Si en couches minces. L'absorption dans la seule couche absorbante (c-Si) est optimisée grâce à des simulations numériques utilisant la méthode de différences finies dans le domaine temporel. Le J_{sc} est augmenté de 56,4% (trous cylindriques) et 104,8% (nano-pyramides inversées) par rapport au cas sans motif. Nous avons également examiné des structures plus élaborées, où plus un CP de trous cylindriques est introduit en face arrière.

Deuxièmement, nous avons considéré des nanostructures complexes mais réalistes pseudo-désordonné, sur la base de supercellules périodiquement reproduites où les trous sont placés au hasard. Dans de telles structures l'absorption peut être augmentée par rapport à un réseau carré de trous optimisé, par augmentation de la densité spectrale de modes optiques. La simulation basée sur l'analyse rigoureuse couplée et la fabrication par lithographie par faisceau électronique et les technologies de gravure ionique réactive ont été effectués, conduisant à une augmentation de l'absorption nette d'environ 2,1% en théorie, et de 2,7% expérimentalement.

Enfin, nous avons mis en place des structures pseudo-désordonnées avec supercellules de tailles différentes, dans les couches c-Si de plusieurs épaisseurs dans la gamme 1-8μm. Les mécanismes d'absorption dans ces structures ont été analysés, à la fois dans les espaces réel et réciproque, en vue de déterminer des critères de conception. En outre, la réponse angulaire de la structure pseudo-désordonnée optimisée est plus stable que celle du réseau carré optimisé, en particulier dans les grandes longueurs d'onde.

Mot-clé : photovoltaïque, couche minces, silicium, cristaux photoniques, le désordre, piégeage de la lumière